ENGINEERING PERSPECTIVE

CONTENTS

Research Articles

ENGINEERING PERSPECTIVE

An International Journal

ENGINEERING PERSPECTIVE

Research Paper

Simulation of The Effects of Valve Timing Misalignment on Performance in Spark Ignition Engines

Emre Arabacı[1*] , Şule Öztürk[2] , Serdar Halis[1]

[1] *Automotive Engineering Dept., Faculty of Technology, Pamukkale University, Denizli, 20160, Türkiye*
[2] *Automotive Engineering Dept., The Graduate School of Natural and Applied Sciences, Pamukkale University, Denizli 20160, Türkiye*

ABSTRACT

Engine performance can be improved by changing the valve opening (or closing) timing without any cam profile changes. In this study, a simple simulation model was created for valve timing misalignment, which is an assembly defect in the engine. Due to misalign, the opening angles of the valves have been changed between +20 degrees and −20 degrees compared to the normal opening angles. The engine performance resulting from this advanced and retarded valve timing was examined for a four-stroke, spark ignition, single-cylinder engine with an engine volume of 393 cc. In this study conducted for the 1000-7000 rpm engine speed range, first the in-cylinder pressure data were examined in detail and then the general engine performance parameters were examined. Accordingly, opening the valves earlier than necessary at low and medium engine speeds increases the maximum in-cylinder pressure, and at high engine speeds, it reduces the maximum in-cylinder pressure due to excessive decrease in volumetric efficiency. It was observed that the volumetric efficiency, which was 0.89 at medium speeds, decreased to 0.70 due to misalignment. Regardless of whether the misalignment is positive or negative, pressure fluctuations increase during the valve lapping process. Maximum braking torque occurs at medium engine speeds. Positive misalignment reduces braking torque, especially for low and high engine speeds. However, especially at high speeds, negative misalignment reduces the pumping torque. While the pumping torque for high engine speeds was −3.78 Nm, it increased up to −5.04 Nm due to positive misalignment. Whether it is positive misalignment or negative misalignment, brake specific fuel consumption tends to increase in both cases. At low and medium engine speeds, negative misalignment or positive misalignment always increases residual gas fraction. As a result of the study, it was seen that misalignment negatively affected engine performance. However, it is seen that the value accepted as reference is the optimum value for the operating speed range of the engine. With this study, it has been understood that valve timing, as well as valve system design, is vital for engine performance.

Keywords: Engine simulation; misalignment; performance; valve timing

1. Introduction

Perhaps humanity's most perfect invention, which has a greater impact on society, economy, and environment, is the reciprocating internal combustion engines [1, 2]. Although many researchers have made significant contributions to the development of internal combustion engines, the historic breakthrough of Nicolaus Otto (1876) and Rudolf Diesel (1892) in the development of the spark ignition engine and compression ignition engine has been recognized worldwide [1-3] As a result of the widespread use of these engine technologies, 25% of the world's oil is consumed. For this reason, it is estimated that 10% of the world's greenhouse gases originate from internal combustion engines [4].

Internal combustion engines operate based on cycles in which sequential processes occur. A series of mechanical and electronic components are needed for the formation of these cycles. The main purpose of engine cycles is to obtain work. The process by which work is obtained is known as the expansion process [5-11]. In studying cycles thermodynamically, the focus is on obtaining work. In ideal thermodynamic cycles, intake and exhaust processes are neglected. However, the amount of work that can be achieved in a cycle is closely related to the geometric dimensions of the engine, the start of combustion and the performance of processes other than the expansion process. The gas exchange process is also an important parameter for a current engine. Because the performance of the intake process is very important to increase the exhaust process and energy

input to start a new cycle. The concept of increasing energy input can essentially be explained by the expression volumetric efficiency [10-15].

The amount of air sucked into each cylinder determines the amount of fuel that can be burned. Therefore, it is a very important design goal for the system to be able to flow as much air as possible into each cylinder (capacity to breathe at a certain rate). The degree to which burnt gases remaining from the previous cycle are expelled from the cylinder also affects the air flow entering the cylinder. For this reason, the exhaust process is at least as important as the intake process [5-11].

There are many parameters that affect volumetric efficiency. Some of these can be listed as quasi-static effects, flow friction in the intake and exhaust system, airflow choking in the intake valve, in-cylinder heat transfer, and overfilling. Apart from these, valve timing as a parameter also directly affects volumetric efficiency [1, 10-12]. All these parameters are design features for an engine.

The flow characteristic is different for each engine speed. To achieve high volumetric efficiency, separate valve timing must be designed for each engine speed. For this purpose, variable valve timing mechanisms are used in today's engines and thus the desire for high volumetric efficiency can be realized. Although there are various strategies for variable valve timing, the most used strategy is cam phase shifting. Continuously adjusting the phase of the intake cam and exhaust cam relative to the crankshaft is the most common approach. This approach uses an intake valve shut-off adjustment range of approximately 40 degrees ($\pm$ 20 degrees). With this method, approximately 5% torque increase can be achieved compared to a conventional engine [1, 16].

Valve timing is characterized by both the time the valves remain open and the time the valves open/close. For this reason, modified camshafts are preferred for a change in performance, especially in the engines of vehicles used for racing or hobby.

There are studies on valve timing in the literature. Liu et.al. investigated the effects of intake valve timing misalignment on maximum volumetric efficiency and backflow in a single-cylinder diesel engine. In this paper, it was mentioned that the closing timing of the intake valve directly affects the amount of backflow and the amount of fresh filling, and for this purpose, only the effect of the change of the intake valve closing timing was examined in 1D and 3D simulation models. As a result, he reported that the emergence of backflow is a gradual process, and that backflow is present when the engine reaches its maximum volumetric efficiency. Misalignment has been stated to approach zero only if the average valve closing speed approaches infinity [17]. Bücker et.al. conducted a study on in-cylinder flow control through variable valve timing in their paper. In this paper, it is mentioned that the in-cylinder flow is controlled by the cam phasing method on the intake camshaft. In this way, it is stated that volumetric efficiency will increase, and pumping loss will decrease. In this study, the underlying flow phenomenon, namely the effect of variable valve timing on tumble development and turbulent kinetic energy, is analyzed. The flow field was examined at a series of early, ambient, and late suction valve opening positions in the suction and compression processes. Variable valve timing has been shown to have a strong effect on mean vorticity and the local and temporal distribution of kinetic and turbulent kinetic energy. Additionally, it has been reported that the amount of turbulent kinetic

energy in the intake stage is linked to intake valve opening, which is important for fuel injection and mixing [18]. Abidin et.al. examined the effect of camshaft rating on performance in a passenger vehicle. What is meant by camshaft gradation here is the coincidence of the markings determined for the synchronization of the crankshaft and camshaft movements. In this study, the authors experimentally examined the effects of forward and reverse exhaust timing on performance. The results showed that the later the exhaust valve opens, the more torque and power are obtained at low engine speed [19]. Sher et.al. conducted a study on valve timing optimization in which specific fuel consumption would be minimum and engine torque would be maximum in a spark ignition engine. The basic performance parameters of the engine were calculated using a computer program that simulates the real engine cycle. When both valves and spark timings were optimized, it was concluded that the optimal timing of each valve apparently depended linearly on engine load, linearly on engine speed, while the slope depended weakly on engine load. It has been reported that because of the optimization, the maximum torque was shifted to a lower engine speed [20].

It is clear from previous papers that engine performance can be improved by changing the valve opening (or closing) timing without any cam profile changes. However, it seems that one of the main factors in this timing is engine speed. This study was created based on this context.

In this study, performance losses caused by incorrect installation of the timing mechanism during the maintenance of four-stroke internal combustion engines were investigated with a 1D simulation model. For this purpose, advance and delay conditions were created for a tested single-cylinder engine according to the reference state. Thus, the effects of valve timing misalignment on engine performance have been revealed.

2. Materials and Methods

2.1. One Dimensional Engine Model

Various licensed software are available for creating and analyzing realistic or quasi realistic simulations of internal combustion engines. In this study, a simulation program that allows 1D gas dynamics to be examined was used. Thanks to the program, the one-dimensional form of the Navier-Stokes equations governing mass, momentum and energy transfer for compressible gas flows is solved and sub models for combustion and emissions can be used [21]. Basic components in an engine were selected for simulation as shown on Figure 1.
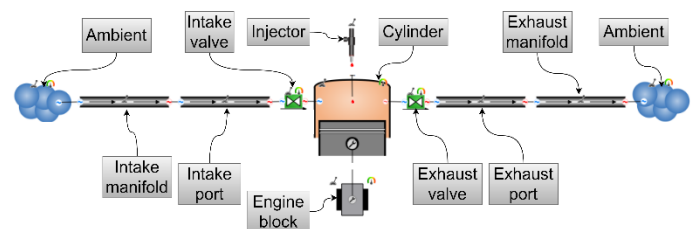

Figure 1. One-dimensional simulation model for single-cylinder engine

For the intake valve, the intake port and intake manifold are associated, and for the exhaust valve, the exhaust port and exhaust manifold are associated. Additionally, a direct injection fuel system was

preferred in the model. The engine used for simulation is a research engine whose accuracy has been previously proven and tested in the simulation program. Some important features of the engine used in the model are presented in Table 1.

Table 1. Specifications of the engine used for the simulation model

Specifications	Value
Stroke	82.0 mm
Bore	78.1 mm
Conrod Lenght	150 mm
Geometric compression ratio	10:1
Stroke volume	393 cm^3
Intake valve diameter	35 mm
Exhaust valve diameter	28 mm
Intake process duration (IPD)	280°CA
Exhaust process duration (EPD)	300°CA
Intake valve opening (IVO)	330°CA
Exhaust valve opening (EVO)	100°CA
Intake valve clearance	0.15 mm
Exhaust valve clearance	0.20 mm
Intake valve lift	8.89 mm
Exhaust valve lift	8.64 mm
Rocker arm ratio	1:1
Injection timing	−100°CA
Injection duration	20°CA
Injection pressure	20 bar

In the created model, two-zone Wiebe combustion model and load compensating Woschni heat transfer model were used. The Original Woschni heat transfer sub-model views the charge as having a uniform heat flow coefficient and velocity on all surfaces of the cylinder and calculates the amount of heat transferred to and from the charge based on these assumptions. The Load Compensating Woschni heat transfer sub-model uses Woschni's modified correlation which includes indicated mean effective pressure (IMEP) compensation. Chen-Flynn Correlation was used for friction losses. The ideal gas model was adopted for compressibility. RON 95 gasoline specifications were used as fuel. The fuel/air ratio is assumed to be stoichiometric for all cases.

2.2. Valve Timing Diagram

Internal combustion engines rely significantly on valve timing diagrams to regulate the intake and exhaust processes, facilitating the engine's breathing functions. Therefore, it is necessary to determine the opening and closing timings for the intake and exhaust valves in the engine throughout the cycle. The valve timing diagram for the engine whose specifications are given in Table 1 is presented in Figure 2. Here, the exhaust valve is open between EVO (Exhaust valve opening) and EVC (Exhaust valve closing). Similarly, the exhaust valve is open between IVO (Intake valve opening) and IVC (Intake valve closing). The region between EVC and IVO is called valve overlap, and both valves are open in this angular range. As seen in Figure 2, the reference points in the valve timing diagram are TDC (Top dead center) and BDC (Bottom dead center). All angular relationships are presented according to TDC and BDC. For this reason, the camshaft and crankshaft must be engaged correctly. In case of an

incorrect engagement, the valve timing diagram changes. However, the angle value between EVC and IVO does not change at all. For example, in a situation where EVC closes late, IVO also opens late, and in a situation where EVC closes early, IVO also opens early.
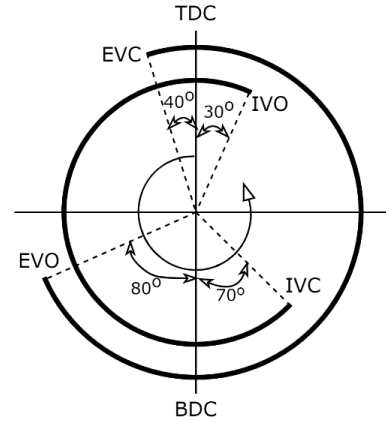
Figure 2. Valve timing diagram for reference engine

2.3. Model Parameters and Boundary Conditions

In the simulation model created, the parameters related to valve timing are IVO, EVO, IPD, and EPD. Valve overlap, EVC and IVC parameters are calculated parameters. Here, a variable (x) is defined for IVO and EVO next to the values in Table 2. Depending on the value of this variable x, IVO and EVO values become advanced or retarded compared to the values in Table 1. Accordingly, the angular relationships for valve timing are as follows. Here, the superscript * represents the values modified by variable x.

$$IVO^* = IVO + x \tag{1}$$
$$IVC^* = IVC^* + IVD \tag{2}$$
$$EVO^* = EVO + x \tag{3}$$
$$EVC^* = EVC^* + EVD \tag{4}$$

Here there are three possible cases for variable: $x < 0$, $x > 0$ and, $x = 0$. According to this:

- If $x < 0$, it means the valves open early (advanced case).
- If $x > 0$, it means the valves open late (retarded case),
- If $x = 0$, the valves open at the reference value (ideal case).

The expression of these three situations in the valve timing diagram is as in Figure 3.
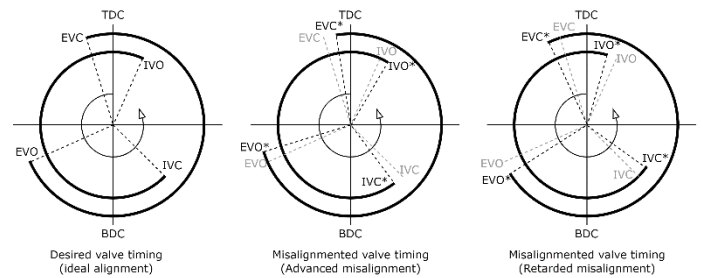
Figure 3. Valve timing misalignment cases

If you notice in Figure 3, the valve timing change is called misalignment. Because this angular misalignment occurs not to change engine performance but due to incorrect assembly.

For this study, it was assumed that the x value could range from −20 degrees (crank angle) to 20 degrees and solutions were made in 5 degree steps. Accepting that the engine speed can be changed from

1000 rpm to 7000 rpm, solutions were made in 1000 rpm steps. In addition, brake torque, pumping torque, residual gas ratio, brake power, brake specific fuel consumption, volumetric efficiency and exhaust temperature were used as performance parameters.

3. Results and Discussion

Performance losses due to incorrect installation of the timing mechanism during the maintenance of four-stroke internal combustion engines were examined on a 1D simulation model of a spark ignition engine and the following results are reported.

3.1. In-Cylinder Pressure Results

The results of in-cylinder pressure variation depending on crank movement were examined for three engine speeds (1000 rpm, 4000 rpm and 7000 rpm, low, medium and high, respectively). Inset graphs were created for more detailed analysis. Inset graph ① shows the intake valve closing, inset graph ② shows the maximum pressure, inset graph ③ shows the exhaust valve opening and inset graph ④ shows the valve overlap in detail.

Figure 4 shows the in-cylinder pressure values at low engine speed (1000 rpm).
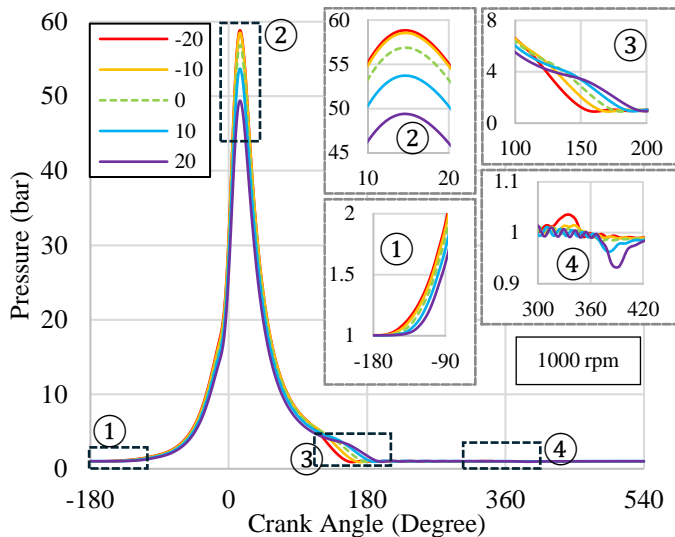
Figure 4. In-cylinder pressure for low engine speed

When Inset graph ① is examined, when the misalignment decreases, the intake valve closes early and therefore the compression process starts earlier. Thus, a higher end pressure of the compression process can be achieved. When Inset graph ② is examined, when the misalignment decreases e maximum in-cylinder pressure has also increased. In Inset graph ③, when the misalignment decreases, the in-cylinder pressure decreases faster because the exhaust valve opens earlier. In Inset graph ④, when the misalignment decreases, the valve overlap also occurs earlier. When misalignment increases, pressure fluctuation increases, albeit slightly.

In Figure 5, in-cylinder pressure values at medium engine speed (4000 rpm) are presented. When Inset graph ① is examined, when misalignment decreases, the intake valve closes early and therefore the compression process starts earlier. However, if you pay attention, the pressure difference caused by misalignment is less here. Inset graph When Inset graph ② is examined, when the misalignment decreases, the maximum in-cylinder pressure also increases. However,

whether the misalignment is −10 or −20 does not change the maximum in-cylinder pressure significantly. In Inset graph ③, when the misalignment decreases, the in-cylinder pressure decreases faster because the exhaust valve opens earlier. Inset graph In graph ④, when misalignment decreases, valve overlap occurs earlier. However, pressure fluctuation increases due to misalignment. For example, when the sample value is −20, the pressure change in the valve overlap is seen to be in the range of 0.6-1.5 bar.
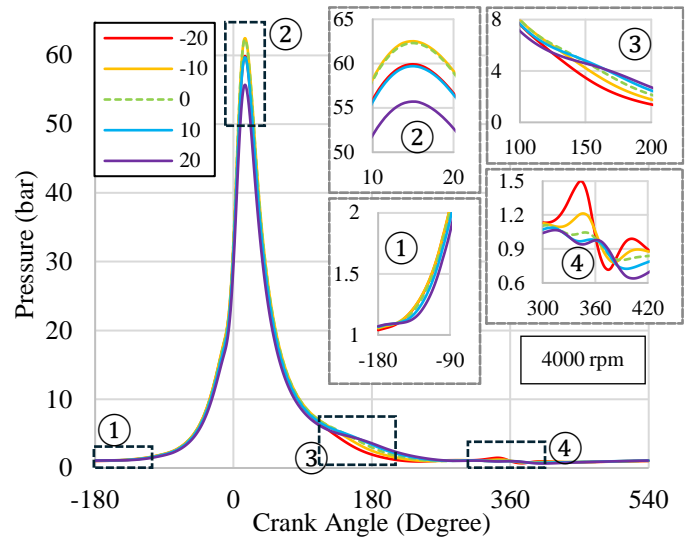
Figure 5. In-cylinder pressure for medium engine speed

In Figure 6, the in-cylinder pressure values at high engine speed (7000 rpm) are presented.
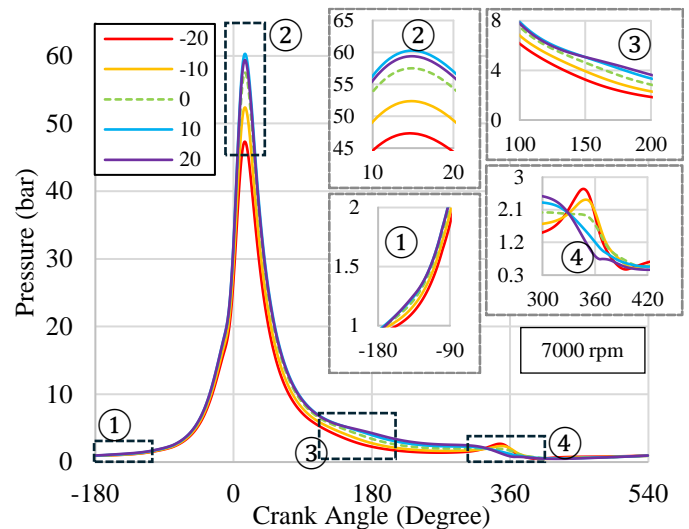
Figure 6. In-cylinder pressure for high engine speed

When Inset graph ① is examined, when the misalignment decreases, the intake valve closes early and therefore the compression process starts earlier. However, the in-cylinder pressure is lower. The possible reason for this is high pressure at high engine speed. volumetric efficiency decreases due to the flow requirement and the shortening of the time used to fill the fresh filler into the cylinder. When Inset graph ② is examined, when misalignment decreases, the maximum in-cylinder pressure e decreases significantly due to

the decrease in volumetric efficiency. The highest in-cylinder pressure misalignment is −10 case. In Inset graph ③, when the misalignment decreases, the in-cylinder pressure decreases faster because the exhaust valve opens earlier. In Inset graph ④, when the misalignment decreases, the valve lapping also occurs earlier. However, the pressure fluctuation increases due to misalignment. For example When the sample value is −20, the pressure change in the valve overlap is seen to be in the range of 0.6-2.5 bar.

3.2. General Performance Results

Braking torque, pumping torque, specific fuel consumption, residual gas rate, and volumetric efficiency were examined as performance parameters.

The performance map for brake torque is presented in Figure 7. Especially at medium engine speeds, creating negative misalignment significantly increases the braking torque. On the other hand, in negative misalignment at high engine speeds, engine torque decreases. Braking torque also tends to decrease in positive misalignment. Maximum engine torque occurs at medium engine speed in case of −20 to 5 misalignment.
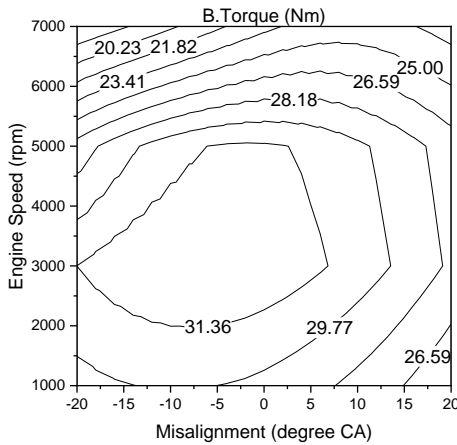
Figure 7. Performance map for brake torque

Figure 8 shows the performance map for pumping torque. As it is known, the main function of the valves is to manage the breathing of the engine and this process results in loss of pumping.
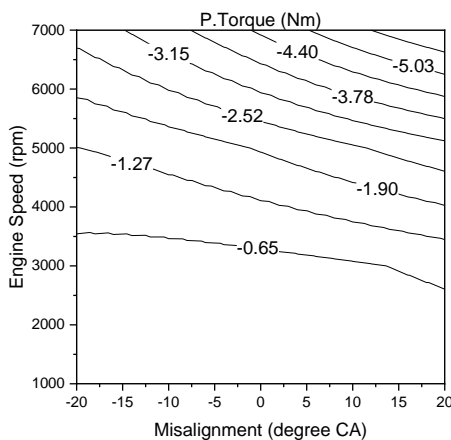
Figure 8. Performance map for pumping torque

Pumping loss tends to increase as engine speed increases. However, especially at high speeds, negative misalignment reduces the pumping torque. Late closing of the valve (positive misalignment) causes the pumping torque to increase. While the pumping torque was −0.65 Nm at low engine speeds, this value was determined as -3.15 Nm to 5.04 Nm at high engine speeds, depending on the misalignment condition.

The expression of engine efficiency based on fuel consumption and brake power is brake specific fuel consumption. Figure 9 shows the performance map for brake specific fuel consumption (BSFC). Whether it is positive misalignment or negative misalignment, BSFC tends to increase in both cases. However, it appears that negative misalignment at medium speeds does not have a significant effect on BSFC. It is seen that BSFC is at the level of 0.25 kg/kWh at low engine speeds. However, it increases up to 0.32 kg/kWh at high engine speeds.
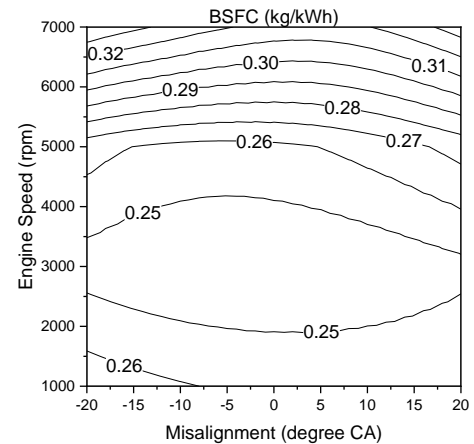
Figure 9. Performance map for brake specific fuel consumption

The operation of the valve system also affects the residual gas fraction (RGF). Figure 10 shows the performance map for RGF. At low and medium engine speeds, negative misalignment or positive misalignment always increases RGF. However, at high speeds, positive misalignment appears to have a reducing effect on RGF.
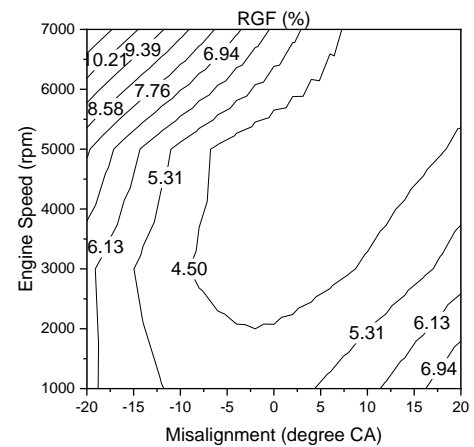
Figure 10. Performance map for residual gas fraction

The main performance of the valve system can be considered as volumetric efficiency. The performance map for volumetric efficiency is presented in Figure 11. Volumetric efficiency is higher, especially for medium engine speeds. When there is positive misalignment or negative misalignment in the engine, volumetric efficiency decreases. Especially at high engine speeds, negative misalignment reduces volumetric efficiency. The highest volumetric efficiency was 0.89 at medium engine speeds. Volumetric efficiency decreases up to 0.70 due to misalignment.
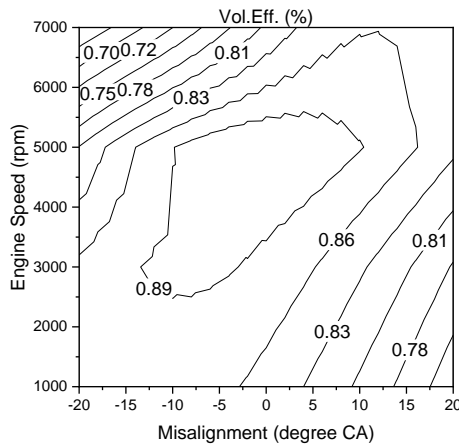
Figure 11. Performance map for volumetric efficiency

3.3. Discussion

According to the results obtained, negative alignment may be necessary at low engine speeds and positive alignment may be necessary at high engine speeds. The use of variable valve timing (VVT), one of today's technologies, can meet this need during engine operation. As it is known, the main goal of VVT is to ensure engine performance and economy by increasing the volumetric efficiency of the engine. Since fixed valve timing is used in conventional engines, engine performance cannot be the same for every engine operating condition. In this study, analysis was performed with the assumption that valve timing misalignment was caused by faulty assembly. As a result of this analysis, reference valve timing gives very good results with the design speed of the engine. In case of a possible valve timing error, performance losses may occur.

4. Conclusions

In this study, a simple simulation model was created for valve timing misalignment, which is an assembly defect in the engine. For example, the opening angles of the valves have been changed from +20 degrees to −20 degrees compared to the normal opening angles. The engine performance resulting from this advanced and retarded valve timing was examined for a four-stroke, spark ignition, single-cylinder engine with an engine volume of 393 cc. In this study conducted for the 1000-7000 rpm engine speed range, first the in-cylinder pressure data were examined in detail and then the general engine performance parameters were examined. Accordingly, opening the valves earlier than necessary at low and medium engine speeds increases the maximum in-cylinder pressure, and at high engine

speeds, it reduces the maximum in-cylinder pressure due to the excessive decrease in volumetric efficiency. Regardless of whether the misalignment is positive or negative, pressure fluctuations increase during the valve lapping process. Maximum braking torque occurs at medium engine speeds. Positive misalignment reduces braking torque, especially for low and high engine speeds. However, especially at high speeds, negative misalignment reduces the pumping torque. Whether it is positive misalignment or negative misalignment, BSFC tends to increase in both cases. However, it appears that negative misalignment at medium speeds does not have a significant effect on BSFC. At low and medium engine speeds, negative misalignment or positive misalignment always increases RGF. However, at high speeds, positive misalignment appears to have a reducing effect on RGF. Whether misalignment is positive or negative, volumetric efficiency decreases. Especially at high engine speeds, negative misalignment reduces volumetric efficiency. As a result of the study, it was seen that misalignment negatively affected engine performance. However, it is seen that the value accepted as reference is the optimum value for the operating speed range of the engine. With this study, it has been understood that valve timing, as well as valve system design, is vital for engine performance. The results obtained are of particular interest to engine designers.

Nomenclature

1D	One dimensional
3D	Three dimensional
BDC	Bottom dead center
BSFC	Brake specific fuel consumption (kg/kWh)
CA	Crank angle (degree)
EPD	Exhaust process duration (°CA)
EVC	Exhaust valve closing (°CA)
EVO	Exhaust valve opening (°CA)
IMEP	Indicated mean effective pressure
IPD	Intake process duration (°CA)
IVC	Intake valve closing (°CA)
IVO	Intake valve opening (°CA)
RGF	Residual gas fraction (%)
RON	Research octane number
TDC	Top dead center
VVT	Variable valve timing
x	Misalignment (°CA)

Conflict of Interest Statement

The authors declare that there is no conflict of interest in the study.

CRediT Author Statement

Emre Arabacı: Conceptualization, Writing-original draft, Validation, Supervision, **Şule Öztürk:** Conceptualization, Methodology, Writing-original draft, software, **Serdar Halis:** Conceptualization, Data curation, Formal analysis

References

1. Ferguson, C. R., & Kirkpatrick, A. T. (2015). Internal combustion engines: applied thermosciences. John Wiley & Sons.
2. Alagumalai, A. (2014). Internal combustion engines: Progress and prospects. Renewable and Sustainable Energy Reviews, 38, 561-571.
3. Grenning, W. (1991). History of the Otto–Langen Engine. Gas engine magazine. Febrery.
4. Reitz, R. D. (2013). Directions in internal combustion engine research. Combustion and Flame, 160(1), 1-8.
5. Merker, G. P., Schwarz, C., Stiesch, G., & Otto, F. (2005). Simulating Combustion: Simulation of combustion and pollutant formation for engine-development. Springer Science & Business Media.
6. Rajput, R. K. (2009). Engineering thermodynamics: A computer approach (SI units version). Jones & Bartlett Publishers.
7. Caton, J. A. (2015). An introduction to thermodynamic cycle simulations for internal combustion engines. John Wiley & Sons.
8. Babagiray, M., Solmaz, H., Ipci, D., & Aksoy, F. (2022). Modeling and validation of crankshaft speed fluctuations of a single-cylinder four-stroke diesel engine. Proceedings of the Institution of Mechanical Engineers, Part D: Journal of Automobile Engineering, 236(4), 553-568.
9. Babagiray, M., Kocakulak, T., Ardebili, S. M. S., Solmaz, H., Çınar, C., & Uyumaz, A. (2022). Experimental and statistical investigation of different valve lifts on HCCI combustion, performance and exhaust emissions using response surface method. Energy, 244, 123184.
10. Çınar, C., Uyumaz, A., Polat, S., Yılmaz, E., Can, Ö., & Solmaz, H. (2016). Combustion and performance characteristics of an HCCI engine utilizing trapped residual gas via reduced valve lift. Applied Thermal Engineering, 100, 586-594.
11. Qiang, Y., Ji, C., Wang, S., Xin, G., Hong, C., Wang, Z., & Shen, J. (2024). Study on the effect of variable valve timing and spark timing on the performance of the hydrogen-fueled engine with passive prechamber ignition under partial load conditions. Energy Conversion and Management, 302, 118104.
12. Gupta, H. N. (2012). Fundamentals of internal combustion engines. PHI Learning Pvt. Ltd.
13. White, C. M., Steeper, R. R., & Lutz, A. E. (2006). The hydrogen-fueled internal combustion engine: a technical review. International journal of hydrogen energy, 31(10), 1292-1305.
14. Wang, Y., Zu, B., Xu, Y., Wang, Z., & Liu, J. (2016). Performance analysis of a Miller cycle engine by an indirect analysis method with sparking and knock in consideration. Energy Conversion and Management, 119, 316-326.
15. Agarwal, A. K. (2007). Biofuels (alcohols and biodiesel) applications as fuels for internal combustion engines. Progress in energy and combustion science, 33(3), 233-271.
16. Heywood, John B. (1988). Internal combustion engine fundamentals. New York :McGraw-Hill,
17. Liu, F., Shi, Z., Hua, Y., Kang, N., Li, Y., & Zhang, Z. (2019). Study on the intake valve close timing misalignment between the maximum volume efficiency and the none backflow on a single cylinder diesel engine. Journal of Engineering for Gas Turbines and Power, 141(2), 021026.
18. Bücker, I., Karhoff, D. C., Klaas, M., & Schröder, W. (2013). Engine in-cylinder flow control via variable intake valve timing (No. 2013-24-0055). SAE Technical Paper.
19. Abidin, S. F. Z., Zulkefli, M. H., Ja'at, N. M., & Hassan, M. N. (2021). Effect of Camshaft Degreeing towards Performance of a Passenger Car. Fuel, Mixture Formation and Combustion Process, 3(1), 1-7.
20. Sher, E., & Bar-Kohany, T. (2002). Optimization of variable valve timing for maximizing performance of an unthrottled SI engine—a theoretical study. Energy, 27(8), 757-775.
21. Claywell, M., Horkheimer, D., & Stockburger, G. (2006). Investigation of intake concepts for a formula SAE four-cylinder engine using 1D/3D (Ricardo WAVE-VECTIS) coupled modeling techniques (No. 2006-01-3652). SAE Technical Paper.

ENGINEERING PERSPECTIVE

Research Paper
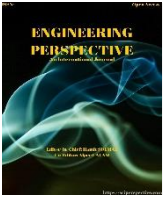
An Experimental Study of the Influences of Lacquer Thinner Addition to Gasoline on Performance and Emissions of a Spark Ignition Engine

Ahmet Uyumaz[1] ID, Ali Batuhan Kilmen[1*] ID, Murat Kaş[1] ID

[1] *Mechanical Engineering Department, Faculty of Engineering and Architecture, Burdur Mehmet Akif Ersoy University, Burdur, 15030, Turkey*

ABSTRACT

In this study, lacquer thinner (LT) has been utilized as an addition to pure gasoline in a single cylinder SI engine for increasing performance and reducing emissions. The tests were done at wide open throttle condition and 2400, 2700, 3000, 3300, 3600 and 3900 rpm engine speeds. The influences of lacquer thinner were observed on the engine torque, thermal efficiency, specific fuel consumption (SFC) and HC, CO and CO_2 emissions. The findings demonstrated that with the addition of the lacquer thinner caused engine torque and power output values to decrease as the amount of lacquer thinner increased. SFC was increased by about 4.36%, 9.13% and 11.64% with LT10, LT20 and LT30 compared to full gasoline at 2700 rpm respectively. But fairly noticeable reductions were observed at CO and HC emissions as lacquer thinner added to the gasoline. HC decreased by 3.4%, 5.6% and 12.13% with LT10, LT20 and LT30 according to gasoline at 3900 rpm respectively. Similarly, CO has decreased by 1.09%, 2.18% and 3.56% with LT10, LT20 and LT30 according to gasoline at 3900 rpm respectively. Lacquer thinner showed positive and impressive results compared to pure gasoline on exhaust emissions. However thermal efficiency decreased, and SFC has increased with lacquer thinner addition to gasoline, but the reduction in engine torque and power can be acceptable considering the drastic improvements at emission levels. Also, it has been observed that lacquer thinner can be used as a gasoline additive without any modifications in spark ignition engines. Still further research is needed on Lacquer thinner on SI engines.

Keywords: Engine Performance; Emissions; Lacquer Thinner; Spark Ignition Engine

1. Introduction

Alternative fuels or fuel additives are being searched by the researchers due to the reasons such as depletion of oil reserves and the harmful influences of the fossil fuels on the environment. Because spark ignition engines have lower emission rates compared to diesel engines, they are more prefer-able despite having lower thermal efficiencies and lower compression ratios. These circumstances can be further made better with the usage fuel additives in SI engines. Lacquer thinner, also known as cellulose thinner (LT) has drawn attention to improve spark ignition performance and emissions. LT is a ubiquitous and cheap substance that is used for thinning paints and is a powerful solvent that is used for cleaning painting equipment such as brushes. LT is produced from toluene, acetone and methanol. It also has high volatility characteristics which makes it suitable to mix with gasoline as an additive. Since LT is in liquid form it can be easily mixed with gasoline and other types of liquid fuels. Considering these facts LT can be used as an

ignition improver to achieve higher thermal efficiencies. When the literature was examined, it was realized that there are not many detailed studies on the effects of LT in SI engines. Awad et al. [1] has reviewed the usage of alcohols and ethers such as ethanol and methanol as fuels in SI engines. They have found that lesser CO and NO_x emissions, but specific fuel consumption (SFC) has increased. Chivu et al. [2] compared commercial diesel blends with turpentine obtained from pine trees they have found that 7.9% increase in torque at 15T85D mixture and 9% power increase at low speed and 5% power increase at high speeds with 30T70D mixture but it had a negative effect on NO_x emissions. Rao et al. [3] has found that with increasing toluene concentrations there was a consistent reduction of the HC, CO and NO_x. Eng et al. [4] tested n-octane/toluene and iso-octane/toluene blends to observe the influences. Kinetic interactions were realized between fuel species. Iqbal et al. [5] has developed ID correlation to guess knock for a toluene reference mixture. Nematizade et al. [6] compared an ethanol-gasoline blend and a G-series fuel of GS1 and GS2. They have

found that torque and power of the engine decreases (not significantly) and SFC increases but, HC reduces about 8% and CO reduces about 47%. Zhou et al. [7] commentated the performance of both lignin and cellulose derivatives. They have found that cetane number (CN) has higher effect than oxygen content. Machado et al. [8] looked on the influence of separate components and the amount of fuel on performance and combustion in SI engines. They have found that toluene and isooctane are important components because of their high-octane ratings also higher compression ratios are better for engines in operating conditions susceptible for knocking. Shahgholi et al. [9] investigated a gasoline engine's performance changes and emissions by gasoline mixtures and ethanol and thinner additives. They have found that addition of the thinner and ethanol increased SFC and reduced CO emissions also, increasing the amount of thinner and ethanol additives has reduced the vibration of the engine. Because SI engines present lower thermal efficiency compared to CI engines because of the lower CR. Gonca et al. [10] tested the impacts of dual mixtures on the theoretical performance characteristics of an SI engine. They have found that maximum decrease ratio of thermal efficiency is 29.71% with the combustion of 50% of methanol. Gonca et al. [11] has tested the effects of petroleum based liquid fuels and alcohols. They have found that fuel type considerably affects the brake power, brake thermal efficiency and NO formation. Ibrahim [12] researched the effects of diethyl ether in diesel engine. 15% diethyl ether showed the 7.2% increase on maximum brake thermal efficiency and 6.7% decrease on brake specific fuel consumption. Since fossil fuels are harmful to the environment and their reserves are getting depleted each day [13] it is crucial to search for alternative fuel sources or additives that are more readily available, cheap and more sustainable. Taking these facts into consideration lacquer thinner can be a good additive to gasoline since they have similar chemical compositions, and they mix well without any modification. In the current study, it was aimed to observe the influences of LT in terms of engine performance and exhaust emissions (HC, CO and CO_2) in a single cylinder four stroke spark ignition engines. For this purpose, the test engine was operated at wide opening throttle and different engine speeds between 2400 and 3900 rpm with the intervals of 300 rpm.

2. Material and Method

The experiments were conducted at Burdur Mehmet Akif Ersoy University, High Vocational School of Technical Sciences Automotive Laboratory. Figure 1 shows the schematic of the view of the test engine setup. Internal Combustion Engines (ICE) are critical machines in various applications from automotive to the industrial machinery. Understanding the effects of the LT on the performance and emissions as an additive to the gasoline in different conditions is essential. For that reason, six different engine speeds have been chosen and experiments were performed at full engine load condition (wide-open throttle), the selected engine speeds are 2400, 2700, 3000, 3300, 3600 and 3900 rpm. A torque sensor was coupled between the dynamometer and test engine shown in the Figure 1 Properties of the test engine were exhibited in the Table 1. Engine block temperature and oil temperature were held constant to prevent measurement differences. Engine was warmed up and then data was collected for each test. Honda GX 160, a single cylinder SI engine was fixed with an AC dynamometer for loading. When test engine started running dynamometer started to produce electricity, then using a potenti-

ometer and a rheostat were precisely adjusted and engine speed was manipulated. Lastly fuel consumption was determined with digital precision scale with 0.5 gr accuracy.
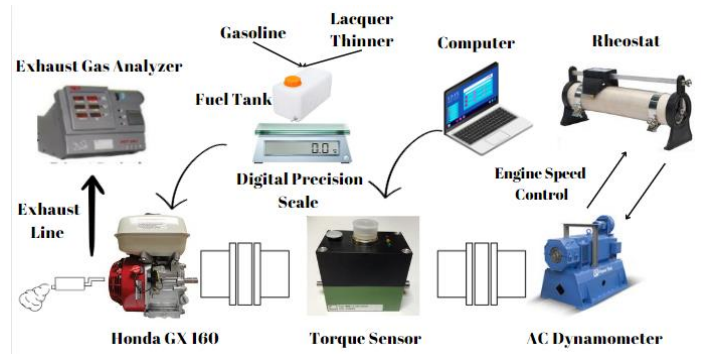
Figure 1. Schematic engine test setup

Table 1. Properties of the test engine

Model	Honda GX160
Bore x stroke [mm]	68x45
CR	8.5:1
Cylinder volume [cm³]	163
Power output [kW] HP@3600rpm	Max. 5.5
Torque [Nm]@2500 rpm	Max.10.78

Lacquer Thinner was used as additive to gasoline in this work. Properties of the gasoline and LT is given side by side in Table 2. Gasoline was the base reference fuel. For the preparation of the test fuels LT and gasoline was measured volumetrically and then combined to acquire 500 ml of test fuel in the end. At the end of each experiment amount of test fuel left was measured and then more gasoline and LT was added to the blend to achieve 500 ml again. LT is added to the gasoline at the rates of 10%, 20% and 30% to obtain test fuels. Test fuels have been named as LT10 (10 % Lacquer thinner + 90 % gasoline), LT20 (20% Lacquer thinner+ 80% gasoline), LT30 (30% Lacquer thinner+70% gasoline).

Table 2. Properties of the test fuels [10-16]

	Gasoline	Lacquer Thinner
Density [kg/m³]	746	870
Latent heat of vaporization [kJ/kg]	331.6	-
Calorific value [kJ/kg]	43594	41030
Flash point [°C]	-43	-7
Octane number	96.47	-
Boiling point [°C]	30-225	110,6 – 111,6
Auto ignition temperature [°C]	257.2	536

Engine torque was determined concurrently according to the engine speed. Engine torque and speed values were delivered to the computer. Technical specifications of the torque sensor are given in Table 3.

Table 3. Specifications of the torque sensor

Model	Burster 8661
Nominal supply voltage range [V DC]	10-30
-3 dB cutoff frequency [Hz]	200
Insulation resistance [MΩ]	> 5
Fluctuation [mV]	<50
Rated torque output voltage [V]	+10
Driver signal (K pin) [V DC]	10…30

HC, CO and CO_2 emissions were determined by using an exhaust gas analyzer. Technical properties of the emission analyzer are shown in the Table 4.

Table 4. Properties of the exhaust gas analyzer

	Operating Range	Accuracy
HC	0- 9999 ppm	1 ppm
CO_2	0-18 %	0.1 %
NO_x	0- 5000 ppm	1 ppm
O_2	0-25 %	0.01 %
CO	0- 14 %	0.001 %
λ	0-4	0.001

2.1. Data Reduction

The engine torque is a measured value versus on the engine speed. With engine speed and torque values engine power can be calculated using the Eq. (1).

$$N_e = \frac{M_e . n_e}{9549} \tag{1}$$

N_e stands for engine power, M_e stands for engine torque and n_e stands for engine rpm. After engine power is calculated SFC can be calculated using Eq. (2) [16].

$$SFC = \frac{m_f}{N_e} \tag{2}$$

m_f denotes the fuel consumption and SFC determines the engine fuel economy. Thermal efficiency has been calculated using the Eq. (3) [16].

$$\eta_T = \frac{N_e}{m_f . Q_{LHV}} \tag{3}$$

Here η_T shows the thermal efficiency and Q_{LHV} stands for the calorific value of the fuel [16].

3. Results and discussions

The changes of the engine torque can be viewed in the Figure 2. Maximum torque was reached at 2400 rpm for each test fuel and engine torque started to decrease as the engine speed increased. Heat losses and gas leakages increase with the rise of engine speed. Engine torque has decreased as the amount of LT raised in the blend. LT30 presented the lowest amount of torque. This is because LT has lower calorific value than gasoline. Engine torque has decreased about 4.66% at 2400 rpm. There is not

significant difference between gasoline and LT fuel mixtures. This phenomenon is attributed to the lack of oxygen and oxidation reactions slow down with the additive of LT in the fuel mixture.
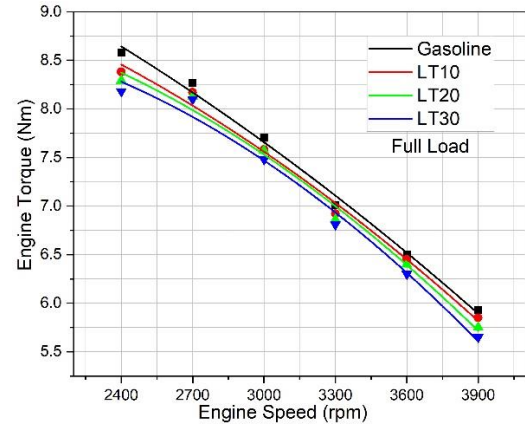
Figure 2. Engine torque

Power output of the engine rises with the rise of engine speed. Figure 3 exhibits the effect of LT on power output. Maximum effective power is computed at 3600 rpm for each test fuels. Volumetric efficiency is deteriorated at high engine speeds. Sufficient oxygen could not be delivered into the cylinder resulting in worse oxidation reactions. In addition, flow losses increase, and mechanical efficiency declines with the rise of engine speed. Hence, produced power decreases at high engine speed. Similarly to engine torque, power output decreases as the amount of LT increases in the blend. The highest power output was determined at 3600 rpm for all test fuels. Power output decreased 0.77%, 1.55% and 3.06% at LT10, LT20 and LT30 respectively at 3600 rpm. Kocakulak et al [14]. has found that with the addition of hexane to the gasoline reduced the engine torque in an SI engine.
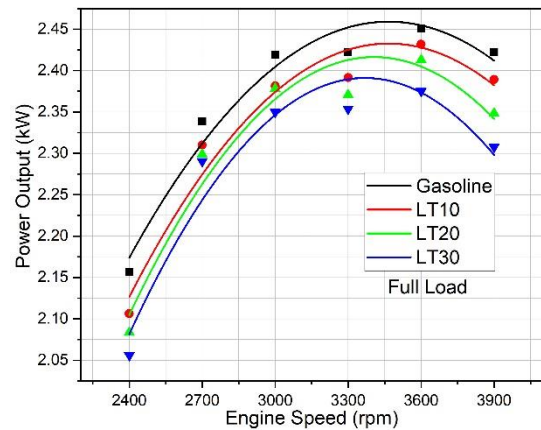
Figure 3. Power output

Figure 4 reflects the effects of LT on SFC. SFC is an important aspect of performance evaluations in internal combustion engines. When engine speed is too high or too low SFC increases as depicted in Figure 4. The lowest SFC data were calculated for 2700 rpm for all test fuels. And as expected increase of LT in the blend increased the SFC owing to LT having lower calorific value than gasoline and higher density. The increase of LT fraction in the fuel mixtures caused to increase of test fuel density. More charge mixture is taken into the cylinder by mass. So, higher fuel consumption is observed to obtain same power in comparison

with pure gasoline. The highest SFC value is calculated with LT30 blend. SFC increased by about 4.36%, 9.13% and 11.64% with LT10, LT20 and LT30 respectively at 2700 rpm. So, more LT is required to achieve required fuel energy to reach same power output.
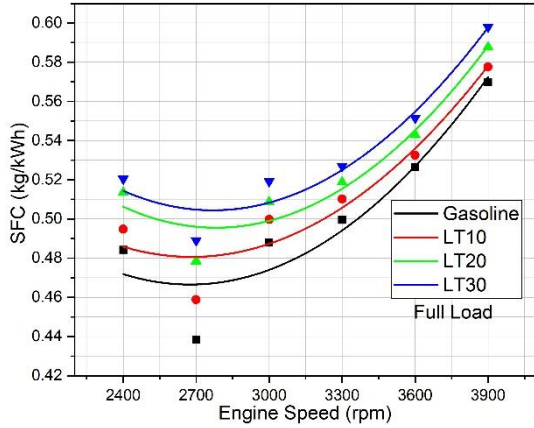
Figure 4. Effects of LT on SFC at various engine speeds

Thermal efficiency shows the produced net work depending on the obtained energy by ignition of the fuel. Calorific energy that is one of the most important factors affecting the thermal efficiency. The addition of LT leads to decrease thermal efficiency as seen in Figure 5. The lowest thermal efficiency was obtained using LT30. Thermal efficiency that is significant variable reflects the produced power output from obtained heat energy. Maximum thermal efficiency was determined at 2700 rpm for all test fuels. Figure 5 depicts the variations of thermal efficiency. Like SFC best thermal efficiency values are obtained at middle engine speed values. Maximum thermal efficiency values were also calculated at 2700 rpm. Thermal efficiency decreased by 3.69%, 6.90% and 8.15% at LT10, LT20 and LT30 respectively compared to gasoline.
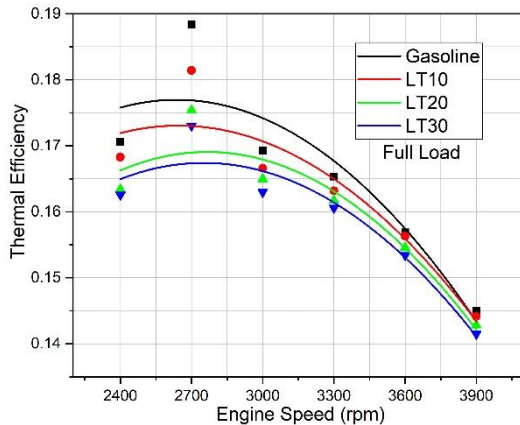
Figure 5. Effects of LT on thermal efficiency

Figure 6 shows the effects of LT on CO emissions. Incomplete combustion caused to obtain CO emissions. CO is generated due to lower cylinder temperature and lack of oxygen in combustion. As it can be seen in the Figure 6, with the addition of LT CO emission is reduced and lowest value is calculated with LT30 blend. At 3900 rpm measured CO values reduced by about 1.09%, 2.18% and 3.56% with LT10, LT20 and LT30 respec-

tively. So, with the addition of LT it can be said that the combustion is improved, and CO formation is decreased. Uyumaz [15] has found that with the addition of diethyl ether to the gasoline in an SI engine CO and HC emissions have reduced and as the amount of diethyl ether increased in the blend CO and HC emissions continued to reduce further.
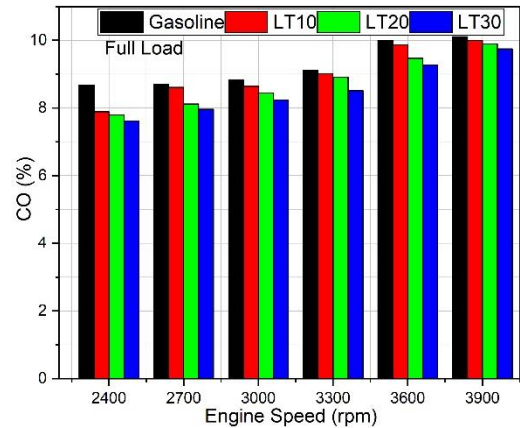
Figure 6. Effects of LT on CO emission
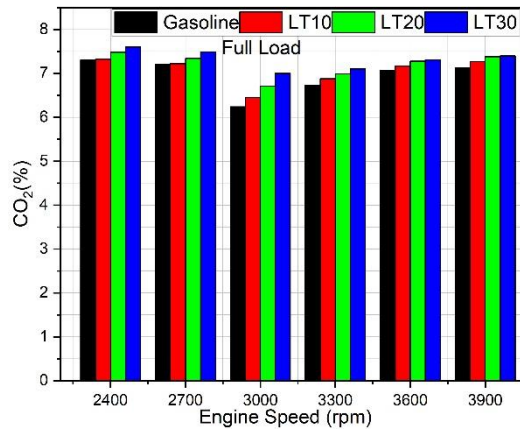
Figure 7. Effects of LT on CO_2 emission
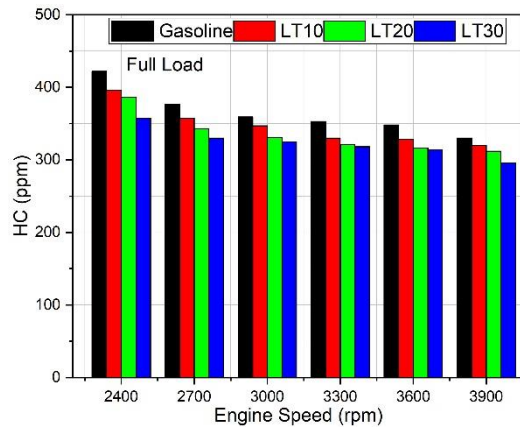
Figure 8. Effects of LT on HC emission

Figure 7 shows the changes of CO_2 emission. There is an inverse relationship between CO_2 and CO. So, as CO decreased CO_2 is increased with the addition of LT. The highest CO_2 like CO was determined at 3900 rpm for all test fuels. Highest CO_2

increase was 3.79% with LT30 blend. Higher density of LT caused to increase released heat and the temperature at the end of combustion. This situation helps to trigger the oxidation reactions. Hence, CO_2 formation is strengthened. It can be also stated that lower flash point of LT improves the combustion reactions resulting in more CO_2 generation. Lastly, values of determined HC emissions are given in Figure 8. At lower speeds the mixture cannot be properly ignited in the combustion chamber because of weak turbulence so HC formation is increased. As it can be seen here with the addition of LT HC emission is reduced significantly about by 3.4%, 5.46% and 12.13% with LT10, LT20 and LT30 respectively at 3900 rpm. Because of its high volatility, LT resulted lower unburned hydrocarbons.

4. Conclusions

The purpose of this experiment was to observe the influences of LT on engine performance and emissions as an addition to gasoline. The findings presented that with the addition of LT engine torque and power output is reduced but not that high of an amount that would render LT unusable as an additive to gasoline. Also, SFC is increased but this would be the case for any additive to gasoline that has lower calorific value than gasoline. The positive effects of LT as an additive lie on the emission side of the experiment. Harmful emissions such as CO and HC were reduced significantly with the addition of LT to the gasoline. HC reduced by 3.4%, 5.6% and 12.13% with LT10, LT20 and LT30 compared to gasoline at 3900 rpm respectively. CO has decreased by 1.09%, 2.18% and 3.56% with LT10, LT20 and LT30 compared to gasoline at 3900 rpm respectively. With these data, it can be said that lacquer thinner is a viable option to use as an additive to gasoline and can be used as without any modification whatsoever. Still further research is needed on the influences of LT on engine performance and emissions.

Nomenclature

|	
AC	Alternative current
CI	Compression ignition
CN	Cetane number
CR	Compression ratio
CO	Carbon monoxide
CO_2	Carbon dioxide
DC	Direct current
HC	Hydrocarbon
HP	Horsepower
ID	Ignition delay
LT	Lacquer thinner
SFC	Specific fuel consumption
SI	Spark ignition
m_f	Consumed fuel
M_e	Engine torque
N_e	Effective power
NO_x	Nitrogen oxide
Q_{LHV}	Lower heating value

Conflict of Interest Statement

The authors declare that there is no conflict of interest in the study.

CRediT Author Statement

Ahmet Uyumaz: Conceptualization, Supervision, Writing-review & editing
Ali Batuhan Kilmen: Conceptualization, Writing-original draft, Validation, Investigation
Murat Kaş: Methodology, Data curation, Formal analysis.

References

1. Awad, O. I., Mamat, R., Ali, O. M., Sidik, N. C., Yusaf, T., Kadirgama, K., & Kettner, M. (2018). Alcohol and ether as alternative fuels in spark ignition engine: A review. Renewable and Sustainable Energy Reviews, 82, 2586-2605.

2. Chivu, R. M., Martins, J., Popescu, F., Uzuneanu, K., Ion, I. V., Goncalves, M., ... & Brito, F. P. (2023). Turpentine as an additive for diesel engines: experimental study on pollutant emissions and engine performance. Energies, 16(13), 5150.

3. Rao, Y. S., Bansod, P. J., Moreno, M., & Manickam, M. (2024). Analysing the effects of toluene percentages and exhaust gas recirculation rates on spark-ignition engine performance and emissions. Thermal Science, 28(1 Part A), 197-207.

4. Eng, J. A., Leppard, W. R., Najt, P. M., & Dryer, F. L. (1998). The effect of fuel composition on hydrocarbon emissions from a spark ignition engine: iso-octane/toluene and n-octane/toluene fuel mixtures. SAE transactions, 1369-1389.

5. Iqbal, A., Selamet, A., Reese, R., & Vick, R. (2011). Ignition delay correlation for predicting autoignition of a Toluene reference fuel blend in spark ignition engines. SAE International Journal of Engines, 4(1), 219-234.

6. Nematizade, P., Ghobadian, B., Fathollah, O. M. M. İ., & Najafi, G. (2013). Performance and exhaust emissions of a spark ignition engine using GSeries and E20 fuels. International Journal of Automotive Engineering and Technologies, 2(2), 55-63.

7. Zhou, L., Heuser, B., Boot, M., Kremer, F., & Pischinger, S. (2015). Performance and emissions of lignin and cellulose based oxygenated fuels in a compression-ignition engine (No. 2015-01-0910). SAE Technical Paper.

8. Machado, G. B., Barros, J. E. M., Braga, S. L., & Braga, C. V. M. (2013). Influence of toluene and iso-octane on combustion and performance parameters of spark ignition engines (No. 2013-36-0229). SAE Technical Paper.

9. Shahgholi, G., Shayei, A., & Keyhandoust, M. (2022). The investigation of the effect of ethanol and thinner as a gasoline fuel additive on performance, pollution, and vibration of a gasoline engine. Journal of Environmental Science Studies, 7(3), 5329-5338.

10. Gonca G., Sahin B., Hocaoglu M. F., (2022), Influences of hydrogen and various gas fuel additions to different liquid fuels on the performance characteristics of a spark ignition engine, International Journal of Hydrogen Energy, 47(24), 12421-12431.

11. Gonca G., (2017),Influences of different fuel kinds and engine design parameters on the performance characteristics and NO formation of a spark ignition (SI) engine, Applied Thermal Engineering, 127, 194-202.

12. Ibrahim A., (2016), Investigating the effect of using diethyl ether as a fuel additive on diesel engine performance and combustion. Applied Thermal Engineering, 107:853-862.

13. Shafiee, S., & Topal, E. (2009). When will fossil fuel reserves be diminished?. Energy policy, 37(1), 181-189.

14. Kocakulak, T., Boyacıoğlu, N. M., Dağoğlu, Y., Uyumaz, A., Aksoy, F., & Arabacı, E. (2024). Experimental evaluation of gasoline-hexane fuel blends usage in a spark ignition engine. International Journal of Automotive Engineering and Technologies, 13(1), 45-53.

15. Uyumaz, A. (2023). Experimental Research With Diethyl Ether on Engine Performance and Emissions in a Spark Ignition Engine. International Journal of Automotive Science And Technology, 7(3), 167-174.

16. Heywood, J.B. Internal Combustion Engine Fundamentals, McGrawHill Publishing Company; New York, 1988.

ENGINEERING PERSPECTIVE

Modeling and Simulation of Integrated Photovoltaic-Alkaline Electrolyzer System for Sustainable Hydrogen Production

Fatima Haidar [1*] ID, Imen Mrad [1] ID, Quang Truc Dam [1] ID

[1] *Capgemini Engineering, Research & Innovation Direction, 12 rue de la Verrerie, 92190, Meudon, France*

ABSTRACT

In this research, the integration of an alkaline electrolyzer system with a photovoltaic (PV) array is explored to facilitate the green production of hydrogen. By directly coupling these two technologies, solar energy is harnessed to drive the electrolysis process, consequently generating hydrogen as a sustainable energy carrier. To enable accurate simulation and analysis of the integrated system, a novel methodology is introduced for identifying and quantifying the various parameters crucial for understanding the electrical behavior of the alkaline electrolyzer system. Through this method, the interplay between the PV array's output and the electrolyzer's operation can be comprehensively captured, allowing for precise modeling of the overall system dynamics. Moreover, mathematical equations are established to provide insights into the anticipated quantities of hydrogen generated by the electrolyzer system under different operating conditions. These equations serve as predictive tools, offering valuable insights into the system's performance and efficiency, essential for optimizing its design and operation. The proposed methodology and equations are implemented and validated using the MATLAB/Simulink environment, a powerful tool for simulating complex systems. By leveraging this platform, the integrated PV-electrolyzer system can be simulated with high fidelity, capturing its dynamic behavior and performance characteristics under varying scenarios. The promotion of renewable energy-based solutions for sustainable hydrogen production is aimed to be facilitated by this research, thereby contributing to the transition towards a greener and more resilient energy future.

Keywords: Alkaline Electrolyzer; Hydrogen; Mathematical Modeling; Solar System.

1. Introduction

The global energy landscape is undergoing a profound transformation driven by the increasing demand for energy and the imperative to mitigate the impacts of climate change [1 - 2]. As traditional fossil fuel reserves dwindle and concerns over greenhouse gas emissions escalate, there is an urgent need to explore and develop new sources of clean and sustainable energy [3]. Renewable energy sources, such as solar and wind power, have emerged as pivotal components of the transition towards a more environmentally friendly energy paradigm [4]. However, despite their abundance and potential, the widespread adoption of renewable energy faces significant challenges, including intermittency and the efficient storage and conversion of energy into electricity [5]. One of the key challenges in harnessing renewable energy is the intermittent nature of sources

such as solar and wind power. Unlike conventional fossil fuels, which provide a continuous and reliable source of energy, renewable sources fluctuate with weather conditions and time of day, presenting operational difficulties for their integration into existing electrical grids [6]. To address this challenge, there is a pressing need for innovative energy storage solutions that can store excess energy during periods of abundance and release it when needed [7]. In recent years, electrochemical storage systems, such as batteries and hydrogen fuel cells, have garnered significant attention as potential solutions to the energy storage problem [8]. Hydrogen, in particular, has emerged as a versatile energy carrier with the potential to store and transport energy derived from renewable sources [9]. The electrochemical conversion of hydrogen in fuel cells offers a clean and efficient way to generate electricity, with water vapor being the only byproduct [10]. However, the widespread adoption of hydrogen as

an energy carrier is hindered by challenges related to its production, storage, and distribution [6].

While most of today's hydrogen production methods rely on fossil fuels, there is growing interest in developing technologies that can directly convert renewable energy, such as solar power, into hydrogen [7], [11]. Among these technologies, the coupling of solar panels with electrolyzers has emerged as a promising approach for green hydrogen production [5]. By leveraging solar energy to power the electrolysis of water, this technique offers a sustainable and carbon-neutral method for producing hydrogen [12]. The efficiency of this process can reach up to 13%, making it a viable option for large-scale hydrogen production [8].

Electrolyzers, the key components in this process, come in several different technologies, including alkaline, membrane, and high-temperature steam electrolyzers [13]. Using those technologies, water is dissociated into hydrogen and oxygen gases through the application of an electric current. Of these, alkaline electrolyzers are one of the most established and widely used technologies for hydrogen production. They operate by utilizing an alkaline electrolyte, typically potassium hydroxide (KOH) or sodium hydroxide (NaOH), and electrodes made of materials like nickel or stainless steel. Alkaline electrolyzers offer several advantages, including relatively low capital costs, high efficiency, and long operational lifetimes. They are suitable for large-scale hydrogen production applications, such as industrial hydrogen generation, renewable energy storage, and transportation fuel production. Additionally, alkaline electrolyzers can operate at ambient temperatures and pressures, simplifying their integration into existing industrial processes and infrastructure. These attributes make Alkaline electrolyzers well-suited for integration with renewable energy sources, such as solar power [3], [9], [11].

In this study, the focus lies on the modeling and simulation of a photovoltaic system integrated with an alkaline electrolyzer for hydrogen production via water electrolysis. The electrolysis process is driven by the electrical energy provided by photovoltaic panels, with excess energy being stored in the form of hydrogen [14 - 16]. Utilizing advanced modeling techniques and simulation tools like MATLAB/Simulink, emphasis is placed on optimizing the performance of the integrated system and identifying the most favorable conditions for efficient hydrogen production. Through this research, a contribution is aimed to be made towards the advancement of sustainable energy solutions and the acceleration of the transition towards a greener and more resilient energy future.

The flowchart as shown in Figure 1 outlines the study's progression, beginning with an introduction to global energy challenges and the significance of transitioning to renewable energy sources, particularly hydrogen. Motivation is provided for exploring sustainable hydrogen production methods, leading to the integration of photovoltaic and electrolyzer systems for green hydrogen generation. In *section 2*, theoretical principles of hydrogen production and design concepts for photovoltaic and alkaline electrolyzer systems are then elucidated. Mathematical modeling follows, detailing the development of equations to describe PV panel and electrolyzer behaviour, including factors influencing hydrogen production rates. *Section 3* is devoted to simulation setup for implementing these models using
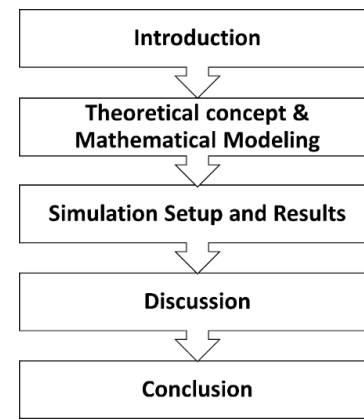
Figure 1. Flowchart summarizing the entire study.

MATLAB/Simulink and configuring the integrated PV-electrolyzer system and its result. Discussion analysis entails examining simulation data on PV module performance and hydrogen production rates, elucidating trends and correlations between variables is presented in *section 4*. Finally, the conclusion summarizes findings regarding system performance and efficiency, while also suggesting future research directions for energy storage and grid integration solutions.

2.2. Theoretical concept of alkaline Technology and PV system

2.2.1. Principle of hydrogen production

The principle of hydrogen production [13] within the system under study encompasses three primary subsystems, each integral to the overall process:

Firstly, the production of renewable electric energy serves as the initial step in the hydrogen production chain. This process relies heavily on the utilization of photovoltaic panels, converting incident solar radiation into electricity through the photovoltaic effect. The electricity generated by the solar panels serves as the primary energy source for the subsequent electrolysis of water, thus initiating the production of hydrogen [13]. Secondly, the electrolysis of water represents the pivotal stage wherein water molecules are dissociated into their constituent elements, hydrogen and oxygen. Various electrolysis techniques are employed for this purpose, with alkaline electrolyzers, polymer membrane electrolyzers, and ceramic oxide electrolyzers being the most commonly utilized methods. These electrolysis techniques facilitate the efficient separation of hydrogen and oxygen gases, enabling the selective extraction of hydrogen for subsequent storage and utilization.

Lastly, the storage of gases constitutes the final component of the hydrogen production process. This phase involves the collection and containment of the produced hydrogen gas for future use. Commonly employed techniques for hydrogen storage include liquefaction and hydration processes. Liquefaction involves cooling the hydrogen gas to extremely low temperatures, thereby converting it into a liquid state for denser and more compact storage. Alternatively, hydration methods involve the absorption of hydrogen gas into a solid matrix, such as metal hydrides, for safe and efficient storage [13], [17].
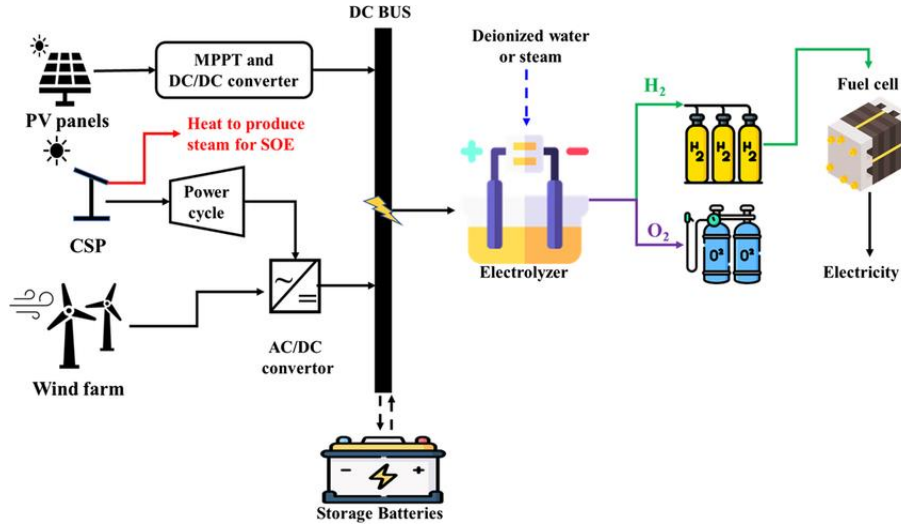
Figure 2. Configuration and operational principles of the Hydrogen production facility [13].

The configuration and operational principles of the hydrogen production facility are depicted in Figure 2, illustrating the interconnectedness of the various subsystems involved in the process. The efficient coordination and integration of these subsystems are essential for optimizing hydrogen production efficiency and ensuring the viability of the overall system. Through continuous research and development efforts, advancements in each of these subsystems contribute to the realization of sustainable and scalable hydrogen production solutions, thereby facilitating the transition towards a cleaner and more sustainable energy landscape.

2.2.2. Designing the Photovoltaic System

In the realm of renewable energy systems, the photovoltaic (PV) generator stands as a cornerstone for sustainable energy production [14 - 16]. In this study, the photovoltaic system's energy production is predominantly facilitated by the photovoltaic generator, which harnesses solar radiation to generate electricity. Leveraging the climate data specific to the site, including sunshine duration and ambient temperature, alongside module specifications provided by the manufacturer, enables precise estimation of the energy output achievable by the photovoltaic module.

The mathematical model of a photovoltaic generator relies on an equivalent circuit. In Figure 3 below, the equivalent circuit is depicted, featuring a current source I_{ph} representing the photocurrent generated by the cell, with R_s and R_{sh} denoting the inherent shunt and series resistances of the cell, respectively, along a diode in parallel [1-3].

PV cells are assembled into larger units known as PV modules, which are then interconnected in a parallel-series arrangement to create PV arrays. Typically, R_{sh} has a very high value, and R_s has a very low value, thus they can often be disregarded to simplify the analysis.

The mathematical model of the photovoltaic panel is described as following in the Eq. (1):

$$I_{ph} = [I_{sc\ ref} + Ki\ (T - T_{ref}\ )] \times Insol \tag{1}$$

Where, $I_{sc\ ref}$ is the short-circuit current (ISC) at reference tem-

perature, Ki denotes the short-circuit current temperature co-efficient, T is the operating temperature of the module, T_{ref} is the reference temperature of the module, and $Insol$ is the Input current of a PV module.

The reverse saturation current (I_{rs}) is calculated as following in the Eq. (2):

$$I_{rs} = I_{sc}/[exp(\frac{qV_{oc}}{N_s kAT_{ref}} - 1] \tag{2}$$

Where N_s is the total number of cells in series, V_{oc} is the open circuit voltage, q represents the Electron charge, k denotes the Boltzmann constant, and A is an idealist factor.

The module's saturation current is then calculated using Eq. (3):

$$I_s = I_{rs}\left[\frac{T_a}{T_{ref}}\right] exp[\frac{q \times E_{g0}}{Bk}\ \left(\frac{1}{T_{ref}} - \frac{1}{T_a}\right)] \tag{3}$$

Where, E_{g0} is the band gap for silicon, $B = A$, and T_a is the operating temperature of the module.

Hence, the calculation of the photovoltaic panel current can be expressed as follows in the Eq. (4):

$$I_{PV} = N_p \times I_{ph} - N_p \times I_0 \left[exp\left(\frac{q \times V_{PV} + I_{PV} R_s}{N_s kAT}\right) - 1\right] \tag{4}$$

Where, N_p represents the number of cells connected in parallel, and V_{PV} is the output voltage of a PV module.
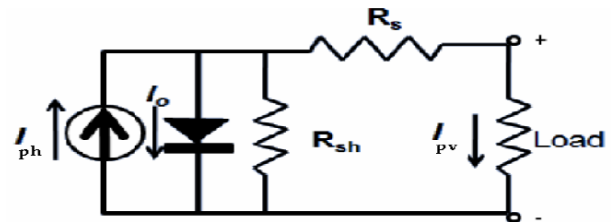

Figure 3. PV cell modelled as an equivalent circuit with diodes

2.3. Designing the Alkaline Electrolyzer System

An electrolyzer serves as a pivotal device in the production of hydrogen, leveraging electrical energy to facilitate the electrolysis of water into its constituent elements, hydrogen, and oxygen, via an electrochemical process. To facilitate the splitting of water molecules, a direct current (DC) must be applied across two electrodes immersed in an aqueous electrolyte with high ionic conductivity (Tijani et al., 2014; Ulleberg, 2003). Typically, the overarching reaction for water splitting is represented as follows in the Eq. (5):

$$H_2O_{(l)} + electrical\ energy \qquad (5)$$

By using the stoichiometry, the production rate of water consumption and oxygen also can be determined as in the Eq. (6):

$$\dot{n}_{H_2O} = \dot{n}_{H_2,prod} = 2\dot{n}_{O_2} \qquad (6)$$

In this study, emphasis is placed on the Alkaline electrolyzer, chosen for its efficiency in hydrogen production. The water electrolyzer comprises multiple electrolyzer cells interconnected either in series, parallel, or both. Our electrolyzer model is intricately designed based on the characteristics of individual cells, with parameters such as operating voltage and gas flow rates determined per cell. Scaling up to the entire electrolysis unit involves simple multiplication of these values by the number of cells in series and parallel. For the sake of modelling the electrolyzer, its mathematical model will be analysed in the following:

The thermal model uses current and voltage, to calculate the temperature variation within the electrolyzer cell by modeling the following equation Eq. (7):

$$C_t \frac{dT}{dt} = \dot{q}_{gen} - \dot{q}_{loss} - \dot{q}_{cooling} \qquad (7)$$

Where, T is the Cell temperature in Kelvin, C_t denotes the Overall thermal capacity of the electrolyzer, $\dot{q}_{gen}$ is the Heat power generated inside the electrolyzer, $\dot{q}_{loss}$ is the Heat power loss and $\dot{q}_{cooling}$ is the Cooling heat power.

For reference (details provided below for each calculation):
→ $\dot{q}_{gen}$ → Can be written as: $\dot{q}_{gen} = (V - V_{th}) \times I$ with

$V_{th} = \frac{-\Delta H}{2F}$

→ $\dot{q}_{loss}$ → Can be determined by: $\dot{q}_{loss} = \frac{1}{R_t}$ $(T - T_{amb})$ with R_t is the thermal resistance of the electrolyzer and T_{amb} is the ambient temperature.

→ $\dot{q}_{cooling}$ → Can be expressed as $\dot{q}_{cooling} = C_m \times (T_{cm,s} - T_{cm,e})$ with C_m is the thermal capacity of the cooling water, $T_{cm,s}$ is the inlet cooling water temperature, and $T_{cm,e}$ is the outlet cooling water temperature with:

$$T_{cm,s} = T_{cm,e} + (T - T_{cm,e}) + (1 - \exp(-\frac{V_{AHX}}{C_m}))$$

and V_{AHX} is the overall heat transfer coefficient. It is obtained by the following equation: $V_{AHX} = h_{cond} + h_{conv}.I$ where, h_{cond} and h_{conv} are the parameters related respectively to heat transfer by conduction and by convection.

The overall energy balance is defined as in the Eq. (8):

$$\frac{dT}{dt} + aT - b = 0 \qquad (8)$$

The solution to the differential equation of the balance is given by the Eq. (9):

$$T(t) = \left(T_{ini} - \frac{b}{a}\right)exp(-at) + \frac{b}{a} \qquad (9)$$

With:

$$a = \frac{1}{R_t.C_t} + \frac{C_{cm}}{C_t}\left(1 - exp\left(-\frac{V_{AHX}}{C_{cm}}\right)\right)$$

$$b = \frac{n_c(V - V_{th}).I}{C_t} + \frac{T_{amb}}{R_t C_t} \qquad (10)$$
$$+ \frac{C_{cm}T_{cm,c}}{C_t}\left(1 - exp\left(-\frac{V_{AHX}}{C_{cm}}\right)\right)$$

In a non-spontaneous electrochemical process, the change in free energy is equivalent to the electrical work required for the reaction to occur. The cell voltage U_{Ecell}, expressed in volts is defined by the Eq. (11):

$$U_{Ecell} = U_{rev} + \frac{r_1 + r_2 T}{A}I$$
$$+ s\ln\left(\frac{t_1 + \frac{t_2}{T} + \frac{t_3}{T^2}}{A}I + 1\right) \qquad (11)$$

Where, r_1 and r_2 represent the parameters of ohmic resistance ($\Omega.m^2$, $\Omega.m^2/°C$), s is the Ohmic voltage (V), t_1, t_2 and t_3 are the overvoltage parameters; t_1 ($m^2·A^{-1}$), t_2 ($m^2·C.A^{-1}$), t_3 ($m^2·C^2/A^{-1}$), A is the area of the cell electrode (m^2), I represents the electrolyzer current in (A), T is the cell temperature (°C) and U_{rev} is the reversible voltage (V).

When assuming a reversible reaction, the energy of the process (H) is utilized with a reversible voltage as indicated in the following reaction (12):

$$U_{rev} = \frac{\Delta G}{ZF} \qquad (12)$$

Where, ΔG represents the Gibbs free energy, Z is the number of electrons (2e⁻), which is the number of molecules transferred per molecule of hydrogen, equal to 2, F is a Faraday's constant (96500 C), U_{rev} which can be expressed by an empirical equation as: $U_{rev} = U_{rev}^0 - k_{rev}(T - 25)$ where U_{rev}^0 denotes the reversible

cell voltage under standard conditions and k_{rev} is the empirical temperature coefficient of U_{rev} (V/°C).

The cells of an electrolyzer are connected in series, so the current is the same and the voltage is given by the following Eq. (13):

$$U_E = n_C . U_{Ecell} \qquad (13)$$

The amount of hydrogen generated can be calculated from the voltage and current of the electrolyzer as in the following Eq. (14):

$$\dot{n}_{H_2,prod} = \eta_F \frac{N_c I}{ZF} \qquad (14)$$

Where Z is equal 2.

According to Faraday's law, the production of hydrogen is influenced by the rate of electron transfer at the electrodes, which corresponds to the electrical current in the external circuit. Conversely, Faraday efficiency represents the ratio of actual hydrogen production to the theoretical maximum achievable in the electrolyzer. However, Faraday efficiency can be compromised by parasitic current losses, which increase as current densities decrease due to higher electrolyte share, leading to reduced electrical resistance. Moreover, temperature elevation results in decreased resistance, amplifying parasitic current losses and consequently lowering Faraday efficiency which can be determined as in the following Eq. (15):

$$\eta_F = \frac{\left(\frac{I}{A}\right)^2}{f_1 + \left(\frac{I}{A}\right)^2} f_2 \qquad (15)$$

Where, I is the current of the electrolyzer, n_C is the number of particles (21), A represent the Effective surface 0.25, f_1 and f_2 denotes the calculation parameters of the faradic efficiency 250 mA²/cm⁴, 0.96 respectively, $\dot{n}_{H_2,prod}$ is the rate of hydrogen production (mol/s) and η_F is the Faradaic efficiency.

The determination of the volume flow rate of hydrogen is influenced by several factors inherent to the electrolysis process and the operational parameters of the electrolyzer system. Key factors include the current density applied to the electrolyzer, the efficiency of the electrolysis process, the temperature and pressure conditions within the system, and the composition of the electrolyte used. Additionally, factors such as the electrode surface area and the design

of the electrolyzer cells can also impact the volume flow rate of hydrogen. The hydrogen production rate, denoted by $\dot{n}_{H_2,prod}$, is initially measured in units of mol/s, representing the amount of hydrogen generated per unit time. To convert this rate into a more commonly used unit for industrial applications, such as Nm³/h (normal cubic meters per hour), a series of conversions are applied. Firstly, to convert from mol/s to mol/h, the production rate is multiplied by the number of seconds in an hour (3600), extending the measurement to an hourly basis. Subsequently, to account for the volumetric properties of gases under standard conditions (typically defined as 1 atm pressure and 0°C temperature), the production rate is multiplied by the molar volume of an ideal gas at these conditions. This value, commonly denoted by V_m is approximately 0.022414 m³/mol. Therefore, the equation for Q, representing the hydrogen production rate in Nm³/h, is derived as follows in Eq. (16):

$$Q = \dot{n}_{H_2,prod} \times 3600 \times 0.022414 \qquad (16)$$

3. Simulation results

The integration of an alkaline electrolyzer system with a photovoltaic (PV) array for green hydrogen production has been extensively explored in this research. Through simulation and analysis using MATLAB/Simulink environment, the dynamic behaviour and performance characteristics of the integrated PV-electrolyzer system have been investigated. This setup was established to illustrate the configuration depicted in Figure 4.

The simulation model, as depicted in Figures 4 integrates the PV system with the alkaline electrolyzer, allowing for the direct coupling of solar energy to drive the electrolysis process for hydrogen production.

The PV model comprises six interconnected subsystems as shown in Figure 5 and represent the calculation to modelized the PV using Eq. (1) to Eq. (4), while the electrolyzer model in Figure 6, consists of three sub-systems: thermal, electrochemical, and hydrogen production models. The Eq. (7) to (15) represent the calculation to modelized the alkaline Electrolyzer coupled to PV system.

■ **PV with single cell ($N_p = 1$)**

Firstly, the performance of the PV module with a single cell ($N_p = 1$) was analysed under varying irradiation conditions at a constant temperature of 25 °C. Figures 7, 8, and 9 illustrate the I-V and P-V characteristics of the PV module, showing the module's current, voltage, and power output under different irradiation levels. The input irradiation is shown in Figure 7. Between 0 and 1 s, the irradiation is 200 W/m², between 1 and 2 s it is 600 W/m², while from 2 s onwards it is 1000 W/m². These results provide insights into the PV system's behaviour and performance under changing environmental conditions.

Figure 8 illustrates the relationship between module current I_{PV} and module voltage V_{PV} for varying levels of irradiation. Each curve represents a different irradiation level: 200 W/m², 600 W/m², and 1000 W/m². As expected, at higher irradiation levels, the module current is generally higher across the entire voltage range. This is
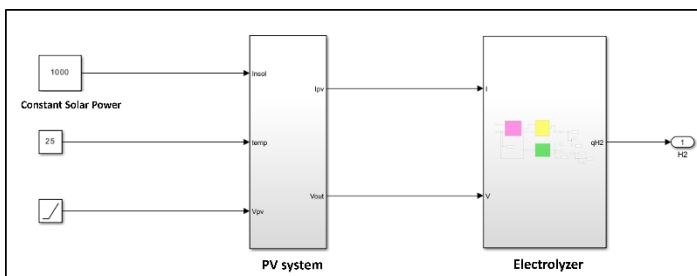
Figure 4. Simulation model of direct coupling of an electrolyzer to PV system
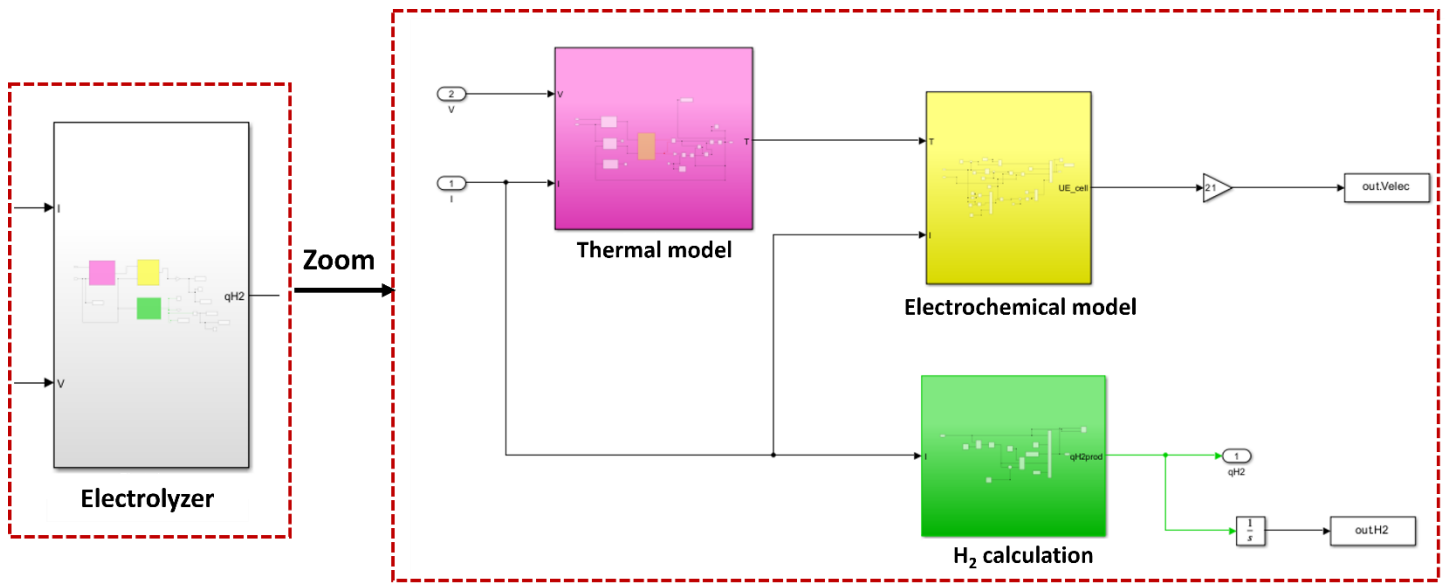
Figure 5. The MATLAB/Simulink sub-blocks of the Solar Panel model
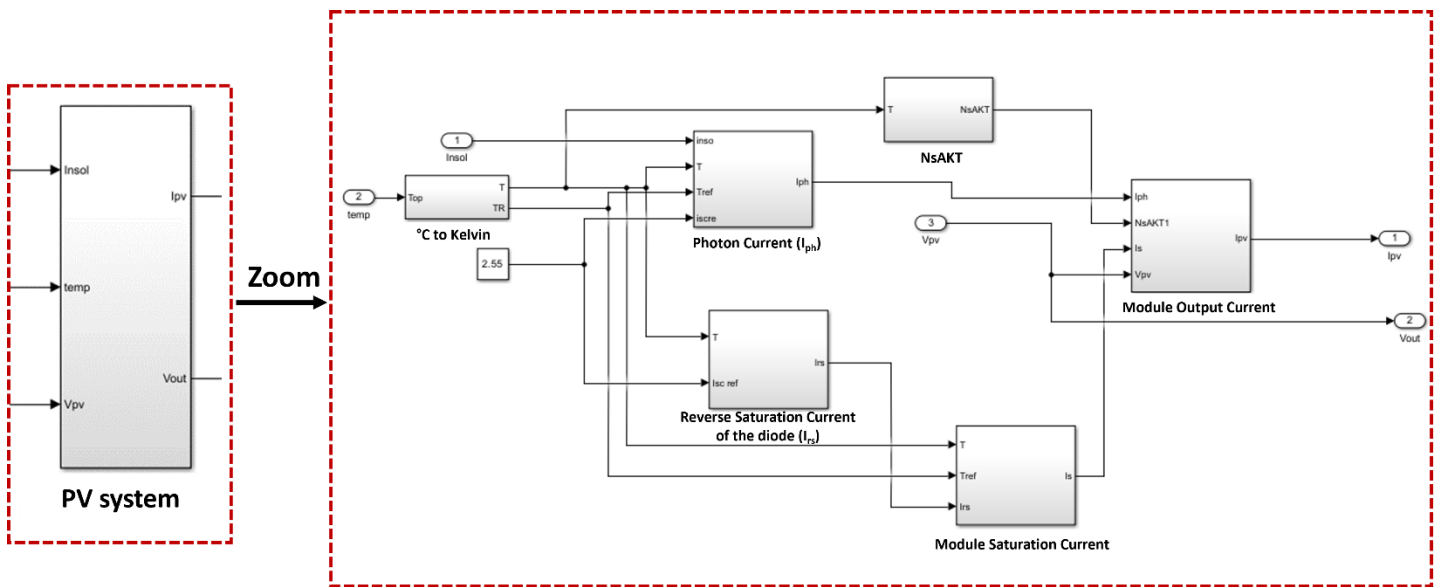
Figure 6. The MATLAB/Simulink sub-blocks of the electrolyzer

because increased solar irradiance leads to greater generation of electrical current in the photovoltaic cells. Conversely, at lower irradiation levels, such as 200 W/m^2, the module current is lower across the voltage range. This relationship is consistent with the basic behaviour of photovoltaic systems, where the amount of electricity generated is directly proportional to the intensity of incident sunlight.

In the other hand, the Figure 9 depicts the relationship between module power (P_{PV}) and module voltage (V_{PV}) under varying irradiation conditions. Similar to the module current graph, each curve represents a different irradiation level: 200 W/m^2, 600 W/m^2, and 1000 W/m^2. It is evident that module power exhibits a quadratic relationship with module voltage, as expected from the fundamental

characteristics of photovoltaic systems. At higher irradiation levels, the module power curve is shifted upwards, indicating greater power output across the voltage range. Conversely, at lower irradiation levels, the module power curve is shifted downwards, reflecting reduced power output. This behaviour highlights the direct influence of solar irradiance on the power generation capabilities of photovoltaic modules, with higher irradiance levels resulting in increased power output and vice versa.
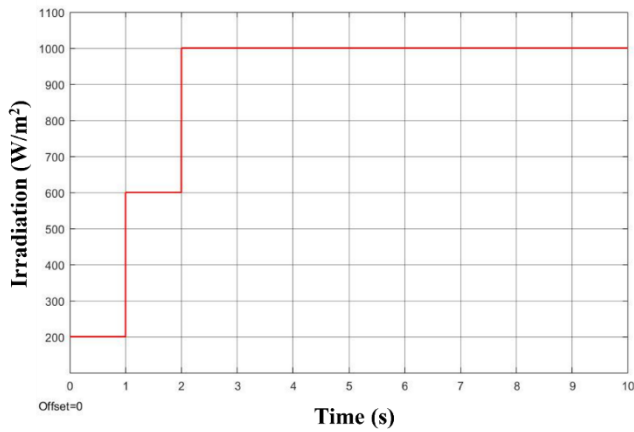
Figure 7. Input – Time varying irradiation
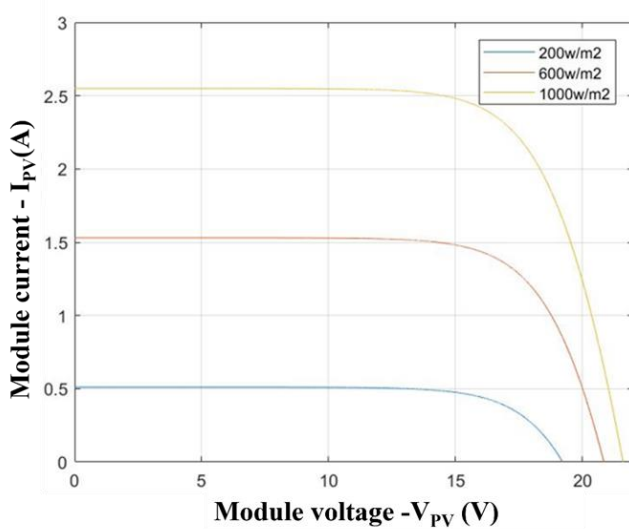
Figure 8. Module current – I-V characteristics with varying irradiation.
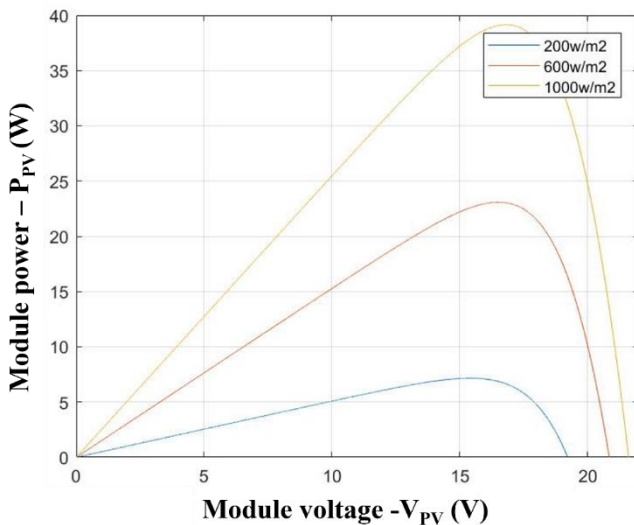
Figure 9. Module power – P-V characteristics with varying irradiation

- **PV (30 cells) - Electrolyzer**

The PV system with 30 cells connected in parallel ($N_p = 30$) was further investigated in conjunction with the electrolyzer. Applying the Eq. (4), using $N_p = 30$ giving us the I_{PV} and V_{PV} output for the PV as presented in Figure 10.
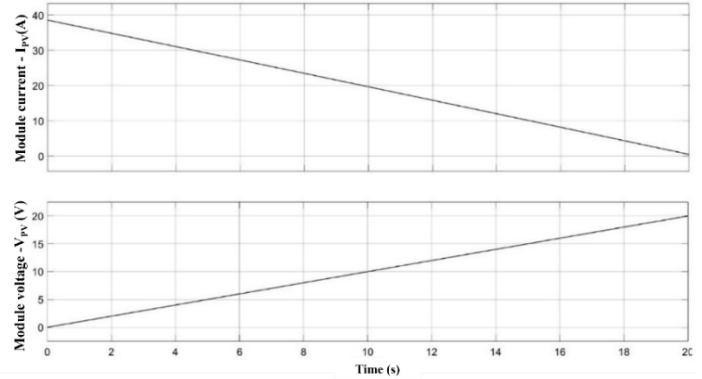
Figure 10. PV module current (I_{PV}) and voltage (V_{PV}) using 30 cells parallel.

The electric current generated from a power photovoltaic array in Figure 10 is used as an input signal changing in time with solar radiation. Based on this simulation results, it is observed that at the beginning of the simulation (0 s), the module current (I_{PV}) is 40 A, indicating a high initial current output from the PV system. At the same time, the module voltage (V_{PV}) is 0 V, suggesting that the voltage output is initially low. Over the course of the simulation from 0 to 20 s, the module current (I_{PV}) decreases gradually from 40 A to 0 A. This decrease in current indicates a reduction in the electrical output of the PV system over time. Concurrently, the module voltage (V_{PV}) increases steadily from 0 V to 20 V during the 20 s simulation period. This increase in voltage suggests that the voltage output of the PV system rises as the simulation progresses. These observations are consistent with the typical behaviour of a PV system. Initially, when there is sufficient sunlight, the PV system generates a high current but with a low voltage output. As time passes and the simulation progresses, the current output decreases while the voltage output increases, reflecting changes in the external conditions (e.g., solar irradiance, temperature) or the system's internal dynamics.
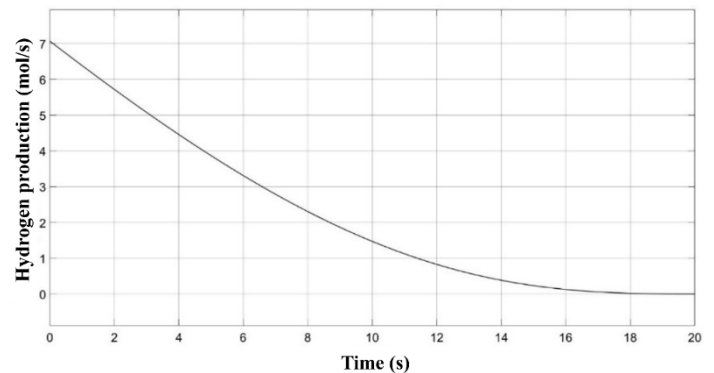
Figure 11.   Production of hydrogen in moles per second
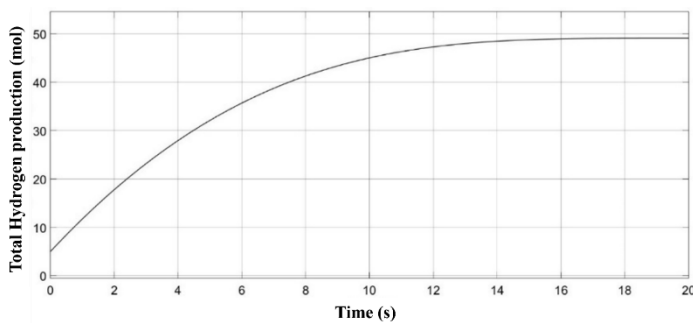
Figure 12. Total produced hydrogen in mol.

The results obtained during simulation of the hydrogen quantities are presented in Figure 11. Then the total produced hydrogen in depicted in Figure 12.

Figures 11 and 12 depict the hydrogen flow rates observed at various temperatures. Across the duration of the simulation, there is a noticeable decline in the rate of hydrogen production from an initial value of 7 mol/s to approximately 0 mol/s by the end of the 20 s. It can be attributed to various factors, including changes in operating conditions such as temperature variations or depletion of reactants over time. Additionally, it suggests a gradual decrease in the efficiency of the hydrogen generation process as the simulation progresses. While Figure 12 represents the cumulative amount of hydrogen produced over time in moles. Starting from an initial value of 5 mol at t = 0 s, the total produced hydrogen steadily increases throughout the simulation period, reaching a final value of approximately 50 mol at t = 20 s. This accumulation of hydrogen over time reflects the continuous operation of the hydrogen generation system and the progressive conversion of water into hydrogen gas. Despite the decrease in the rate of hydrogen production observed in Figure 11, the cumulative amount of hydrogen continues to rise due to the continuous operation of the system.

In addition, as the current increases, the hydrogen flow rate also increases, indicating a direct correlation between current supply and hydrogen production. The dissociation reaction responsible for breaking the bonds of water molecules is facilitated by the increasing current supply to the electrolyzer. Higher current densities lead to greater dissociation reactions, resulting in higher hydrogen flow rates.

4. Discussion

The study demonstrates the potential of harnessing solar energy for electrolysis, showcasing consistent hydrogen flow rates across diverse operational scenarios. This underscores the comparable performance of the integrated PV electrolysis system with prior research, as reported in the existing literature [18]. Through simulations, consistent hydrogen production rates are observed despite fluctuations in current supply and solar irradiance, aligning with observations from previous studies [19]. The comprehensive design model developed in the study serves as a springboard for future research avenues, such as maximizing hydrogen production efficiency and minimizing energy losses, as suggested in prior literature [20]. These endeavors aim to optimize the performance of PV-

electrolyzer systems and unlock the full potential of solar-driven hydrogen production. The findings not only highlight the viability of solar-powered electrolysis but also provide a solid groundwork for further advancements in renewable energy technology. By focusing on refining system efficiency and reducing energy wastage, a contribution can be made to a more sustainable energy landscape [21 – 22].

5. Conclusions

In this paper, the production of hydrogen through water electrolysis is explored, utilizing an alkaline electrolyzer in conjunction with a photovoltaic (PV) system. Central to the study was the development and modeling of PV panel and alkaline electrolyzer models within the Simpower Systems block of MATLAB/Simulink, facilitating the simulation and analysis of the hydrogen production process. Through rigorous simulations, the amount of hydrogen generated by the integrated PV-electrolyzer system under various operating conditions was quantified. This empirical data provides valuable insights into the system's performance and efficiency, serving as a foundational step towards optimizing hydrogen production processes. Moving forward, the research will extend to exploring energy storage solutions aimed at mitigating the technical challenges associated with solar energy, wind power, and other intermittent generators. By addressing the intermittency issues inherent in renewable energy sources, the aim is to facilitate their seamless integration with utility grids. Energy storage technologies offer a promising avenue for enhancing grid stability, reducing reliance on fossil fuels, and fostering the widespread adoption of renewable energy. By continuing to investigate and develop innovative energy storage solutions, the path can be paved for a more sustainable and resilient energy future. Through collaborative efforts across academia, industry, and government sectors, the transition towards a greener and more sustainable energy landscape can be accelerated, driving positive environmental and socio-economic impacts globally.

Conflict of Interest Statement

F.H and I.M. contributed equally. All authors have given approval to the final version of the manuscript. The authors declare that there is no conflict of interest in the study.

CRediT Author Statement

Fatima Haidar: Writing original draft- review & editing, Conceptualization, Supervision, Validation. **Imen Mrad:** Writing original draft; Data collection; Simulation, Validation. **Quang Truc Dam:** Writing original draft; Validation.

References

1. Aouali, F. Z., Becherif, M., Tabanjat, A., Emziane, M., Mohammedi, K., Krehi, S., & Khellaf, A. (2014). Modelling and Experimental Analysis of a PEM Electrolyser Powered by a Solar Photovoltaic Panel. Energy Procedia, 62, 714–722.

2. Hervello, M., Alfonsín, V., Sánchez, Á., Cancela, Á., & Rey, G. (2014). Simulation of a stand-alone renewable hydrogen system for residential supply. DYNA, 81(185), 116.

3. Kiaee, M., Cruden, A., Chladek, P., & Infield, D. (2015). Demonstration of the operation and performance of a pressurised alkaline electrolyser operating in the hydrogen fuelling station in Porsgrunn, Norway. Energy Conversion and Management, 94, 40–50.

4. Kamal, T., & Hassan, S. Z. (2016). Energy Management and Simulation of Photovoltaic/Hydrogen/Battery Hybrid Power System. Advances in Science, Technology and Engineering Systems Journal, 1(2), 11–18.

5. Awad, H., Abdalfatah, S., Hegazy, H., & Elkholy, E. E. (2019). Hybrid PV/FC System Design and Simulation. 2019 21st International Middle East Power Systems Conference (MEPCON), 1025–1030.

6. Zhou, T., & Francois, B. (2009). Modeling and control design of hydrogen production process for an active hydrogen/wind hybrid power system. International Journal of Hydrogen Energy, 34(1), 21–30.

7. Saeed, Eng. W., & Warkozek, Eng. G. (2015). Modeling and Analysis of Renewable PEM Fuel Cell System. Energy Procedia, 74, 87–101.

8. Awasthi, A., Scott, K., & Basu, S. (2011). Dynamic modeling and simulation of a proton exchange membrane electrolyzer for hydrogen production. International Journal of Hydrogen Energy, 36(22), 14779–14786.

9. Tijani, A. S., Yusup, N. A. B., & Rahim, A. H. A. (2014). Mathematical Modelling and Simulation Analysis of Advanced Alkaline Electrolyzer System for Hydrogen Production. Procedia Technology, 15, 798–806.

10. Lajnef, T., Abid, S., & Ammous, A. (2013). Modeling, Control, and Simulation of a Solar Hydrogen/Fuel Cell Hybrid Energy System for Grid-Connected Applications. Advances in Power Electronics, 1–9.

11. Ulleberg, O. (2003). Modeling of advanced alkaline electrolyzers: A system simulation approach. International Journal of Hydrogen Energy, 28(1), 21–33.

12. Cao, T.-F., Mu, Y.-T., Ding, J., Lin, H., He, Y.-L., & Tao, W.-Q. (2015). Modeling the temperature distribution and performance of a PEM fuel cell with thermal contact resistance. International Journal of Heat and Mass Transfer, 87, 544–556.

13. Megía, P. J., Vizcaíno, A. J., Calles, J. A., & Carrero, A. (2021). Hydrogen Production Technologies: From Fossil Fuels toward Renewable Sources. A Mini Review. Energy & Fuels, 35(20), 16403–16415.

14. Chowdhury, S., Chowdhury, S. P., Taylor, G. A., & Song, Y. H. (2008). Mathematical Modelling and Performance Evaluation of a Stand-Alone Polycrystalline PV Plant with MPPT Facility. 2008 IEEE Power and Energy Society General Meeting - Conversion and Delivery of Electrical Energy in the 21st Century, 1–7.

15. Pandiarajan, N., & Muthu, R. (2011). Mathematical modeling of photovoltaic module with Simulink. 2011 1st International Conference on Electrical Energy Systems, 258–263.

16. Jung, J.-H., & Ahmed, S. (2010). Model construction of single crystalline photovoltaic panels for real-time simulation. 2010 IEEE Energy Conversion Congress and Exposition, 342–349.

17. Bousseksou, O. (2024). Thermal modeling of solid hydrogen storage in a LaNi5 metal hydrid tank. Engineering Perspective, 1(1), 32–39.

18. Nasser, M., Megahed, T. F., Ookawara, S., & Hassan, H. (2022). A review of water electrolysis–based systems for hydrogen production using hybrid/solar/wind energy systems. Environmental Science and Pollution Research, 29(58), 86994–87018.

19. Fischer, M. (1986). Review of hydrogen production with photovoltaic electrolysis systems. International Journal of Hydrogen Energy, 11(8), 495–501.

20. Demirdelen, T., Ekinci, F., Mert, B. D., Karasu, İ., & Tümay, M. (2020). Green touch for hydrogen production via alkaline electrolysis: The semi-flexible PV panels mounted wind turbine design, production and performance analysis. International Journal of Hydrogen Energy, 45(18), 10680–10695.

21. Vinod, Kumar, R., & Singh, S. K. (2018). Solar photovoltaic modeling and simulation: As a renewable energy solution. Energy Reports, 4, 701–712.

22. Marocco, P., Gandiglio, M., & Santarelli, M. (2024). Optimal design of PV-based grid-connected hydrogen production systems. Journal of Cleaner Production, 434, 140007.

ENGINEERING PERSPECTIVE
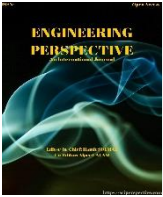
Study on Design Method of a Novel Precast Prestressing Composite Frame Based on African Manner

Jean Pierre Nsengimana[1*] iD

[1] *School of Civil Engineering of Southeast University, Nanjing, China*

ABSTRACT

Precast composite structures are new trend in construction technology in China due to their high sustainability and structural performance. As Chinese construction companies enter Africa continuously, the Chinese developed technologies are increasingly applied in Africa. A novel precast prestressing composite structure, developed in China, is believed to have a good prospect in Africa. In this study, a design method of the novel precast structure based on the African design system was developed to promote the application in Africa.

The structural design systems in Africa and China were compared to help designers know the difference between the two design systems and develop a better design method for the new precast prestressed composite frame in Africa. It can be found that the basic theory of the two design systems is similar, but the technical design parameters and equations are different.

The structural design method of the novel precast structure was built with African design system. The basic structural design steps based on the limit state method according to Eurocodes were established, and the seismic design process for the novel precast structure was also developed based on equivalent lateral seismic force method. Some important structural details of the novel frame for earthquakes based on African manner were presented.

The developed detailed design method of the novel structure was applied by designing a four storey novel building structure expected in Huye City at Southern Province of Rwanda. The design results were validated by comparison with results of the novel four storey building structure constructed in Suzhou, China. It is shown that both design systems provide safe design since all the results are within allowable limit, and the Chinese design method is more economical but the African design method is more conservative.

Keywords: Design method; precast composite structure; prestressing; African manner

1. Introduction

Since the African continent has become an urbanization and rising investment destination in the world, Chinese companies have been carrying out construction projects in different African countries in line with sustainable development. Chinese companies integration into African market is growing over years. Since 2005, China won 32% of their total international revenue from African countries [1].

In the construction industry in Africa, it was developed based on China relationship with African Countries, as a result, Chinese companies expanded across Africa in construction industry. Chinese Construction Firms(CCFs) have had a good record in Africa basically due to its advanced technology in construction projects, procurement of materials, financial sources and environmental safety. Recently, China has introduced belt and road initiative program which was intended to integrate Africa into Chinese constructed sustainable infrastructure development. Since 2000 to 2017, China choose belt and road initiative countries such as Djibouti, Ethiopia, Kenya and Tanzania to be given a loan linked to direct resource exploration and infrastructure projects usage. Due to that loan these countries received, some building and transportation projects have been implemented [2] by CCFs. A research showed a high competition where 40% of contracts for buildings and transportation projects in Africa won by CCFs [3].

A case study of Tanzania and Zambia showed a large amount of the incorporation of Chinese companies into construction industry of Africa, on the ground that the indigenous companies have lack of financial and technical capacity in major large scale projects, consequently, Chinese companies based on these countries across Africa have big natural resources and evenly large and stable market [4]. The Zambia's construction industry was developed and is being flourished by Chinese construction companies through bilateral cooperation between China and Zambia [5].

However, the CCFs face the same challenges as other construction companies such as political and economic instability, poor quality of local workforce and construction materials [6]. Especially, they are not confident to use local labor due to communication barrier and lack of technical technologies among African workforce. Not only this challenges, but also include low operation and maintenance skills which require a more conservative design with high safety [7].

On May 2, 2018, construction of the tall building shown in Figure 1 started in Egypt, and the 385 m high Iconic tower has offices, hotels and businesses. The composite tall building structure covers 65,000m^2 with 2 basements and 78 floors above ground level. The Chinese Company called China State Construction Engineering Corporation (CSCEC) is implementing the project. The exchange of ideas between Egyptian and Chinese engineers will improve the modern construction method and better cooperation in infrastructure development design.

Figure 1. Iconic Tower in CBD Egypt (385m high), photo taken June17, 2021 with view of modern buildings.

They exist different types of composite elements including steel-concrete composite, timber-concrete composite, steel-timber composite, and plastic-concrete composite. Steel-concrete composite is the composite element that is most commonly used in construction. Precast composite structure refers to the use of structural steel and precast concrete made together so that the structure behaves as one element. This precast composite structure has the purpose to use the best characteristic strength of both different materials and provide best performance that is more stronger than it had when the individual components been used together without monolithic liaison. The precast composite structure have great importance: shorten the time for construction, good performance and value, energy saving and emission reduction. In addition, the concrete encasement protect the structural steel from corrosion and fire and composite deck provide an integrated services within the channels.

There are numerical investigations on steel-concrete composite structures, the literature review for this study will focus on composite structural members such as concrete filled steel tube columns, precast hybrid steel–concrete beams and the steel-concrete composite connecting joints[8].

Concrete is a material that is strong in compression, but weak in tension. On the other hand, structural steel is very strong in tension, even when it is used in relatively small quantity. Steel-concrete composite uses compressive strength of concrete alongside structural steel's resistance to tension forces, and when they are bound together results in forming a very high stiff material unit. Due to the advantages such as fire resistance, combining high strength, long life capability and lightness of steel with stiffness, good ductility and damping, good energy dissipation capacities and economy of concrete, Steel-concrete composite construction has been increasingly used over decades in building industry, bridges, high rise building construction and car park[8,9].

Referring to the Figure 2, some typical examples of composite subassembly are presented such as composite beam, composite slab and composite columns.
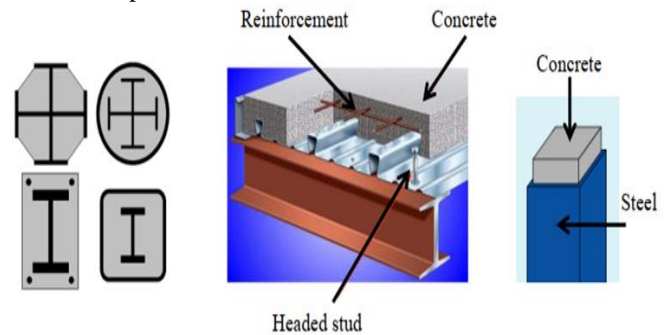
Figure 2. Details of a composite beam, slab and columns [9].
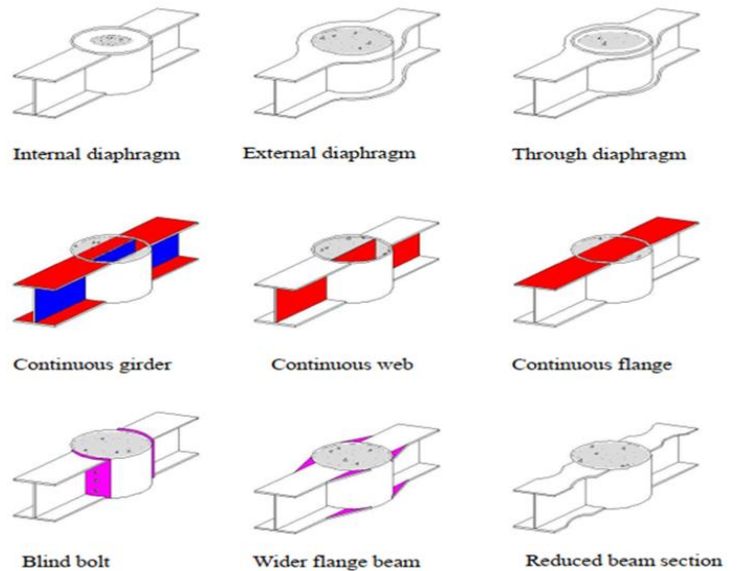
Figure 3. common CFST joint configurations [9].

Steel–concrete composite joints are accumulation of parts that transfer forces from one member to others, the forces and moments of the members must be resisted at the point of joint. Eurocode4(EN1994-1-1.5.2.8)[10] provided definition of composite joint: a joint between a composite member and another composite, steel or reinforced concrete member, in which reinforcement is considered in design for the resistance and stiffness of the joint. For the joints to respond effectively in moment resisting frames, they have to satisfy the following criteria:

1.The applied design moment should be always less than the moment capacity of the joint.

2. The joint must have sufficient rotational stiffness.

3. The joint should have adequate rotational capacity (subsequently referred to as ductility) to allow the connection to work as plastic hinge.

4. The applied shear resistance must be less than the shear resistance of the joint. Refer to the Figure 3.

S. Feng, D. Guan, Z.Guo et al [11] developed the assembly of the joint between a new hybrid H-steel precast concrete (HSPC) beam and concrete-encased filled steel tubular (CFST) column as shown in Figure 5 and 6. It was developed through laboratory experimental set up in order to assess the seismic performance based on ductility, energy dissipation capacity, failure pattern, stiffness degradation and hysteresis curve of the joint. The HSPC was connected to CFST via cantilever H-steel section [12, 13-14].

To assess the suitability of the joint, the cyclic load reversed test was conducted under use of three types of cantilever H-steel beam: untreated beam section (EJ-1), reduced beam section (RBS) (EJ-2) and open web beam (OWB) (EJ-3). The results indicated that the hysteretic bahaviour stability of the joint with reduced beam section occurred at a drift ratio of up to 4.75% (refer to Figure 4) and a significant ductility and the cumulative energy dissipation capacity was 8.8 times that of original specimen. Conversely, the enhancement in the steel section with OWB in subassembly was poor compared to the original specimen. Therefore, the subassembly with reduced beam section(RBS) was considered to resist in seismic region. Refer to the Figure 4 below [15, 16].

Design methods of the steel-concrete composite design is a crucial step in steel-composite building construction. The steel-concrete composite design is done to make safer the building structure. The major structural composite members in steel-concrete composite structures are reinforced against bending and vertical shear forces. The shear connector are designed and incorporated between the surface of steel and concrete for composite beam and slab [17,18].
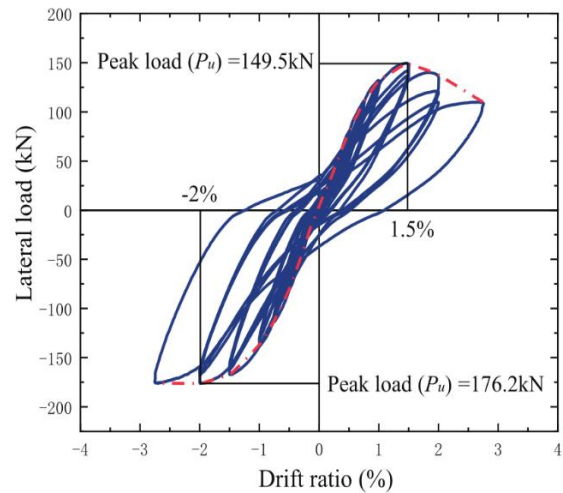
(a)   Specimen EJ-1
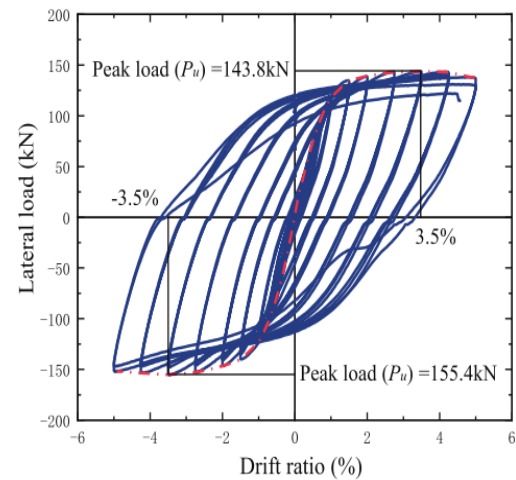
(b)   Specimen EJ-2
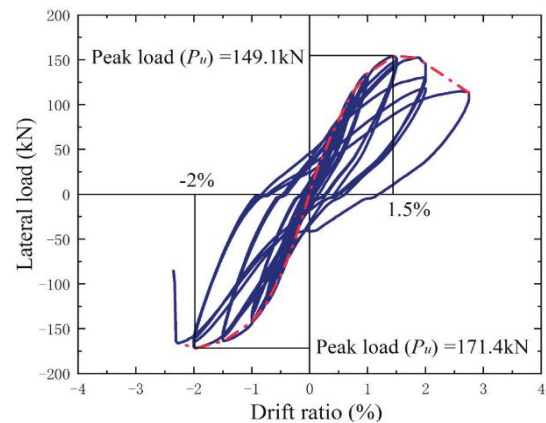
(c) Specimen EJ-3

Figure 4. Hysteresis curves of specimens under cyclic loading [11].

71
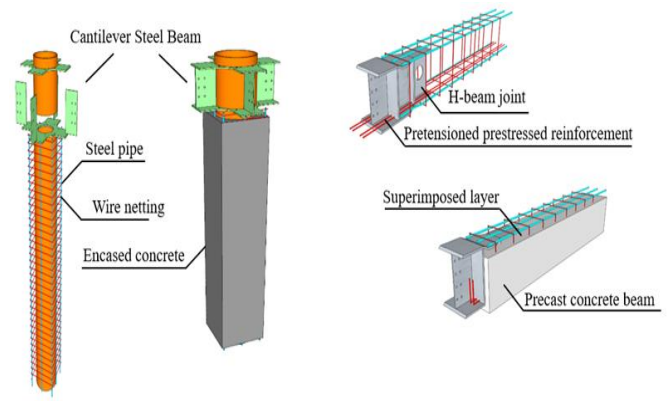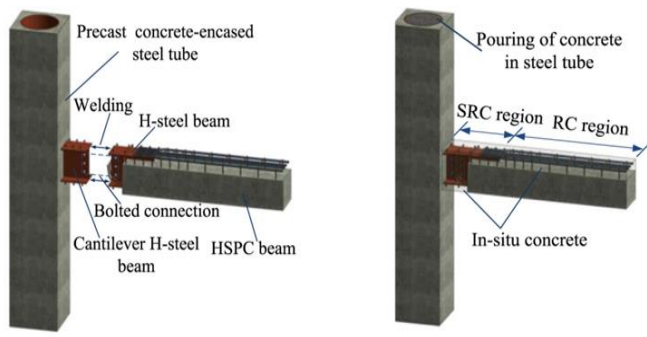
(a) Precast joint in assembly   (b) Precast joint after assembly

Figure5. Construction processes of the developed precast joint CFST column and HSPC beam [11].
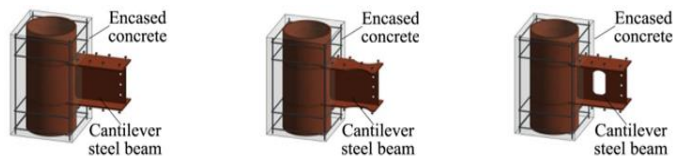
(a) untreated beam   (b) RBS steel beam   (c) OBW steel beam

Figure 6. Concrete encased-CFST columns with cantilever H-steel beams [11].

In the common analysis of composite sections, the following conditions are assumed :(EN1994-1-1), as follows:

1.Concerete is assumed to carry zero tensile stresses in both elastic theory and plastic theory.

2. In elastic theory, concrete in compression is transformed into an equivalent area of steel by dividing its breadth by the modular ratio E_a/E_c.

3. Plane sections of the structural steel and reinforced concrete parts of a composite section each before bending remain plane after bending [19,20-22].

4. in plastic theory only,

a) Concrete in compression resist a stress of $0.85f_{cd}$ where $f_{cd}=f_{ck}/\gamma_C$, which does not change over the whole depth between the plastic neutral axis and the most compressed fibre of the concrete.

b) The structural steel member is stressed to its design yield strength $f_{yd}=f_y/\gamma_A$. Transformed sections are not used.

2. The novel precast prestressing composite frame

As the development of the architectural industrialization career in China, tremendous precast structures are designed and constructed across different areas of China, including precast concrete structures, precast steel structures and precast timber structures. However, the widely-applied precast concrete structures are emulative system, of which the construction efficiency is relatively low relying on a large amount of labors. Precast steel structures require coatings and other protective measures for fires and corrosions, making the construction cost relatively high. Therefore, many investigators and engineers are developing and seeking a satisfactory precast structure.

(a) Details of the components

(b) Connection details of the columns and beams

(c) The constructing stage of the structure

Figure 7. The novel precast prestressing composite frame in Suzhou, China

A novel precast prestressing composite structure, which was believed to have a good prospect of application, was developed by the research group that the author belonged to in School of Civil Engineering at Southeast University, China. The columns are made of concrete filled steel tube (CFST) surrounded by reinforced concrete wall for fire proofing. The beams are precast prestressed beams in the middle span and the ends are made with H-steel beam connection embedded into precast beam in the joints. A through diaphragm was used to connect either circular or rec-

tangular steel tube column with H-steel cantilever beam embedded in precast prestressed beam as shown in the Figure7. At construction sites, the precast prestressed composite beams are connected to the precast composite columns through bolts for the webs and weldings for the flanges.The columns are connected with each other by steel plates welded at columns end sides and with bolts to connect steel plates at both columns ends connection. After the installation of slabs, concrete is poured for the monolithic layers. This novel structure has been constructed as an office building by ZYF Company in Suzhou, China, proving the high efficient construction and satisfactory load-bearing capacity of static loadings.

The use of precast prestressing steel-concrete composite units is essential in promoting the sustainability and resilience of infrastructure in Africa and around the world in general. In addition, precast units are environmental friendly and reusable. Prestressing units will allow load balance to be placed in the structure to anticipate service loads. This will bring many benefits to the building frame such as:

1. Span can be increased without increasing structural depth
The load balance reduces the service deflection, which causes the span length to increase without the need for structural depth increase, and the number of supports is reduced.

2. Reduction of structural thickness dimensions
The lower service deflection allows the use of thin structural sections in the building that lead to more service areas.

3. Construction time is reduced;
The precast beam can be installed and connected to the precast column in the similar way with the quick construction of steel structures. The precast units are fully stretched and braced within five days, after which a few formworks are removed and can be quickly used for the next phase of building construction. Alternatively, when the precast unit is manufactured at the factory, it must be installed in a very short time with minimal labor cost.

4. Cost savings for fire-proof materials;
For the steel components in this structure, the concrete is poured to encase them in a manufacturing factory as fire-proof materials, which is cheap and easy to be prefabricated. The layers of the fire-proof concrete outside the steel elements commonly remain approximately 50 mm. Therefore, the steel components are protected well with relatively low costs.

For this novel precast prestressing composite frame structure, as the advantage of the force combination; the encased steel is more protected against corrosion and fire, and no maintenance is required. The concrete inside rectangular steel tube column is well confined and no need of additional rebar in concrete because the column bearing capacity is adequate. The H-steel beam section in the ends of beam in the connection between beam and column is more strong compared to other connection in precast structures. The connection of column with each other is more strong compared to other connection in precast structures. It consists of steel plate welded on column sides at end of each column and the connection is made of other steel plate fixed at end of each side of columns with the help of bolts.

3. Materials and Method

3.1. Materials

The novel precast prestressed composite frame was developed and applied in China. A comparison was made between the structural design system in Africa and China to know the difference, which can help develop a better design method for the new precast prestressed composite frame in Africa. In general, the structural design system in Africa is based on Eurocode0 for the basis of structural design, Eurocode1 for the loads on structures, Eurocode2 for the design of reinforced concrete structures, Eurocode3 for the design of structural steel structures, and Eurocode4 for the design of steel-concrete composite structures, and Eurocode8 for the design of earthquake resistant structures in most of the African countries.

There are many design codes for structures in China. In this paper, the general structural design system in China is thought to be based on the several basic design codes, i.e., GB50010 Code for the design of reinforced concrete structures, GB50009 Load code for design of the building structures, GB50017 Code for design of steel structures, JGJ138 Code for design of composite steel structures and GB50011 Code for seismic design of buildings. Therefore, the comparison of both Eurocodes and Chinese codes was employed to help Chinese and African designers to know the two structural design systems well and the difference between them, and the developed design method according to African manner was based on limit state method and design steps were proposed.

3.2. Method

The possible design method based on African manner is the limit state method according to Eurocode0, Eurocode1, Eurocode2, Eurocode3, Eurocode4 and Eurocode8. A three-D model was transformed into a two-Dimensional plane frame. Computer program (ETABS software) can be used to assist in analysis and design of the frame members based on stiffness method in Rwanda, Africa. The frame member sizes are selected, loads of the frame are estimated, bending moment, axial and shear forces are computed, and prestress is applied. Then the planned structure is checked for both ultimate limit state and serviceability limit state. The analysis and design is done based on the assumption that the materials behaviour are linear and elastic [23]. The design method of critical elements such as composite beam, columns, and connections are discussed in design steps below.

3.2.1. Basic design steps of the novel structure based on African manner

At the initial stage, the structural modelling of the proposed precast prestressing composite frame was developed. The simplified structural analytical model was developed based on load distribution, geometry of the structure, its supports and the estimated deformation of the structure [23]. Then, the critical elements can be designed following the design steps and design formulas which are expressed below.

Step1.Establishment of the structural layout plan

Step2.Identification of the Elements of the frame and materials properties

Step 3.Determination of the characteristic values of loads

Step 4. Preliminary design of member sizes of a structure.

1. Preliminary design of beams

The basic parameter of the beam can be obtained using the following expression first:

$$Z_{btm} \geq \frac{M_T - 0.85M_0}{f_{ct,t} - 0.85f_{cc,0}} \tag{1}$$

where Z_{btm} is the section modulus at the bottom fiber of the beam; M_T is the moment due to total service load; M_0 is the moment due to selfweight; $f_{ct,t}$ is the tensile stress limit of concrete at bottom fibre after prestress forces finish transfering; $f_{cc,0}$ is the compressive stress limit of concrete at bottom at prestress forces finish transferring. According to Code EC2, the values of $f_{ct,t}, f_{ct,0}$, $f_{cc,t}$ and $f_{cc,0}$ are concrete stress limit which are selected for design.

Then the trial depth of beam section is given by the following expression:

$$h \geq \sqrt{Z_{btm} \times 6/b_w} \tag{2}$$

where b_w is the width of beam section which is assumed according ordinary details of beams[23].

Check that the deflection of the initially-determined beam according to the requirement, i.e., the trial section should satisfy the following expression:

$$I \geq \beta \frac{W_{tot} \times l^4}{E_{cm} V_{max}} \tag{3}$$

where W_{tot} is the total unbalance load; L is the span of the beam; E_{cm} is the elastic modulus of concrete; V_{max} is the limiting maximum deflection, $l/500$; and β is deflection coefficient equal to 5/384.

Determine prestressing force and eccentricity required at midspan of the beam. The section properties α_{top} and α_{btm} are obtained by the expressions, i.e., $\alpha_{top} = A/Z_{top}$ and $\alpha_{btm} = A/Z_{btm}$, where A: Cross section area, α_{top}: the ratio of area to section modulus at top fiber of beam and α_{btm}: the ratio of area to section modulus at bottom fiber of beam, and Z_{top}: section modulus at top fiber of beam [23].

The following expression provides the upper and lower limits of prestress at transfer and after transfer, respectively: at transfer

$$P_{mo} \leq \frac{Af_{ct,0} + \alpha_{top}M_0}{\alpha_{top}e - 1} \tag{4}$$

$$P_{mo} \leq \frac{-Af_{cc,0} + \alpha_{btm}M_0}{\alpha_{btm}e + 1} \tag{5}$$

after transfer

$$P_{mo} \geq \frac{-Af_{ct,t} + \alpha_{btm}M_T}{\Omega(\alpha_{btm}e + 1)} \tag{6}$$

$$P_{mo} \geq \frac{Af_{cc,t} + \alpha_{top}M_T}{\Omega(\alpha_{top}e - 1)} \tag{7}$$

where Ω is time-dependent loss of prestress and e is excentricity to resultant prestressing force; P_{mo} is prestress force applied $f_{ct,t}$: the tensile strength of concrete after transfer, $f_{ct,0}$:the tensile

strength of concrete at transfer , $f_{cc,t}$:compressive strength of concrete after transfer and $f_{cc,0}$:compressive strength of concrete at transfer[23,24-26]

The two ends of beam are made of short H-steel beam embedded into concrete precast prestressed beam. The top and bottom steel reinforcement are welded on top and bottom of H-steel beam flange with the help of stud connectors. According to expermiment done [27]. The connection between steel reinforced concrete (SRC) region and reinforced concrete (RC) region is designed following the model of the experiment done. Refer to Figure 8, below [28, 29-30].
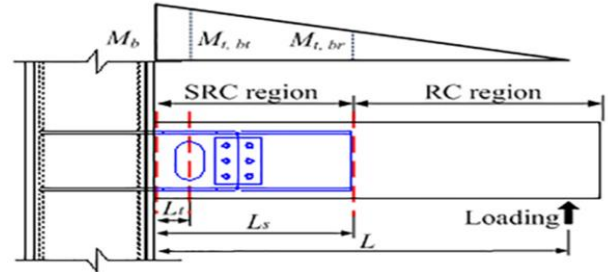
Figure8. Calculation sketch of hybride steel precast concrete (HSPC) beam [11].

The distance L_t, L_s, L is taken similar to that one in experiment. However, the dimensions of H-steel beam section and concerete filled rectangular steel tube section can be different according to the loading of the structure being designed. In Figure 8, M_b is the ultimate flexural capacity at the interface between beam and column, and can be calculated using EN1994-1-1, as follows:

$$M_b = F_{Rd} \times z \tag{8}$$

Where F_{Rd} is the axial force resistance, and z: lever arm. Details can be seen in Table 1 below.

Table 1.welded connection at the interface between beam and column (EN1993-1-8, 6.2.7)

Type of connection	Centre of compression	Lever arm	Force distributions
a) Welded connection	In line with the mid thickness of the compression flange	$z = h - t_{fb}$ h is the depth of the connected beam t_{fb} is the thickness of the beam flange	
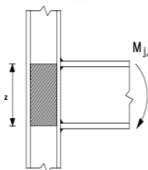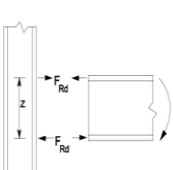
In Figure 8, above, $M_{t,bt}$: is theoretical flexural resistance in the central section of H-steel region; $M_{t,br}$: is the theoretical flexural resistance of the end section at RC region; M_{bt}: is the ultimate flexural capacity of the central section of H-steel beam; M_{br} is the ultimate flexural capacity of the end section at RC region.

For the plastic hinges to be formed within SRC region, the following equations must be followed:

$$M_{bt} / M_{t,bt} \leq 1 \tag{9}$$

$$M_{br} / M_{t,br} \geq 1 \tag{10}$$

2. Preliminary design of column

The size of the column is derivered from plastic resistance to compression $N_{pl,Rd}$ of a composite cross-section which is expressed by the following equation:

$$N_{pl,Rd} = \eta_a A_a f_{yd} + A_c f_{cd} \left(1 + \eta_c \frac{t}{d} \frac{f_y}{f_{ck}}\right) \quad (11)$$

Where $N_{pl,Rd}$: plastic resistance to compression,t: thickness of steel tube ,d:diameter of steel tube , A_a: cross section area of steel f_{yd}:design tensile strength of steel, A_c:cross section area of concrete, f_{cd}:design compression strength of concrete,f_y:yield tensile strength of steel,f_{ck}:characteristic tensile strength of steel, η_a and η_c are reduction coefficients of steel and concrete respectively. In Eq.(11), no longitudinal steel reinforcement is considered according to the novel precast composite structure.

The increase in strength of concrete due to confinement in concrete filled circular tube may be taken into account if the relative slenderness λ defined in EN1994-1,Clause 6.7.3.3(2) does not exceed 0.5 and e/d <0.1, where e is the eccentricity of loading given by M_{Ed} /N_{Ed} and d is the external diameter of the column. Otherwise stated, for e/d > 0.1, the values of η_a = 1.0 and η_c = 0, then $N_{pl,Rd}$ should be calculated by the following equation:

$$N_{pl,Rd} = A_a f_{yd} + A_c f_{cd} \quad (12)$$

Step 5. Load estimation

Step 6. Estimation of load combination for ultimate limit state design

The following equations can be used to determine the design ultimate load (W_{Ed})：

$$W_{Ed} = 1.35 \times Deadload + 1.5 \times Liveload \quad (13)$$

$$W_{Ed} = 1.35 \times Dead\ load + \psi_0, L \times Live\ Load \quad (14)$$

where ψ_0 is the factor for buildings according to EC0 (1990:2001,Table A1.1).

Step 7. Design of beams

1. Design of precast prestressing reinforcement

Using the above Equations 4 through 7, the minimum required prestressing force at mid-span that satisfies all four equations can be obtained with the eccentricity to the resulting prestressing force at middle span of beam.

The immediate losses at mid-span is assumed and the jacking force is determined as following :

$$P_j = \frac{P_{mo}}{\Omega} \quad (15)$$

where P_j: is the jacking force, P_{mo}:applied prestress.

Assuming a seven-wires strand of 12.7mm diameter, the maximum stress in the tendon at jacking is the smaller value of *0.8 f_{pk}* or *0.9 $f_{p0.1k}$*, where f_{pk} is the characteristic strength of strand, and $f_{p0.1k}$ is 0.1% proof characteristic strength of strand, hence the jacking force per strand, $P_{jstrand}$ can be *0.9 $f_{p0.1k}$ *Area of strand*, and then the minimum number of seven wire strands can be found by jacking force over jacking force per strand.

2. Design of non prestressing reinforcement
a) Design of non prestressing steel rebars in tension

Considering a section of beam, effective prestress, $P_{m,t}$, and the area of prestressing steel, A_p, the cross section have been designed to satisfy the serviceability of the reqirements of the member. With the stress-srain relationship according to EN1992-1-1, and the design moment resistance of the section is calculated as the following equation:

$$M_{Rd1} = \sigma_{pud1} A_p \left(d_p - \frac{\lambda_{x1}}{2}\right) \quad (16)$$

where σ_{pud1}:stress in strand,A_p:area of strand,d_p:effective depth to strand,x_1:depth to neutral axis, λ:reduction coefficient.If the design resistance(M_{Rd1}) is greater or equal to the design ultimate moment(M_{Ed}), no additional non-prestressing reinforcement is needed, but if M_{Rd1} is less than M_{Ed}, additional non-presstresing reinforcement is required. Hence,

$$A_s \geq \frac{M_{Ed} - M_{Rd1}}{f_{yd} \times z_2} \quad (17)$$

where M_{Ed} is the design ultimate moment; f_{yd} is the yield strength of reinforcement; Z is the lever arm between the design tension force in the additional steel; F_{sd} and the equal and opposite compression force F_{cd2} which results in the increase in the depth of compressive stress block (refer to Figure 9 below) and A_s is the area of reinforcement.

The lever arm between the design tension force in the additional steel can be obtained refering to Figure 9 below as:

$$Z_2 = 0.9(d_s - \lambda_{x1}) \quad (18)$$

where d_s: effective depth to reinforcement. Non- prestrssing reinforcements are provided in the tensile zone of the section of a beam to provide additional flexural strength when the strength provided by the prestressing steel is not enough. It improves also crack control when cracking is anticipated at service loads.
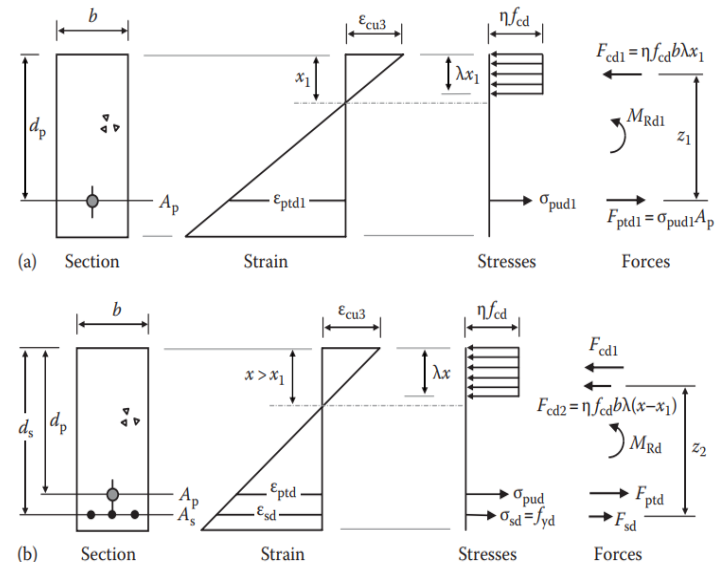

Figure 9.Cross section containing tensile reinforcement [23].

b) Design of non-prestressing steel rebars in compression

Considering the rectangular section of a beam below, the minimum area of additional tensile reinforcement is given by the following expression:

$$A_{s(2)} = \frac{M_{Ed} - M_{Rd1}}{\sigma_{sd(2)}(d_{s(2)} - d_{s(1)})} \qquad (19)$$

Where $\sigma_{sd(2)}$:design stress in tension rebar(refer to Figure 10).The minimum area of additional compression reinforcement is given by the following expression:

$$A_{s(1)} = \frac{A_{S(2)}\sigma_{sd(2)}}{\sigma_{sd(1)}} \qquad (20)$$

and the strain in both compression and tension reinforcement can be greater than the strain in steel, hence the steel have yielded.

$$\varepsilon_{sd(1)} = \frac{\varepsilon_{cu3}\ (x - d_{s(1)})}{x} \qquad (21)$$

$$\varepsilon_{sd(2)} = \frac{\varepsilon_{cu3}\ (d_{s(2)} - x)}{x} \qquad (22)$$

where $d_{s(1)}$:effective depth to compression rebar, $d_{s(2)}$:effective depth to tension rebar,ε_{cu3}:strain of concrete $\varepsilon_{sd(1)}$:strain of compression rebar, and $\varepsilon_{sd(2)}$:strain of tension rebar. Non- prestressing reinforcement are provided in top of the section to not only improve the strength in compression zone, but also increase the curvature at failure and improve ductility. It reduces long-term deflection due to creep and shrinkage, hence, improving serviceability. Compression reinforcements are also provided to enhance anchorage and bearing for the transverse reinforcement in beams. Closely stirrups are used to laterally brace the highly stressed bars in compression and prevent them from buckling outward [31].
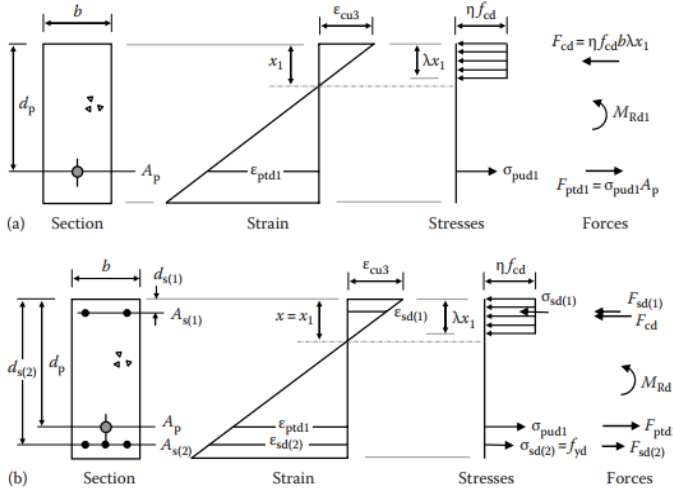
Figure 10, doubly reinforced section [23]

3. Check of the resistance to bending at mid-span

The design load W_{Ed} is found by using Equation 13 or 14 in Step 6 and the design moment (M_{Ed}) at mid span is found by using this expression:

$$M_{Ed} = \frac{W_{Ed}L^2}{8} \qquad (23)$$

The ultimate resistance moment of a rectangular section containing both prestressing steel and non prestressing steel is found by this expression:

$$M_{Rd} = \sigma_{upd}A_p\left(d_p - \frac{\lambda x}{2}\right) + f_{yd}A_s\left(d_s - \frac{\lambda x}{2}\right) \qquad (24)$$

where $x = \frac{f_{pd}\ A_p}{\eta f_{cd}b\lambda}$ is the depth to the neutral axis of the section,

$f_{pd} = 0.9 f_{pk}/\gamma_s$ is the design strength of prestressing steel, A_p is area of prestressing steel, f_{cd} is the design compressive strength of concrete and b is the width of beam section, d_p and d_s are effective depth to prestressing steel and non prestressing steel, respectively.

For a section with non prestressing steel, M_{Rd} should be greater than M_{Ed}, which can be computered as follows:

$$M_{Rd} = \sigma_{upd}A_p\left(d_p - \frac{\lambda x}{2}\right) \qquad (25)$$

No non-prestressing steel is required for the section, the section has adequate flexural strength with ductility. Otherwise, the section will require non prestressing steel reinforcement.

4. Check of shear resistance

The shear is checked at 1 m and 2 m from the face of the column support , and whether the shear resistance of the beam is greater than the design shear ,$V_{Rd,c} > V_{Ed}$, should be checked. Shear resistance should be:

$$V_{Rd,c} = \frac{Ib_w}{S}\sqrt{(f_{Ctd})^2 + \alpha_1\sigma_{Cp}\ f_{Ctd}} \qquad (26)$$

where S:is the first moment area of the section, I is the second moment area of the section, σ_{Cp}: is concrete compressive stress due to axial load and prestressing, f_{Ctd} is design concrete tensile strength ,b_w:width of beam and $\alpha_1 = l_x/l_{pt2} \leq 1.0$ a reduction coefficient.

5. Minimum clear spacing between pretensioned tendons

Horizontal clear spacing of between pretensioned tendon should be greater than the maximum of $d_g + 5$, 2Φ and 20mm, and vertical clear spacing be greater than the maximum of d_g and 2Φ, where Φ is diameter of pretensioned tendon and d_g is maximum size of aggreagates[31].

6. Design of ends connections of beam

According to Figure 8, the value of M_{bt} and M_{br} can be calculated assuming the rectangular stress block for composite beam in EN1994-1-1 in similar way as the experiment done(Feng et al., 2021). M_{bt} can be obtained based on that the neutral axis is within the web of the H-steel beam and that the sectional area of the top steel flange is equal to that of bottom steel flange. Considering force equilibrium, the equation for reduced H-steel beam section(RBS) as per previous experiment can be obtained as follow:

$$f_{cc}bc + f_{aw}A_{w,co} = f_{aw}A_{w,t} \qquad (27)$$

The equation for RBS region is obtained considering the moment equilibrium:

$M_{bt} = f_{af}A_{bf}(h-c-a_{s,t}) +0.5f_{aw} A_{w,t} (h-c-a_{s,t}) +f_{af}A_{bf}(c-$

$a_{s,co})+0.5f_{aw}A_{w,co}(c-a_{s,co})+0.5f_{cc} bc^2$ (28)

where f_{cc} is the axial compressive strength of concrete that is determined as $0.85f_{cd}$, f_{af} and f_{aw} are the yield strengths of the flange and the web in H-steel, respectively; $a_{s,t}$ is the distance between the flange of H-steel in the tension zone and the tensile edge of the cross section; $a_{s,co}$ is the distance between the flange of H-steel in the compression zone and the compressed edge of the cross section; c represent the depth of the neutral axis. Moreover, A_{uf} and A_{bf} are the sectional areas of the upper and bottom flanges, respectively, in H-steel. $A_{w,co}$ and $A_{w,t}$ denote the sectional areas of the beam web in the compression and tension zones, respectively (refer to Figure 11).
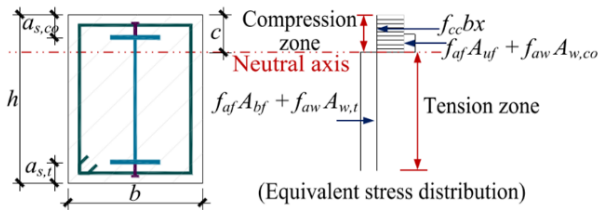

Figure 11. Center cross-section of the reduced beam section (RBS) [11].

The Figure 11 can be used to calculate the flexural resistance under sagging moment

To ensure good strength of the connection between the H-steel beam and RC beam, it must satisfy:

$A_s \geq \dfrac{f_{af} A_f (L-L_S)}{f_s (L-L_t)}$ (29)

where A_s is the area of steel reinforcement, f_{af} is the yield strength of steel and ,A_f is the sectional area of the steel flange, L is the distance from the face of column to the point of loading, L_s is the distance from face of column to the end of RC region, and L_t is the distance from face of column to center of H-steel section beam on Figure 8, above.

The required area of the H-steel A_a is determined by

$A_a f_{yd} (h_a+h_t-h_c/2) \geq M_{Ed}$ (30)

Where A_a: cross section area of steel, f_{yd}: design tensile strength of steel, h_a : depth of steel section h_t:thickness of slab, h_c:thickness of overtoping slab, and M_{Ed}:design moment.

Step 8. Design of composite column

The ultimate moment of resistance (M_u) can be calculated based on stress block diagram for concrete filled rectangular steel tube columns according to BS5400: Part5,C.4.2.5[32] as follows

$M_u = 0.91f_y\left[A_S \dfrac{(h-d_c)}{2} + b_t t_f (t_f + d_c)\right]$ (31)

$d_c = \dfrac{A_S-2b_f t_f}{(b\rho+4t_f)}$ (32)

$\rho = \dfrac{0.4f_{cu}}{0.91f_y}$ (33)

where A_s is area of rolled steel section; h is depth of concrete in filled rectangular hollow section, d_c is depth to the neutral axis from most compressed face of concrete; t_f is the average thickness of the flange of steel section; b_f is the external dimension of width of rectangular hollow section; ρ is the ratio of the average compressive stress in the concrete at failure to the design yield strength of the steel.
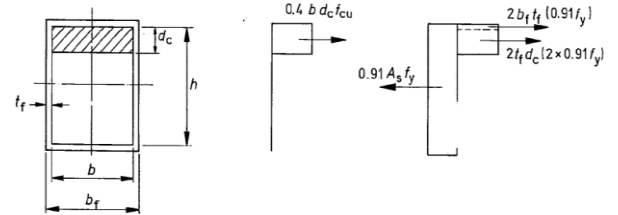
Figure 12. Force diagram for calculating M_u [32].

Step 9. Design of beam to column connections

1. Connections between concrete filled steel tube columns and H steel beams

According to the provision given in EN1993-1-8, steel joint design method can also apply to steel-conrete composite joint design in EN1994-1-1. In the beam-column connection, an H-steel beam is welded onto column by inner diaphragms. The H-steel beam is connected to precast prestressing beam by means of welding H-steel flange with both top and bottom steel reinforcement in precast prestressing beam. At the top of H-steel beam, there is shear studs to assist in preventing horizontal slide between beam and top slab. The H-steel beam embedded on the column and the one embedded in beam are connected by means of welds at top flanges and web plate with bolts at both web sides. The dimension of H-Steel beam are obtained from steel profile data base (Europian beam). To ensure enough strength of connection between the H-steel beam and RC beam , the total area of reinforcement that transmit normal stress to the top and bottom of the beam should be greater or equal to sectional area of the H-steel flange.The design resistance of bolts are given in Table 3.4 of EN1993-1-8:2003[33].

Headed stud connectors are provided and can have the following dimensions: $h>3d$, $d_h >1.5d$ and $h_d > 0.4d$, where h is overall height of stud, d_h is diameter of head of stud, d is diameter of shank of stud, h_d is depth of head of stud (EN1994-1-1:2004,Clause 6.6.5.7). For welded stud on top of flange of H steel beam, the diameter of welded stud should not exceed $1.5t_f$, where t_f is the thickness of the flange, and the spacing of shear stud should not be less than $5d$ in the direction of shear force and $2.5d$ in the transverse direction of shear force in solid slabs and $4d$ in other cases (EN1994-1-1:2004, Clause 6.6.5.7). The design shear resistance of headed stud should satisfy this expression:

$P_{Rd} = \dfrac{0.8f_u \pi d^2/4}{\gamma_v}$ (34)

Where f_u is the ultimate tensile strength of the material of stud not greater than $500N/mm^2$, d is the diameter of the shank of the stud, $16mm \leq d \leq 25mm$ and γ_v is the partial factor 1.25 (EN1994-1-1:2004, Clause 6.6.5.7)

2. Resistance of welded joints between H-steel beams and Rectangular hollow sectional tube columns

The design resistance of welded joints connecting H-steel beams to (rectangular hollow section (RHS) member is given in EN1993-1-8, Table 7.13)[33].The design internal axial force ($N_{1,Ed}$) should not exceed the design axial resistance ($N_{1,Rd}$) of welded joint $N_{1,Rd} > N_{1,Ed,}$

$$N_{1,Rd} = f_{y0} t_0 (2t_1 + 10t_0)/\gamma_{M5} \tag{35}$$

$$M_{ip,1,Rd} = N_{1,Rd}(h_1 - t_1) \tag{36}$$

details are found in the Table 7.13 of EN1993-1-8,

4. Resistance of bolts in beam to column bolted connection

The design resistance of bolts in beam to column connection is given in EN1993-1-8, clause 3.1.1.(3). The yield strength (f_{yb}) and the ultimate tensile strength (f_{ub}) of bolts of classes: 4.6, 5.6, 6.8,8.8 and 10.9 are listed in Table 3.1 of EN1993-1-8. These values in Table 3.1 are taken as the characteristic values in calculations [33, 34].

a) When the bolts are in shear and tension

When the bolts are in shear, it should be designed as bearing type in category A(EN1993-1-8,clause 3.4.1(1)(a). When the bolts are in tension, it should be designed as non-preloaded in category D(EN1993-1-8,clause 3.4.2(1)(a), EN1993-1-8, Table 3.2,category of bolted connections.

The following formulas are adopted for both bolts in shear and tension resistance.

(i) For bolts in shear

$F_{v,Ed} \leq F_{v,Rd}$ and $F_{v,Ed} \leq F_{b,Rd}$,

(ii) For bolts in tension

$F_{t,Ed} \leq F_{t,Rd}$ and $F_{t,Ed} \leq B_{p,Rd}$,

b) Position of holes for bolts on the plate

According to EN1993-1-8, the minimum and maximum, end and end edges distances are provided as following:
Minimum end distance $e_1 = 1.2d_o$,maximum $e_1 = 4t+40mm$, where d_o is the diameter of hole and t is the thickness of the thinner outer connected part. Figure 13 shows the position of the holes.
Minimum end distance $e_2 = 1.2d_o$, maximum $e_2 = 4t +40mm$.
Minimum spacing $p_1 = 2.2d_o$, maximum spacing $p_1 = 14t$ or $200mm$.
Minimum spacing $p_2 = 2.4d_o$, maximum spacing $p_2 = 14t$ or $200mm$.
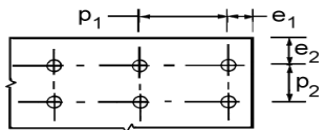
Figure 13. Position of hole for bolts [33].

c) Design resistance of bolt

Based on EN1993-1-8, Table 3.4, the formulas for design resistance of bolts in shear, tension and bearing are provided as following:
(i) Bolts in shear resistance
The shear resistance per shear plane can be obtained as:

$$F_{v,Rd} = \frac{\alpha_v f_{ub} A}{\gamma_{M2}} \tag{37}$$

Where the shear plane passes through the threaded portion of the bolt (A is the tensile stress area of the bolt A_S).

$\alpha_v = 0.6$ for bolts of classes 4.6,5.6, and 8.8

$\alpha_v = 0.5$ for bolts of classes 4.8, 5.8,6.8,and 10.9

Where the shear plane passes through the unthreaded portion of the bolt (A is the gross cross section of the bolt) $\alpha_v = 0.6$
(ii) Bolt in tension resistance

$$F_{t,Rd} = \frac{k_2 f_{ub} A_S}{\gamma_{M2}} \tag{38}$$

Where $k_2 = 0.9$

$$B_{p,Rd} = 0.6 \Pi d_m t_p f_u / \gamma_{M2} \tag{39}$$

$B_{p,Rd}$ is punching shear resistance , d_m is diameter of bolt, t_p is threaded height of bolt in plate and f_u is ultimate strength of bolt [35,36-38].
(iii) Bolt in bearing

$$F_{t,Rd} = \frac{k_1 \ \alpha_b f_u \ dt}{\gamma_{M2}} \tag{40}$$

Where α_b is the smallest of α_d , $\frac{f_{ub}}{f_u}$ or 1.0, d is the diameter of bolt ,t = threaded height of bolt In the direction of load transfer, for end bolts, $\alpha_d = \frac{e_1}{3d_o}$, $\alpha_d = \frac{P_1}{3d_o} - \frac{1}{4}$ for inner bolts Perpendicular to the direction of load transfer, For edges bolts, k_1 is the smallest of $2.8\frac{e_2}{d_o}$ -1.7 or 2.5 For inner bolts, k_1 is the smallest of $1.4\frac{P_2}{d_o}$ -1.7 or 2.5.For one bolt row in single lap joints, the design bearing resistance for each bolt should be limited to: $F_{b,Rd} \leq 1.5 f_u \ dt / \gamma_{M2}$.

4. Results and Discussions

4.1. Results of seismic analysis and design of four storied office novel precast prestressing composite frame

4.1.1. Establishment of the numerical model

The analysis and design was carried out using the above basic design steps and ETAB17 software for model building and internal forces calculation. The 3D model is shown in Figure 14 below. The results are validated with that one of four-storey building office of the developed novel structure constructed in Suzhou, China by ZYF Construction Group Co., Ltd. The novel structure has the floor plan dimensions of 63.6m×20.6m where ground floor height is 5.5m .and typical storey height is 4.2m. Bending moment diagram can be seen on Figure 15. The design parameters are shown in the Table 2, Table 3, and Table 4.

Table 2. Selected Materials properties according to African manner (EC2) and Chinese design system

Material properties	African design system	Chinese design system
Unity weight of masonry	21kN/m³	21kN/m³
Unity weight of reinforced concrete	25kN/m³	25kN/m³
Grade of concrete	C35/C45 or f_{ck} =35	C40
Grade of rebar	B400	HRB 400
Grade of steel	S235, S355	Q235, Q355
Modulus of elasticity of concrete(Ecm)	34,000MPa	32,500MPa
Initial modulus of elasticity ($Ecm(t_o)$)	30,000MPa	-
Modulus of elasticity of steel	210,000 MPa	200,000MPa
Grade of prestressing steel(strand)	1860MPa	1860MPa
Initial characteristic strength of concrete ($f_{ck}(t_o)$)	17.6MPa	26.8MPa
Initial mean tensile strength of concrete($f_{ctm}(t_o)$	2.8MPa	-
Mean tensile strength of concrete (f_{ctm})	3.2MPa	-
Tensile strength of concrete at transfer of prestress($f_{ct,0}$)	$f_{ct,0}=0.5f_{ctm}(t_o)=1.4MPa$	-
Compressive strength of concrete at transfer of prestress($f_{cc,0}$)	$f_{cc,0} = -0.5 f_{ck}(t_o)=-8.8MPa$	-
Tensile strength of concrete after transfer of prestress($f_{ct,t}$)	$f_{ct,t}=0.5 f_{ctm}=1.6MPa$	-
Compressive strength of concrete after transfer of prestress ($f_{cc,t}$)	$f_{cc,t} = -0.5f_{ck} = -17.5MPa$	-

Table 3. Load conditions according to African manner(EC1) and Chinese design system

Load conditions	African design system	Chinese design system
Dead load	Self-weight of structural members	Self-weight of members
Live load for office(minimum)	2kN/m²	2kN/m²
Live load on roof	0.5kN/m²	0.5kN/m²
Plaster on floor	0.4kN/m²	0.4kN/m²
Floor tiles	0.45kN/m²	0.45kN/m²
Gypsum mortar under floor slab	0.36kN/m²	0.36kN/m²
Iron garvanized sheets	0.12kN/m²	0.12kN/m²
Truss	0.3kN/m²	0.3kN/m²
Purlins and system bracing	0.1kN/m²	0.1kN/m²
Gypsum ceiling	0.1kN/m²	0.1kN/m²

Table 4. Earthquake parameters

|	African design system	Chinese design system
Location	Southern Province of Rwanda, Huye City	Suzhou, China
Seismic zone(earthquake level or intensity)	VI with PGA *0.10g*	7 with PGA *0.10g*
Earth quake design group	-	1
Ground type(Site class)	Type C	Site class II
Importance factor	1	-
Time period(Vibration period)T	$T= C_tH^{3/4} C_t = 0.05, H=18.1m T=0.44s$	*0.45s*
Earthquake load direction	*X* and *Y* direction	*X* and *Y* direction
Diaphragm type	Rigid	Rigid
Type of analysis	Linear Static	Linear Static
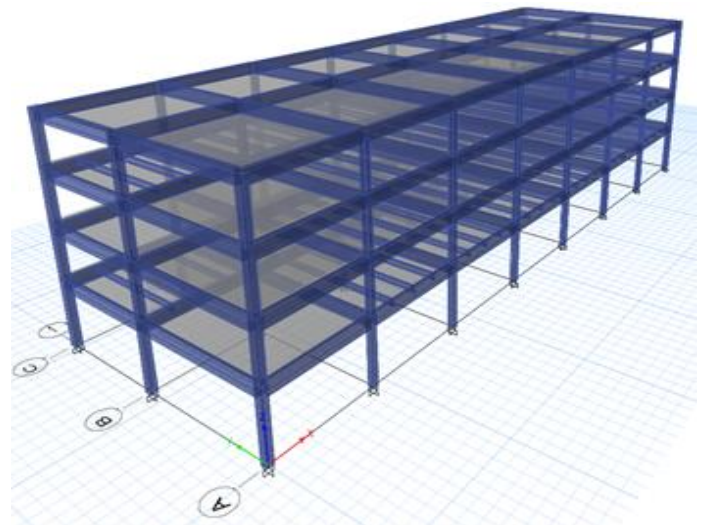
Figure 14. 3D View of the model in ETABS software
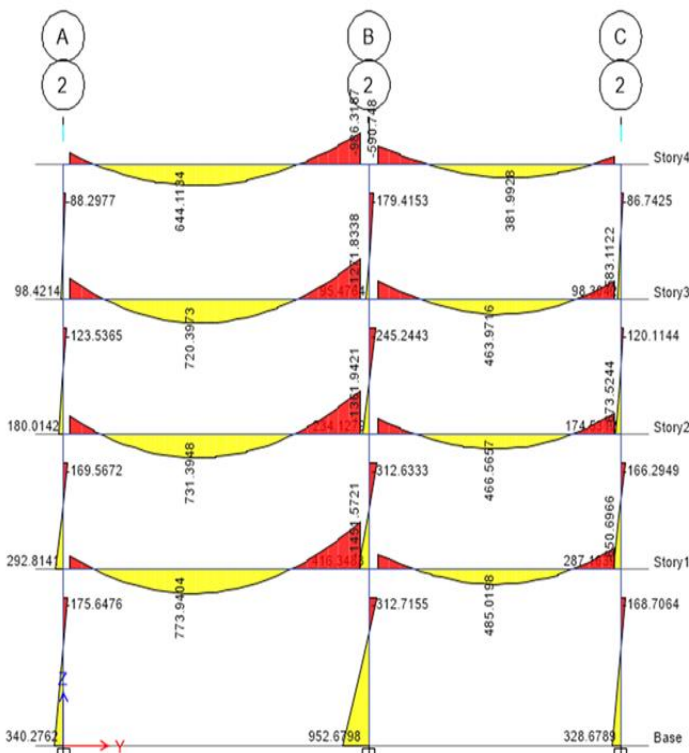
Figure 15. Bending moment diagram

4.1.2. Design results

After the analysis and design using basic design steps and EABS17 software, the following Table 5 shows the detail design results which were validated with that one of four-storey building office of the developed novel structure constructed in Suzhou, China by ZYF Construction Group Co., Ltd.

Table 5 Validation of detail design results

Structural member	African design system	Chinese design system
Precast prestressed slab	160mm thick,80mm in situ casting,5strands 12.7mm each flat duct, overall thickness of composite slab=240mm	140mm thick,100mm in situ casting,3 strands each flat duct, overall thickness of composite slab=240mm
Precast prestressed beam mid-span	h=900mm,b_W=400mm,A_S top=5T25,A_S btm=3T25, 5strands 12.7mm,	h=900mm,b_W=400mm,A_S top=7T20,A_S btm=5T20, 3strands 12.7mm,
End of beam connection with H-steel beam	H700x300x13x24mm	H700x300x12x18mm, H800x300x12x18mm
Concrete filled rectangular steel tube columns	External columns 650X550mm(550x450x20mm) Internal columns 850X750mm(750x650x24mm)	External columns 650x550mm(550x450x16mm) Internal columns 600x500mm(500x400x16mm)
HSB(High Strength Bolt)	M27	M22

According to Table 5, the design results from African design system are greater than that ones in Chinese design system. For instance, the web and flange thickness of H-steel beam section are

greater than that ones in Chinese design system but, the height and width are the same. This means that more steel is used in African design system, and the African design system is more conservative while Chinese design system is more economical. In addition, the safety factor for dead load and live load in African design code is greater than that in Chinese design code.

Regarding design of prestressed members, the African design code use more strands and greater section thickness than the Chinese design code, however the grade of strand is the same.
The ETABS 17 software was employed to assess the seismic loads effects in both African and Chinese design system, and the results are summarized in the tables and figures below.

Table 6. Comparison of the seismic actions

Chinese Design system		African design system		
Storey	$Fi(kN)$	Storey	$Fi(kN)$	%difference
1	512.62	1	529.78	2.673
2	892.79	2	912.24	2.132
3	1279.35	3	1307.37	2.143
4	1309.92	4	1328.37	1.389
			Average	2.1
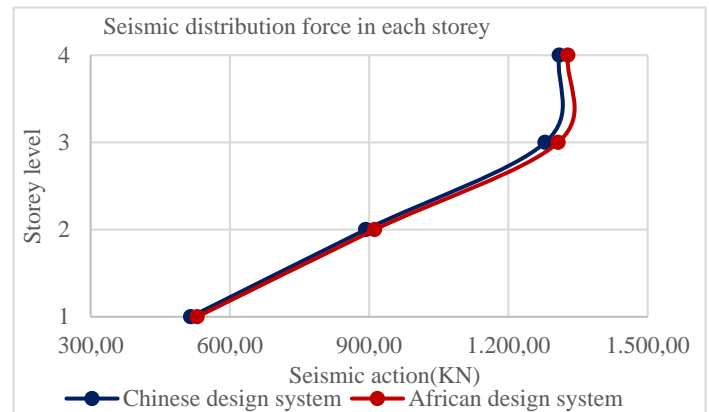
Figure 16. Seismic distribution force in each storey

From analysis done, comparing the seismic base shear or the expected lateral force on the base of the building structure due to seismic loads, it is found that F_{Ek}=4,054.47kN in Chinese design system is less than F_b = 4,077.53kN in African design system. This is due to the fact that the seismic map of Rwanda, where the site is located with earthquake intensity of 6 with PGA 0.10g is close to that one in Chinese system which is 7(0.10g), but have different design spectrum such as $S_d(T_1)$ = 0.0871g for African method and $amax$=0.08 for Chinese method[39,40].

The seismic force in each storey in African design system is greater than that one in Chinese design system by average 2.1%, as indicated in Table 6. Therefore, this indicates that the African design system considers the building structure to resist much applied earthquake forces more than Chinese design system and it is more conservative. Figure 16 shows the curves which indicate the trends of seismic force distribution in each storey. For both design systems, the curves show the increase of seismic force with the height of the building. Therefore, the higher the building is, the greater the earthquake effect is, and in multistorey building design, earthquake effect should be highly considered and especially in high seismic zones, more precaution have to be provided.

Table 7. Max interstorey drift in *X* direction due to earthquake

Chinese Design system		African design system		
Storey	Drift (%)	Storey	Drift (%)	%difference
1	0.0533	1	0.0544	2.0
2	0.0522	2	0.0551	5.3
3	0.0391	3	0.0411	4.9
4	0.0228	4	0.0229	0.4
			Average	3.1
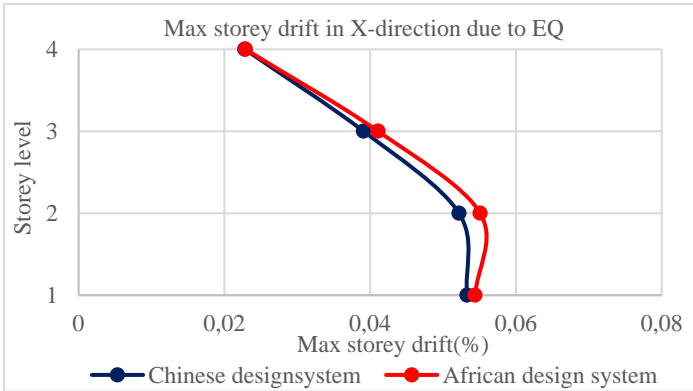
Figure 17. Max interstorey drift in *X*-direction due to earthquake

Table 8. Max interstorey drift in *Y*-direction due to earthquake

Chinese Design system		African design system		
Storey	Drift (%)	Storey	Drift (%)	%difference
1	0.0584	1	0.0608	3.9
2	0.0598	2	0.0626	4.5
3	0.0457	3	0.0468	2.4
4	0.0278	4	0.0285	2.5
			Average	3.3
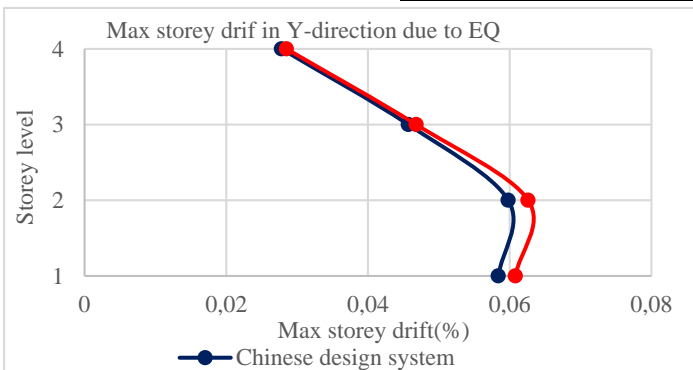
Figure 18. Max interstorey drift in *Y*-direction due to earthquake

Storey drift is the horizontal displacement of the floor relative to the floor below. In Figure 17 and Table 7 above, the max storey drift due to earthquake in *X*-direction under Chinese design system is average 3.1% lower than that in African design system, and in *Y*-direction in Figure 18 and Table 8, the Chinese design system is average 3.3 % lower than that in African design system. This indicates that the Chinese design system takes into account the earthquake loads effect at higher level than it is in African design system. In addition, both design systems are safe since the results of storey drift do not exceed the maximum allowable limits, and the drift ratio (%) in each storey are less than 0.5% ,which indicate that after the earthquake the building is repairable.

5. Conclusions

As Chinese construction companies remain entering Africa continuously to carry out construction projects in different African countries in line with sustainable development, the developed construction method in China are most likely to be applied in the old continent. A novel precast prestressing composite structure, developed by Chinese investigators and constructed by ZYF Company in Suzhou, China, is believed to have a good prospect in Africa. Therefore, this study aimed to design method of the mentioned novel precast structures based on African manners to help Chinese construction companies to design and implement the novel precast structures in Africa. The work and conclusions of this study are as follows:

1. The structural design systems in Africa and China was compared to help designers know the difference between the two design system and develop a better design method for the new precast prestressed composite frame in Africa. The structural design system in Africa is based on Eurocodes, therefore, main Eurocodes were selected for the comparison. The comparison included material properties, loads and load combination, design equations for composite elements. It can be found that the basic theory of the two design system is similar, but the technical design parameters and equations are different, thus, it is necessary to develop a structural method based on African manners for the novel precast structure.

2. The structural design method of the novel precast structure was built with African design system. The basic structural design steps based on the limit state method according to Eurocodes were established, and the seismic design process for the novel precast structure was also developed based on equivalent lateral seismic force method. Some important structural details of the novel frame for earthquakes based on African manner were presented.

3. The developed detailed design method of the novel structure-was applied by designing a four storey novel building structure expected in Huye City at Southern Province of Rwanda, of which the earthquake parameters were close to the ones of Suzhou, China. The design results were validated by comparison with results of the novel four storey building structure constructed in Suzhou, China. The strengths of connection between the H-steel beam to concrete filled rectangular steel tube and between H-steel beam and precast concrete portion, were verified using the recommended formula from the previous experimental investigation [11] and fulfilled the conditions and requirements.

Considering earthquake loads in design, the max interstorey drift ratio is 0.0626% in African design system and 0.0598% in Chinese design system. The interstorey drift in the Chinese design system, is on average 3.3% lower than that in African design system. The main difference of the determined structural details is that structural H-steel beam profile section found in African manners have greater web and flange thickness than that in Chinese design system. The size of concrete filled rectangular steel tube used in African design system is greater than that one used in Chinese design system. Hence, it is shown that both design systems provide safe design since all the results are within allowable limit,

and the Chinese design method is more economical but the African design method is more conservative.

Acknowledgment

Conflict of Interest Statement

The author declares that there is no conflicts of interest concerning this article.

References

1. Lucy Corkin. (2011).Chinese Construction Companies in Angola: A Local Linkages Perspective.MMCP Discussion Paper No 2, University of Cape Town and Open University, ISBN: 978-1-77011-233-9.

2. Ian Taylor and Tim Zajontz. (2020). In a fix: Africa's place in the Belt and Road Initiative and the reproduction of dependency. South African Journal of International Affairs, VOL.27, NO.3,277–295. https://doi.org/10.1080/10220461.2020.1830165

3. Chuan Chen. (2007). An empirical analysis of Chinese construction firms' entry into Africa. The CRIOCM2007 International Symposium on Advancement of Construction Management and Real Estate 8-13, Sydney Australia.

4. Christopher Burke. (2007). China's Entry into Construction Industries in Africa: Tanzania and Zambia as Case Studies. CHINA REPORT 43 : 3 :323–336 SAGE Publications Los Angeles/London/NewDelhi/SingaporeDOI: 10.1177/000944550704300304

5. Tim Zajontz. (2020). The Chinese infrastructural fix in Africa: Lessons from the Sino-Zambian 'road bonanza'. Oxford Development Studies, DOI:10.1080/13600818.2020.1861230

6. Chuan Chen and Ryan J.Orr.(2009). Chinese contractors in Africa: home Government support, coordination mechanisms, and market entry strategies. Journal of construction engineering and management, 135(11):1201-1210.

7. Chuan CHEN et al, local operations of Chinese construction firms in Africa: an empirical survey [J]. The International Journal of Construction Management (2009) 75 – 89

8. Bungale.S. Taranath, ph.D, P.E, S.E. (2017). Tall building design, steel, concrete, and composite system.

9. Rui Li.(2016). Seismic properties of joints composed of CFST columns RBS composite beams, PhD thesis. Australia, Institute of infrastructure Engineering Kingswood Campus Penrith NSW Australia Western Sydney University.

10. EN1994-1-1-Eurocode4. (2004).Design of composite steel and concrete structures part1.1General rules and rules for buildings.

11. Shuaike,F.,Donghzi,G.,Zhengxing,G,,Zhongxiang,L.,Guojian,L., Changyi,G.(2021). Seismic performance of assembly joints between HSPC Beams and concrete-encased CFST Columns. Journal of Construction steel Research 180,106572 P.1-14.

12. Zhang, X., Zhang, S., Niu, S. (2018). Experimental studies on seismic behavior of precast hybrid steel–concrete beam. Advances in Structural Engineering, 00(0): 1–17.

13. Shuaike, F., Donghzi, G., Luyao, N., Yu, L., Zhongxiang, L., Zhengxing, G. (2022). Experimental study on seismic behavior of joints connecting precast H-steel reinforced concrete beams and concrete-filled steel tube columns.Journal of building engineering 4,103444 P.1-15.

14. Li, B., Kulkarni, S., Leong, C. (2009). Seismic performance of precast hybrid-steel concrete connections. Journal of Earthquake Engineering, 13(5): 667-89.

15. MIDIMAR (2015). The National Risk Atlas of Rwanda.

16. Erochko, J., Christopoulos, C., Tremblay.R, Choi, H. (2011). Residual drift response of SMRFs and BRB frames in steel buildings designed according to ASCE 7-05. Journal of Structural Engineering (ASCE), 137(5): 589-99.

17. R.P.Johnson. (2004). Composite structures of steel and concrete.

18. R.Narayanan. (2005). Steel-concrete composite structures stability and strength.

19. Anamika Tedia and Dr. Savita Maru. (2014). Cost, Analysis and Design of Steel-Concrete Composite Structure Rcc Structure". IOSR Journal of Mechanical and Civil Engineering (IOSR-JMCE) e-ISSN: 2278-1684, p-ISSN: 2320-334X, Volume 11, Issue 1 Ver. II, PP 54-59.

20. Jianguo NIE.,Jiaji WANG.,Shuangke GOU.,Yaoyu ZHU.,Jiansheng FAN.(2019). Technological development and engineering applications of novel steel-concrete composite structures. Front. Struct. Civ. Eng., 13(1): 1–14 https://doi.org/10.1007/s11709-019-0514-x

21. Alessandro, Z., Michele, B., Joel, P.Conte, M.ASCE. (2008). Nonlinear seismic response analysis of steel-concrete composite frames.Journal of structural engineering, P.986-997.

22. Enrico Spacone, A.M.ASCE., Sherif EI-Tawil, M.ASCE. (2004).Nonlinear analysis of steel-concrete composite structures: State of the arts.Journal of structural engineering Vol.130, No.2, P.159-168.

23. Raymond, I.G., Neil Colin M., Gianluca R. (2017).Design of prestressed concrete to Eurocode2, second edition.

24. Yang K, Oh M, Kim M. (2010). Flexural behavior of hybrid precast concrete beams with H-steel beams at both ends. Engineering Structures, 32(9): 2940-49.

25. Yang K, Seo E, Hong S. (2016). Cyclic flexural tests of hybrid steel-precast concrete beams with simple connection elements. Engineering Structures, 118: 344-56.

26. Kim S.Elliot. (2017). Precast concrete structures second edition.

27. GB50009-2001. (2002). Load code for the design of building structures, Ministry of construction of the People's Republic of China, Beijing.

28. GB50017-2003. (2003). Code for design of steel structures, Ministry of construction of the People's Republic of China, Beijing.

29. Yida Guo., Guobin Gong., Chee Chin., Cheng Zhang. (2018). Structural design of concrete to EC2 and GB50010-2010: a Comparison. MATEC Web of Conference, 175, 01039, pp.1-851.

30. JGJ138-2016. (2016).Code for design of composite structures, Ministry of housing and Urban-Rural development of the People's Republic of China, Beijing.

31. EN1992-1-1-Eurocode2. (2004). Design of concrete structures part1-1, general rules and rules for buildings.

32. BSI, Steel, concrete and composite bridges BS5400: Part 5. (1979).Code of practice for design of composite bridges.

33. EN1993-1-8-Eurocode3. (2003). Design of steel structures part1-8, design of joints.

34. EN1993-1-1-Eurocode3. (2003).Design of steel structures part1-1, general rules and rules for building.

35. EN1991-1-Eurocode1. (2001).Actions on structurespart-1-1, general actions, densities, selfweight, imposed loads for building.

36. EN1990-1-Eurocode0. (2001). Basic of structural design.

37. W.H.Mosley, R.Hulse, J.H.Bungey. (2012).Reinforced concrete design: to Eurocode 2.

38. BSI, Structural use of concrete. Part I:(1997) Code of practice for design and construction.

39. GB50011-2010. (2014). Code for seismic design of buildings, China Architecture and Building Press, Beijing.

40. EN1998-1, Eurocode8. (2003). Design of structures for earthquake resisntantce-Part1: General rules, seismic actions and rules for builings.

ENGINEERING PERSPECTIVE
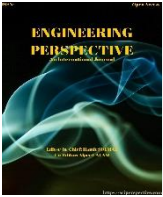
Assessing Mechanical Properties of Free-Fall Self-Compacting Concrete and its Application in Concrete-Filled Steel Tube Columns

Jean de Dieu Ninteretse[1*] [iD], Marc Nshimiyimana[2*] [iD], Jovial Niyogisubizo[3] [iD], Jean Claude Sugira[4] [iD]
Alain Niyongabo[5] [iD]

[1]*Department of Construction and Real Estate, School of Civil Engineering /Southeast University, Nanjing,210096, China*
[2]*School of Civil Engineering / Southeast University, Nanjing,210096, China*
[3]*Shenzhen Key Laboratory of Intelligent Bioinformatics and Center for High-Performance Computing, Shenzhen Institute of Advanced Technology, Chinese Academy of Sciences, Shenzhen 518055, China*
[4]*School of Transportation Engineering of Southeast University, Nanjing, China*
[5]*College of Hydrology and water resources, 1 xikang Road,Nanjing, 210098, China*

ABSTRACT

The application of Self-Compacting Concrete (SCC) in the construction industry has been adopted over the years and its quality over normal concrete has been influential. The high-rise construction demands emphasize the necessity of concrete pumping technology due to limited working space. Concrete made from manufactured sand was produced and the variation of free fall height based on the experiment of SCC was studied. This study assesses both the mechanical properties of SCC cast after free fall from various heights and its applications in the CFST columns. The study specifically focuses on a varied height of free fall at 6m, 6.5m, 7m, 7.5m, and 8m. The workability performance of this SCC, batched from manufactured sand has been evaluated, and slump extension between 500-600 mm was obtained. The concrete cubes and prism specimens were tested for compressive and splitting, therefore the associate strength was obtained. Testing both normal and SCC reveals unfavourable effects in strength reduction with an increase in free fall height. At the final height of 8m, an observed decrease in strength of about 15%-20% using SCC was observed. At 6.5m, there is a 3% decrease in strength, and the reduction in cube-splitting strength ranges from 7% to 11% with SCC from natural sand. When the free fall height is 7m, the cubic compressive strength is reduced by about 4.3-5.4%, and its cube-splitting strength at a height of 7m decreases by approximately 7–11%. Despite the gradual decrease noted in this study, the application of SCC obtained at 7m in CFST has demonstrated reliable results in terms of combined strength, suggesting its use in columns not exceeding the same height.

Keywords: SCC, CFST, Free fall height, manufactured sand, compressive strength

1. Introduction

Over the years, with the rapid development of concrete materials, the application of high-performance concretes with excellent properties has been widely adopted. SCC is one of the concretes with incomparable excellent working performance about other concretes. In the early 1980s, the Japanese research team prepared SCC with ordinary concrete materials for the first time and named it solid concrete [1, 2]. Since then, more and more researchers have begun to develop and widely use SCC in the construction of skyscrapers and modern houses.

SCC has been described as the most revolutionary development in concrete construction for several decades. It has continuously been adopted in the construction industry due to its added properties over ordinary concrete. The increase in use lies in the structural limitations of normal concrete considered as low resistance to tensile loading, cracking, vibration, density, strength development, final strength, and durability. SCC has been proven to have the best quality control thus flowing like honey, its ability to flow into a confined space is the added value when combined with steel reinforcements. The scenario that SCC can be manufactured in a site batching plant

or a ready-mix concrete plant, and delivered to the site by truck can lead to the concrete free fall method especially when the working space is limited. Due to its self-vibration, SCC will have a stronger strength than standard vibrated concrete with a similar water-to-cement ratio. Then, this led it to be placed either by pumping or pouring into horizontal or vertical structures, some literature suggests, SCC can be poured above 5 m in height without any sort of segregation using a well-built SCC. On the other hand, some studies limit the standard maximum free drop height and maximum lateral flow distance should be around 5 m or less and 8 to l5 m or less, respectively s per EFNARC 2002 guidelines.

Currently, the use of SCC has gained popularity for its fluidity and anti-segregation properties thus being preferable in CFST columns. However, during high falls, before SCC is cast in designated columns can segregate, affecting its mechanical properties. The mix proportions in this case are critical, impacting compaction and CFST performance. The paste volume and aggregate ratios also affect the post-peak behaviour and ductility of these tubes. SCC's use in vertical structural members, like densely reinforced wall columns and nodal core areas, has been assured to cause segregation due to throwing out. The issues like displacement of reinforcements or damage of formwork, adhere to the construction codes and practices during concrete pouring, especially when allowing concrete to fall freely [3, 4]. Factors such as concrete ingredients, mixing, proportion, application method, and free fall height influence concrete compactness in the steel tubes. Empty spaces in steel tube may form thus, reducing its ability to confine the concrete core, thereby decreasing the load-carrying capacity and ductility of the structure [5, 6]. BS81101:1997 mandates precautions to prevent displacement of reinforcement, ducts, formwork, and damage to formwork faces during free falling of concrete, emphasizing the need for a cohesive, non-segregating mix while ACI standards do not specify a maximum free-falling height for concrete, the "Technical Regulations for the Application of SCC" limit pouring heights in reinforced column wall formwork to 5 m, extending to 9 m with the use of auxiliary devices like chutes and tandem tubes.

This study highlights the adaptability of free-fall SCC in hollow steel tube technology. Hou et al. [7] emphasized the significance of the construction stage in quality management for CFST members by highlighting the impact of construction methods on void formation, particularly during the prevalent pumping method. The method, commonly used, presents challenges as the air density within the steel tube rises with concrete height during pumping, risking voids if not promptly discharged. Despite the use of micro expansion agents, the shrinkage of high-strength core concrete may lead to voids between steel tubes and concrete over time, attributed to shrinkage and creep. Cao et al. [8] conducted a model test and theoretical analysis on core concrete filling in a CFST project. They found that the degree of void significantly affects the ultimate bearing capacity of such tubular members, more severe void reduces the bearing capacity. Chen et al. [9] analysed the axial compression process of hollow CFST and established the relationship between hollow degree and axial force. The void space in the tube increases initially with axial load, but beyond a critical value, it decreases with further axial load increase. Tests conducted by Zheng et al. [10], and Kumari et al. [11] revealed that the bearing capacity of CFST members with voids is lower than that of those without voids. The study

found that insufficiently dense core concrete pouring can impact the coordinated stress between the steel tube and concrete, leading to a reduction in the bearing capacity of CFST members.

The steel tube and the infilled concrete work together to resist the applied external load, which is a fundamental assumption in the use of CFST columns. The factors affecting the compactness of concrete in steel tubes include concrete components, mixing, proportion, application method, and height of fall. Voids between the concrete core and outer steel tube can decrease confinement, reducing load capacity and utility. SCC is commonly used in CFST structures, but the compaction level within the steel tube is rarely studied. This study uses the common techniques for checking the quality of SCC in confined spaces like the percussion–acoustic method, well-known for its cost-effectiveness and high efficiency in detecting voids within concrete exposed to air. This method has been adapted for identifying voids in underwater concrete, considering the fluid-structure coupling effect. The Impact Rebound Method serves to indicate surface hardness, exhibiting correlation with concrete compressive strength. Additionally, the Vibration Test Method involves applying shock vibrations to prismatic specimens by hammering one end in the longitudinal direction. This method consolidates concrete in two stages: firstly, by displacing concrete particles and secondly, by eliminating trapped air (For Construction).

Shortage of working space mainly on small construction sites is likely and some methods of concrete casting can be adopted. This study is based on the experimental investigation of pouring concrete from heights, assessing the possible mechanical properties: compressive and tensile strength, and workability which is important in vibration and pouring to avoid segregation. This study aims to investigate the free fall properties of SCC made from artificial /manufactured sand. It applies artificial sand to demonstrate SCC's reliability in CFST columns within specified steel design sections. The free fall heights were varied at concrete batches from heights: 6m, 6.5m, 7m, 7.5m, and 8m based on the conflicts of existing literature. Additionally, the results from the best-performance batch were adopted into CFST for dual purposes: achieving the properties of hardened SCC and combined strength through its application. Finally, the use of percussion, Impact rebound, and Vibration testing were employed to ensure the distribution and quality of adopted SCC.

2. Materials and Methods

2.1 Materials

This study acknowledges the suitability of natural and man-made (manufactured) sand in concrete. These enhance binding with cement thus boosting strength and durability. Cement interacts with fine sands and various-sized gravels, enabling adaptable concrete mixes. Fly ash and mineral powder refine properties, contributing to workability and long-term strength. These materials enhance specific properties and reduce water content without affecting workability. Hallow steel tube columns filled with SCC mixes offer a unique blend of strength and lightness for high-rise buildings and large-span structures.

For this study, SCC and CFST were designed and tested to ensure the feasibility and extensive application in practice. The manufactured sand obtained from crushed gravel was used to make the quantity of SCC. The concrete, truck mixer has been used for mixing large volume quantity and quality concrete needed in the experiment.

Additionally, the SCC was tested using both cubes and prism formworks. The results from slump, compressive strength, and splitting strength tests were obtained. The hallow steel tube sections of square, rectangular, and circular shapes were employed, and used in application thus defining the purpose of this study.

2.2. Methods

2.2.1. Experimental Design

The experiment was conducted using artificial sand to make a C40 standard SCC; corresponding working performance (slump extension 500-600 mm) was taken as parameters to discuss the influence of manufactured sand on the working performance under a high drop of SCC. According to Table 1, SCC prepared using machine-made sand generally performs worse than natural sand. The main reason is that the fineness modulus of machine-made sand is small, usually only about 1.0, and the content of lime powder is large, which also reduces the cohesion of fresh concrete.

Table 1. Mix ratio of SCC with artificial sand

Number	cement	Artificial sand	Fine sand	5-10 gravel	10-16 gravel	10-20 gravel	fly ash	Mineral powder	admixtures	Bulking agent	water	water reducer	slump spread
I	294	660	219	88	442	355	63	63	8.32	42	165	1.8%	570
II	294	660	219	88	442	355	63	63	7.85	42	165	1.8%	600
III	294	917	-	85	443	339	63	63	8.32	42	165	1.8%	580
V	284	908	-	82	415	332	63	63	8.81	42	165	1.8%	570
IV	294	765	135	86	432	346	63	63	8.32	42	165	1.8%	500

From the observed SCC performance from the initial slump extension of 690mm, at T500 (time in seconds taken by the concrete to reach a spread diameter of 500mm after the cone is lifted) [12, 13] was 1.5s, 1.5 hours later, the slump of 630mm, at T500 was 2.25s, it indicated a significant loss of about 60mm; The initial falling time of the slump cylinder was 2.2s, and about 2.89s after 1.5 hours. There was no bleeding phenomenon around the collapse extension and inversion test of concrete.

In this comprehensive study, a thorough examination was conducted on a total of 48 CFST columns to provide a detailed analysis of their structural behaviour. Among these columns, 10 were designed with a circular cross-section, while the remaining 38 featured a rectangular configuration. It is noted that the steel tubes used in this research were fabricated from Q355B steel, known for its high strength and durability. The selection of Q355B steel ensures that the CFST columns exhibit robust mechanical properties, contributing significantly to overall structural integrity [14, 15]. The internal cavities of these steel tubes were uniformly filled with high-performance C40 concrete, further augmenting the columns' load-bearing capacity and overall performance. This incorporation of Q355B steel and C40 concrete not only aligns with contemporary construction standards but also represents a deliberate choice to achieve optimal strength and stability in the tested CFST columns as detailed in Table 2 and Figure 1.

It is therefore proven that in the construction of CFST columns with dense diaphragms, various methods can be employed. The utilization of the pipe jacking method for high or large one-time pouring heights, and achieving the required jacking pressure can be challenging. Alternatively, a method similar to underwater concrete tube pouring requires a special vibrator and complex safety measures when operating at high altitudes. However, the SCC tube method poured directly from the top of the column, utilizes the fluidity of SCC to eliminate the need for vibration. During the pouring process, a gap (free fall) is maintained between the duct end and the concrete surface.

Table 2. Information table of steel tube columns

Component member	Section size(mm)	Root number	Concrete strength class
GKZ 1	□1500*1000*40	16	C40
GKZ 2	□1600*1600*40	2	C40
GKZ3a	□1000*1000*40	6	C40
GKZ3b	□1000*1000*30	6	C40
GKZ4	□800*800*35	14	C40
GKZ5	□700*500*20	10	C40
GKZ6	□800*500*24	4	C40
GKZ7	○1000*30	10	C40

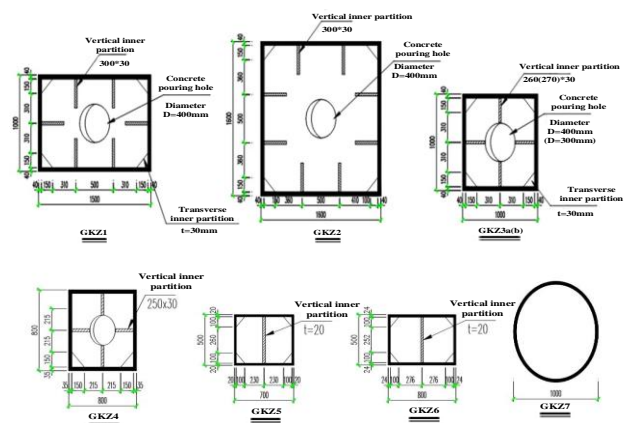Note: □ represents rectangular/square steel columns, ○represents circular steel columns

Figure 1. Detailed drawing of column section size

2.2.2. Experimental Methodology

The height from concrete drop was set to 6m, 6.5m, 7m, 7.5m and 8m, the mixture was set to unique and the variation in the properties based on height of drop were noted. The concrete truck was set to

fixed station and the conduit was varied based on free-fall heights respectively. The purpose of undertaking these heights refer to the uncertain and challenges of different construction site conditions where accessing the concreting points is very complicated thus delaying the project and increase cost uncertainties. The difference in the five batches lies in the height of pump truck conduit, the results associated with the tests procedures were provided under slump test using slump cone, compressive strength tests using cube mould, and splitting tests using prism mould.

During the concreting process from concrete pump truck to ground base, it was required to pour 20mm of cement mortar with the same proportion, to prevent the rebound of the concrete falling process. A layer of soil was underlaid, rain canvas was laid on it, and concrete was freely dropped from different heights by placing booms, and then casted into the cube and prismatic test moulds. Even though the site was soft, there was a significance rebound phenomenon and the most obvious falling distance was 8m. According to the field observations, the rebound height was approximately 0.3 m horizontally. The field observation indicates that although there is a rebound, there is no great segregation.

2.2.2.1. Quality Detection Methods

Flowing of SCC in conduit results in minimum loss of strength depending on the quality of concrete produced, however, it is important to consider the concrete flow through conduit over height. The purpose of varying the heights of conduit from 6m to 8m explains the different strength obtained though seemed to have no practical restrictions when combined with steel. Concrete was applied in CFST columns of previously specified sizes and shapes which resulted in a very beautiful columns with less voids. The applications were adopted according to the code of practices regarding the uses of SCC in CFST with great care and the sound results were obtained. This section explains the 3 methods used for checking the hardened properties and qualities of casted CFST columns.

2.2.2.2. Percussion method

The incorporation of percussion method in CFST columns serves the purpose of ensuring optimal compaction and consolidation of the concrete. This technique employs percussion or vibration methods throughout the construction process to eliminate air voids, improve the bond between steel and concrete, and achieve a uniform density across the entire column [16, 17]. To assess the concrete's density within the column tube, a sound-based analysis was employed, utilizing a specialized Number 3 steel hammer designed specifically for quality inspections. The inspection process involves comprehensive percussion testing on each steel tube column. These inspections occurred at both 7 and 28 days, ensuring a thorough and accurate evaluation of concrete density within the columns. This method entails tapping at several equidistant points along the column's periphery, moving from the bottom to the top. Given that the two ends of the CFST column are fixed, there is a disparity in amplitude between them, resulting in inconsistent knocking sounds between the middle and the two ends of the column. Any deviation from the expected sounds, including the identification of a third kind of sound, is considered abnormal during this assessment.

2.2.2.3. Impact rebound method

The rebound hammer is a non-destructive testing apparatus, whereby the rebound of the spring-driven mass is measured after its impact with the concrete surface. The output of the rebound hammer is referred to as the rebound number and is correlated with the surface hardness of concrete [18]. When hammering the surface of the concrete structure, vibration will be induced on the surface. The elastic wave signal is continuously excited along the test concrete surface. By extracting the reflected signal and processing the corresponding image, the internal defects of the structure can be identified. In general, the following changes in vibration characteristics occur at the part where stripping occurs as shown in Figure 2:

(1) The bending stiffness decreases significantly, and the transcendence cycle increases;

(2) The escape of elastic wave energy becomes slow, and the duration of vibration becomes longer;
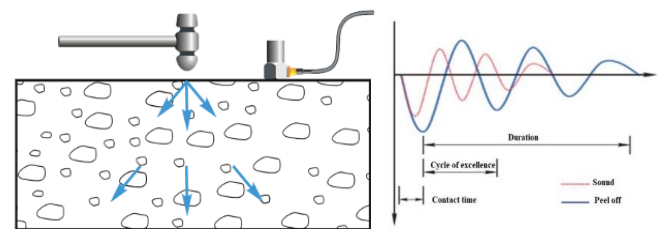

Figure 2. Variation characteristics of vibration parameters during peeling/emptying

When the structure is empty, the indexes (excellent period, duration) all tend to increase. Due to the lack of an absolute threshold, the induced vibration method involves many parameters, such as duration, predominance period, etc. To normalize relevant parameters, a void index can be introduced.

2.2.2.4. Vibration test method

The vibration test method in CFST construction aims to optimize mechanical properties by ensuring thorough compaction, uniform density, and void elimination within the concrete fill [19, 20]. This method enhances the material's strength and load-bearing capacity by eliminating air voids, promoting homogeneous distribution, and improving bonding between the steel tube and concrete. By focusing on compaction and uniformity, the vibration test method enhances the structural integrity and reliability of CFST columns, ensuring they meet standards while effectively supporting various loads and stresses within diverse structural applications. The signal acquisition system is selected, the appropriate acquisition parameters are set, the CFST structure is tested several times, and multiple acceleration response signals of the CFST under transient excitation are obtained.

3. Results and Discussions

This section details the results obtained from compressive and splitting tests performed using manufactured sand, demonstrating

the influence of the studied free fall heights on the mechanical properties of SCC. It presents the results from 144 specimens – 54 for compressive strength and 54 for splitting strength of both normal concrete and SCC with cube moulds, while also presenting 36 specimens for both normal concrete and SCC with prism specimen.

3.1. Cube compressive test results

Table 3 shows the specimen numbers and cube compressive strength with the free-falling height of SCC as parameters. SCC stands for Self-Compacting Concrete, and NC stands for ordinary concrete. The second numbers, 0 and 1, represent the concrete at the test site to start the test. 0 represents the concrete to the site immediately used to start the test, and 1 represents the concrete to the site after waiting for 1 hour to start the test. On the other hand, 0, 6, 6.5, 7, 7.5, and 8 represent free-fall heights in m. For example, SCC-0-6 represents the test study of a 6m free fall from SCC to the site immediately.

Table 3. Cube compressive strength of each specimen

Specimen number	Concrete type	Time/h	Freefall height/m/m	Cubic specimen strength fcu /MPa			Efficient Value	Comparison with original
				Specimen1	Specimen2	Specimen3		
SCC-0-0	SCC	0	0	61	66	61	63	1.00
SCC-0-6	SCC	0	6	63	61	61	62	0.98
SCC-0-6.5	SCC	0	6.5	60	66	59	61	0.97
SCC-0-7	SCC	0	7	58	60	58	59	0.94
SCC-0-7.5	SCC	0	7.5	58	57	58	57	0.90
SCC-0-8	SCC	0	8	54	55	55	55	0.87
SCC-1-0	SCC	1	0	61	64	62	62	1.00
SCC-1-6	SCC	1	6	65	65	66	65	1.05
SCC-1-6.5	SCC	1	6.5	59	60	62	61	0.98
SCC-1-7	SCC	1	7	58	59	58	58	0.94
SCC-1-7.5	SCC	1	7.5	53	53	54	54	0.87
SCC-1-8	SCC	1	8	55	40	60	52	0.84
NC-0-0	NC	0	0	61	62	59	61	1.00
NC-0-6	NC	0	6	59	57	56	57	0.93
NC -0-6.5	NC	0	6.5	56	55	55	55	0.90
NC -0-7	NC	0	7	53	53	50	52	0.85
NC -0-7.5	NC	0	7.5	47	51	50	49	0.80
NC -0-8	NC	0	8	47	45	47	46	0.75

3.2 Cube-splitting test results

The corresponding cube-splitting strength of each test specimen in the first batch is shown in Table 4. Splitting strength is calculated according to Eq. (1):

$$f_{sp} = \frac{2F}{\pi A} = \frac{0.637F}{A} \tag{1}$$

In the Equation: f_{sp} is the splitting strength, F is the ultimate load, and A is the cross-sectional area of the cube.

Table 3. Splitting tensile strength of cubic concrete

Specimen number	Concrete type	Time/h	Freefall height/m	Splitting tensile strength of cube specimen f_{sp}			Efficient	Comparison with original λh-cu
				Specimen1	Specimen2	Specimen3		
SCC-0-0	SCC	0	0	4.28	4.69	4.27	4.41	1.00
SCC-0-6	SCC	0	6	4.73	4.29	4.13	4.38	0.99
SCC-0-6.5	SCC	0	6.5	4.05	4.22	4.41	4.23	0.96
SCC-0-7	SCC	0	7	4.13	4.30	3.93	4.12	0.93
SCC-0-7.5	SCC	0	7.5	4.08	3.90	4.06	4.02	0.91
SCC-0-8	SCC	0	8	3.76	3.76	3.96	3.83	0.87
SCC-1-0	SCC	1	0	4.55	4.20	4.03	4.26	1.00
SCC-1-6	SCC	1	6	4.49	4.21	3.55	4.08	0.96
SCC-1-6.5	SCC	1	6.5	3.44	3.96	4.16	3.85	0.90
SCC-1-7	SCC	1	7	3.74	3.88	3.58	3.73	0.88
SCC-1-7.5	SCC	1	7.5	3.63	3.71	3.56	3.63	0.85
SCC-1-8	SCC	1	8	3.47	3.71	3.41	3.53	0.83
NC-0-0	NC	0	0	4.12	3.79	4.27	4.06	1.00
NC-0-6	NC	0	6	4.11	3.55	3.84	3.83	0.94
NC -0-6.5	NC	0	6.5	3.97	3.84	3.41	3.74	0.92
NC -0-7	NC	0	7	3.87	3.46	3.32	3.55	0.87
NC -0-7.5	NC	0	7.5	3.57	3.30	3.27	3.38	0.83
NC -0-8	NC	0	8	2.99	3.42	3.21	3.21	0.79

3.3 Test results of stress-strain curves of prisms under axial compression

This section focuses on the laboratory experimental phenomenon. Figure 3 shows the typical failure pattern of prismatic specimens under axial compression. It can be seen from the figure that the failure pattern of prismatic specimens under axial compression is generally similar to that of ordinary concrete. Still, the specimens with higher drop height have a more severe shedding phenomenon during failure, and the phenomenon of two inverted cones is evident.

The stress-strain curves of the prisms in each group are presented in Table 5 and plotted in Figure 4 and Figure 5. The stress-strain curves shown in the Figures illustrate the characteristic phases observed in the behaviour of each prism specimen. These curves typically exhibit distinct segments, including the elastic section, where the material undergoes reversible deformation; the splitting section, where the onset of failure or fracture is evident; the descending section, indicating the material's post-peak deformation; and finally, the residual section, representing the residual strength or stability after the peak stress has been reached

(a) 0m   (b) 6m   (c) 6.5m

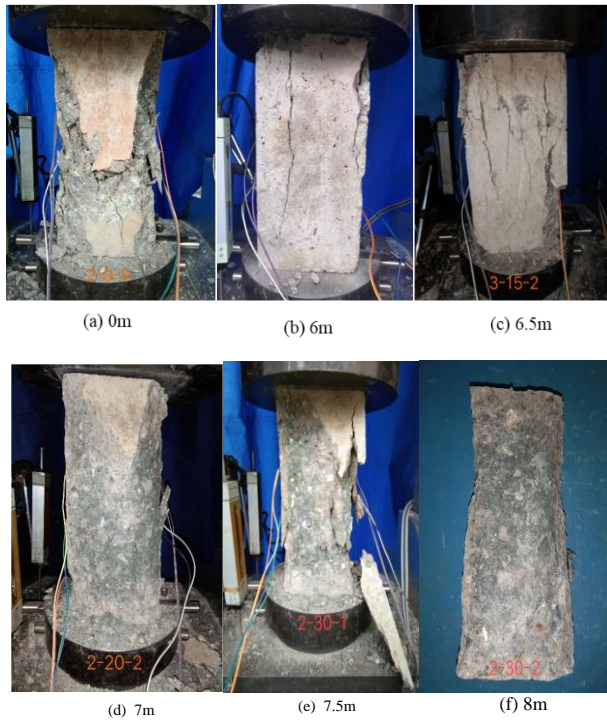(d) 7m   (e) 7.5m   (f) 8m

Figure 3. Failure modes of prisms under axial compression

3.4 Influence of free fall height on various mechanical properties

This section details the results of the relationship between compressive and splitting strengths based on the equations developed by the American Concrete Institute (ACI) in 1999, as have been modified by many scholars [21, 22].   To examine influencing factors such as free-falling height, time-loss, and slump extension of SCC corresponding strength reduction coefficients defined as λ. The specific algorithms are outlined in Eq. (2), Eq. (3), and Eq. (4) respectively.

$$\lambda_{h-cu} = \frac{f_{cu,h}}{f_{cu,0}} \tag{2}$$

$$\lambda_{h-sv} = \frac{f_{sp,h}}{f_{sp,0}} \tag{3}$$
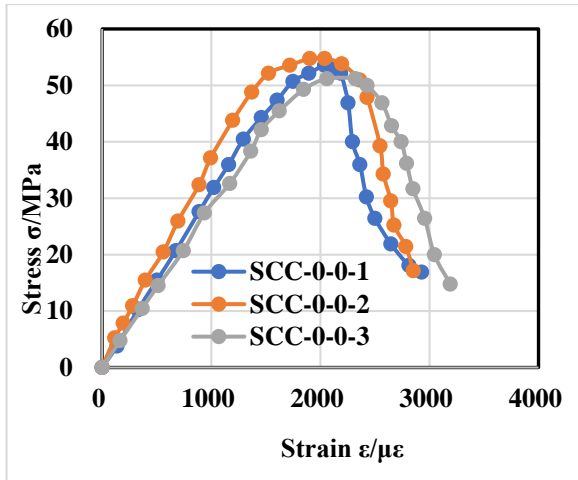
$$\lambda_{h-c} = \frac{f_{c,h}}{f_{c,0}} \tag{4}$$

Where, λ_{h-cu}, λ_{h-sp}, λ_{h-c} represent reduction strengths of compressive, and splitting strengths for cube and prism specimens, respectively due to free fall height.

As the height increases, the cube's compressive and splitting strengths, as well as prismatic compressive strength, generally exhibit a downward trend. Figure 6 illustrates the decrease in the compressive strength of the cube with an increase in height. However, when compared with ordinary concrete, SCC shows a smaller decline range. In Figure 6 (b), as the height of free fall increases from 0 to 6.5m, the compressive strength of SCC only decreases by about 3%. Nevertheless, with further height increase, a gradual decrease is
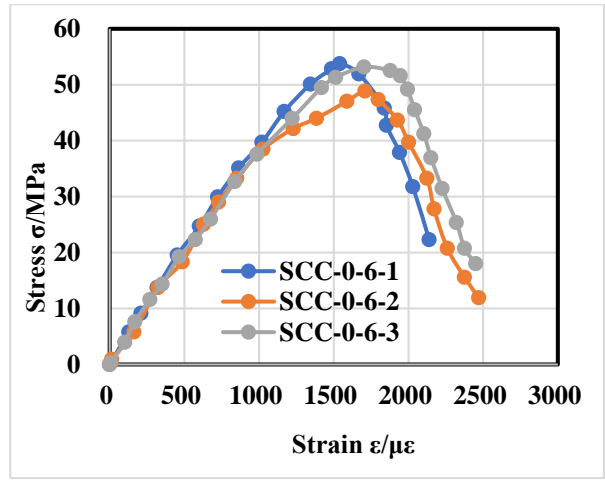
observed, reaching approximately 15% when the height reaches 8m. In contrast, the height increases in ordinary concrete from 0 to 8m resulting in a decline range of about 25%. The observed characteristics of SCC are primarily attributed to its high cement content, leading to a thicker water-cement slurry during the falling process. This, coupled with the substantial compressive strength of coarse aggregates, sets SCC apart from ordinary concrete, which typically has a slump of up to 180 mm. The increased use of powder admixtures in SCC results in a denser cement paste with weaker adhesion, causing a higher likelihood of separation between coarse aggregates and cement paste during movement. Figure 6 illustrates that, under the same free-fall height, the strength of a specimen subjected to a 1-hour delay before testing shows a similar decline as those tested immediately. This suggests that a delay of 1 hour has a minimal effect on the concrete's strength.

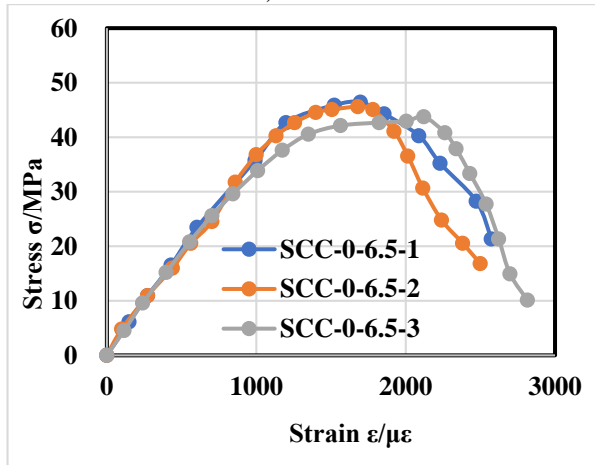Table 5. Typical characteristic values of various prismatic specimens

Specimen number	Prism strength		Peak strain		
	fc / MPa	λ_{h-c}	εcu /με		λ_{h-c}
SCC-0-0	53.6		2040		
	54.8	53.2	1	2040	2046	1.0
	51.2		2060		
SCC-0-6	53.8		1540		
	48.9	51.9	0.98	1709	1650	0.81
	53.1		1702		
SCC-0-6.5	52.9		1697		
	52.0	51.6	0.97	1681	1833	0.90
	49.9		2121		
SCC-0-7	54.4		1987		
	44.8	49.2	0.92	1734	1850	0.90
	48.3		1829		
SCC-0-7.5	44.7		1752		
	45.0	46.7	0.87	1729	1794	0.88
	50.5		1902		
SCC-0-8	43.3		1579		
	43.0	42.2	0.79	1832	1674	0.82
	40.4		1612		
SCC-1-0	51		1797		
	53.6	50.1	1	1883	1720	1.0
	45.9		1481		
SCC-1-6	51.3		1646		
	46.1	51.3	1.02	1722	1756	1.02
	51.1		1899		
SCC-1-6.5	50.5		1485		
	48.6	49.2	0.98	1902	1810	1.05
	48.6		2043		
SCC-1-7	45.5		1849		
	49.8	48.0	0.94	1961	1981	1.15
	48.8		2135		
SCC-1-7.5	48.4		1857		
	47.9	47.0	0.92	1870	1702	0.99
	44.6		1379		
SCC-1-8	45.6		1438		
	42.1		1853		
	49.3	45.7	0.89	1600	1630	0.95
	49.5		1764		
	48.4		1723		

.
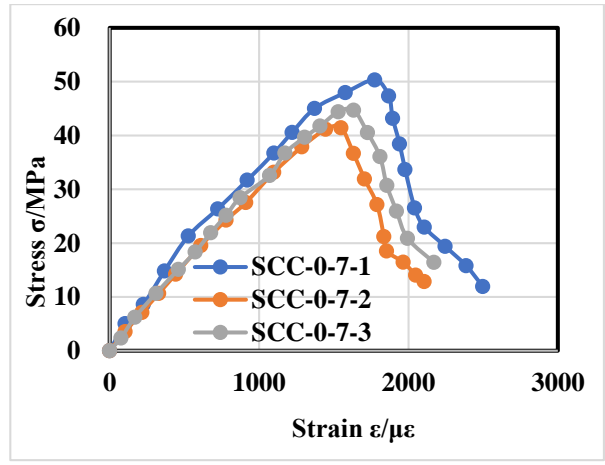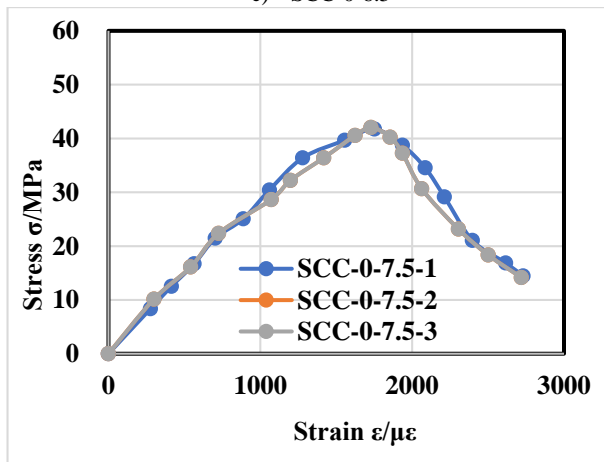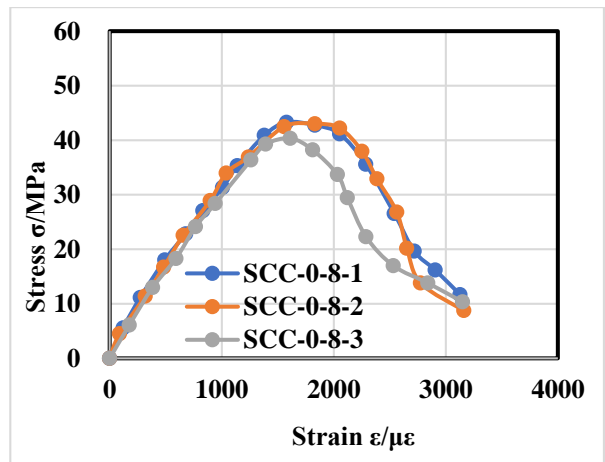
Figure 4. Relationship between stress and strain for specimens made of SCC
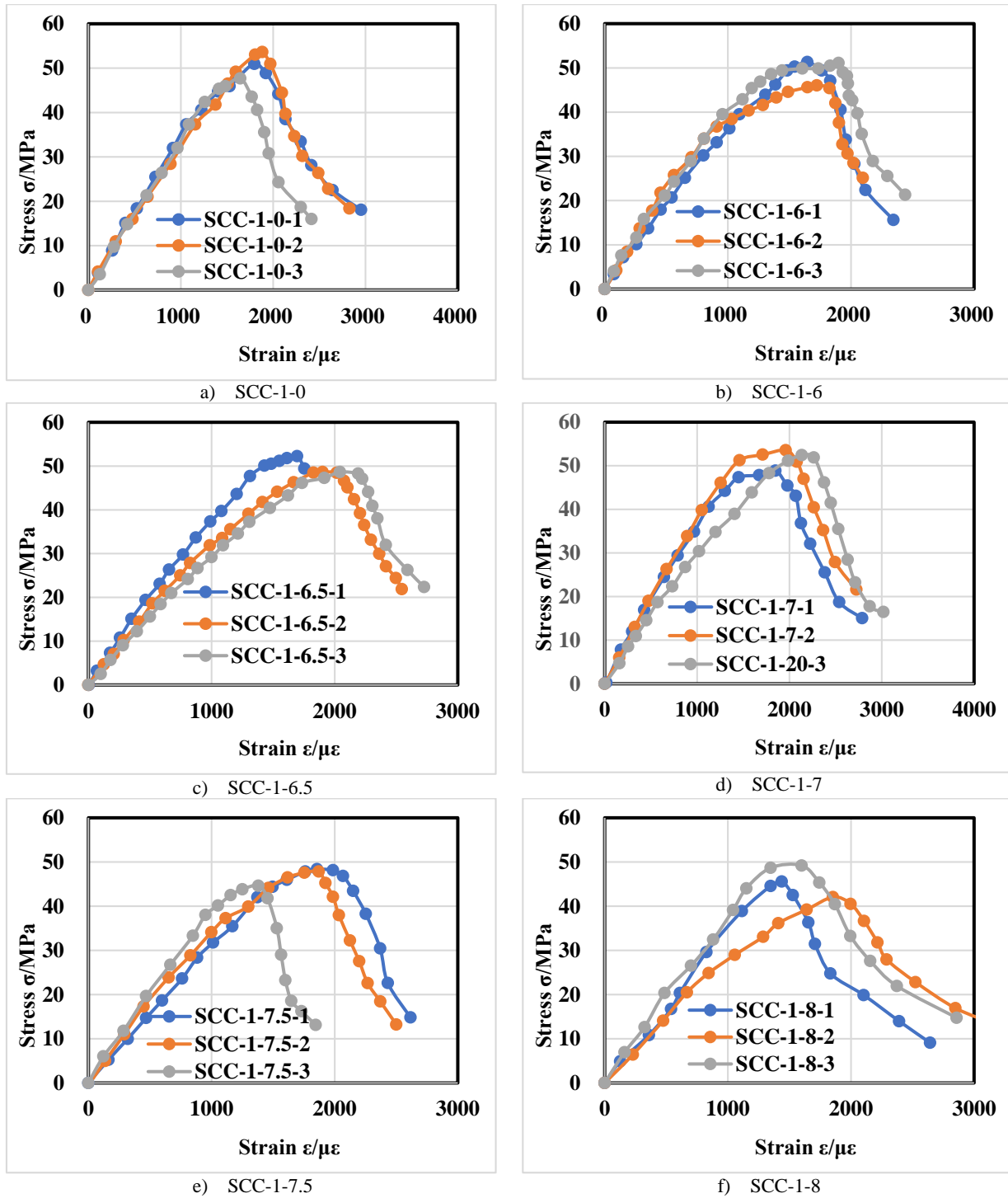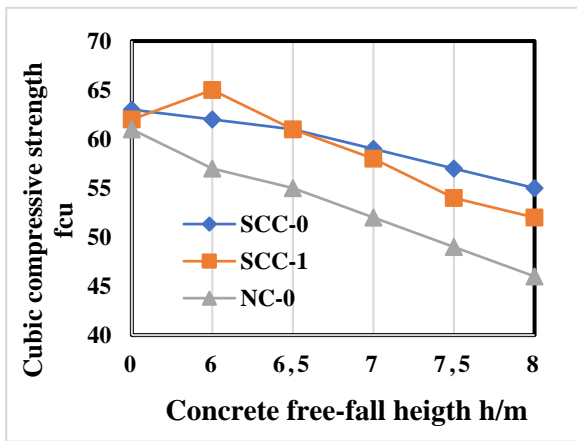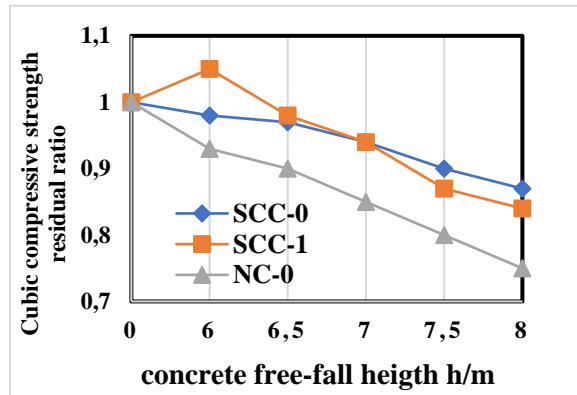
Figure 5. Relationship between stress-strain of specimens of SCC after standing for one hour.

a) $f_{cu} - h$

b) $\lambda_{h-cu} - h$

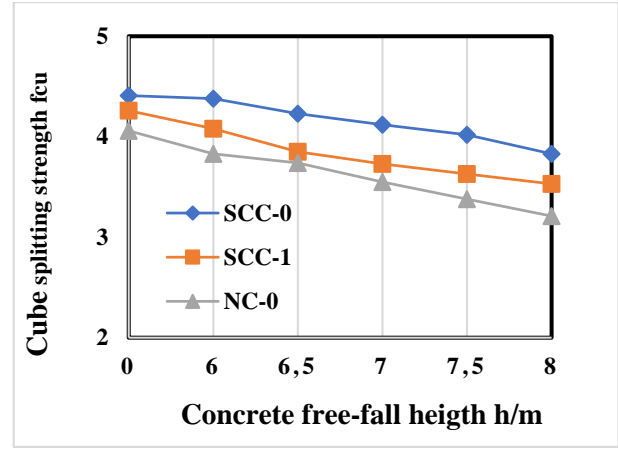Figure 6. Influence of free fall height on compressive strength of cube

a) $f_{cu} - h$

b) $\lambda_{h-sp} - h$

Figure 7. Influence of free fall height on splitting strength of cube
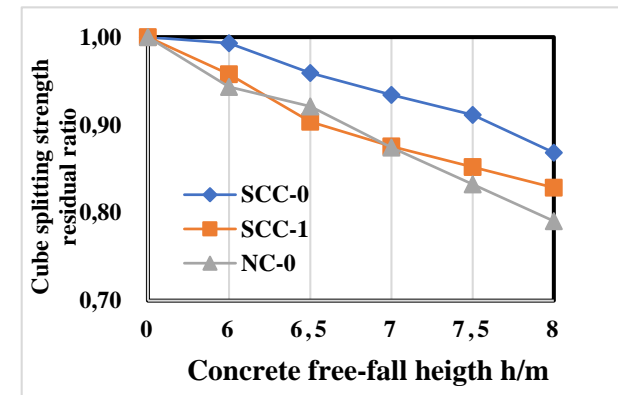
Figure 7 shows that the correlation between the free fall height and the splitting strength of a concrete cube closely mirrors that observed in the compressive strength of a concrete cube. Both exhibit a similar decreasing trend, with the amplitude of decline roughly equivalent. Notably, when the free fall height of SCC specimens in two distinct groups reaches 8 meters, there is an approximate 17% reduction in the splitting strength of the concrete cube. This suggests a consistent and predictable impact of free fall height on the mechanical properties of the concrete, emphasizing the importance of understanding and controlling this factor in structural analysis and design.

3.5. Compressive properties of manufactured sand SCC cube after high throwing

The SCC is prepared with manufactured sand when the free fall height of the concrete is 7m, and its cubic compressive strength is reduced by about 4.3-5.4%, similar to the SCC prepared with natural sand. The reduction is roughly the same. Table 6 shows the compressive strength of SCC cube specimens with manufactured sand.

Table 6. Compressive strength of cubic concrete

Specimen number	Freefall height /m	Cube specimen strength f_{cu}/MPa				
		Data1	Data2	Data3	average value	Range of change
SCC-I-0	0	70	74	75	73	-5.4%
SCC-I-7	7	70	70	68	69	
SCC-II-0	0	64	69	68	67	-4.5%
SCC-II-7	7	63	65	64	64	
SCC-III-0	0	68	70	66	68	-4.4%
SCC-III-7	7	65	64	68	65	
SCC-V-0	0	68	69	67	68	-4.4%
SCC-V-7	7	66	65	64	65	
SCC-IV-0	0	70	68	70	69	-4.3%
SCC-IV-7	7	67	66	64	66	

3.6 Cube-splitting performance of manufactured sand SCC after free fall

From Table 7, it is evident that when SCC is prepared with manufactured sand, its cube-splitting strength at a height of 7m decreases by approximately 7–11%, which is slightly higher than that of SCC prepared with natural sand.

Table 7. Cube-splitting strength of SCC with manufactured sand after high casting.

Specimen number	Freefall heig	Data1	Data2	Data3	average value	Range of change
SCC-1-0	0	5.32	4.82	5.05	5.06	-7%
SCC-1-7	7	4.62	4.75	4.78	4.72	
SCC-2-0	0	4.65	4.53	4.62	4.60	-11%
SCC-2-7	7	4.02	4.08	4.16	4.09	
SCC-3-0	0	4.62	4.56	4.78	4.65	-10%
SCC-3-7	7	4.12	4.25	4.21	4.19	
SCC-4-0	0	4.75	4.62	4.71	4.69	-9%
SCC-4-7	7	4.32	4.25	4.28	4.28	
SCC-5-0	0	4.75	4.83	4.82	4.80	-9%
SCC-5-7	7	4.42	4.35	4.38	4.38	

In conjunction with the compressive strength, during the free-falling process, if the concrete does not undergo segregation, the free-falling height also has a relatively minor impact on the splitting strength of the concrete. Nonetheless, the reduction range is slightly greater than the compressive strength

The techniques employed for detecting and assessing SCC quality in CFST columns have consistently yielded reliable results. These results indicate the absence of voids, ensuring a seamless flow of concrete within the steel tube. This attests to the compactness and cohesion between SCC and CFST columns in terms of quality, strength, and durability – crucial measures for ensuring the structural integrity and resilience of high-rise buildings. The robust evaluation methods employed not only affirm the absence of voids but also underscore the essential attributes necessary for the optimal performance of these structures in the long term.

4. Conclusions

This study evaluates the mechanical properties by testing SCC at various free-fall heights. Subsequently, the concrete is applied to CFST columns, a scenario previously identified as challenging. The findings indicate that an increase in free fall height has detrimental effects on both normal concrete and SCC. The concrete's behaviour aligns closely with the obtained slump range, leading to a reduction in compressive and splitting strength. Specifically, SCC experiences a gradual decrease, with a notable drop of 15%-20% observed at a total height of 8 m. Interestingly, SCC prepared with manufactured sand remains suitable up to height of 7m. Notably, at a 6m free fall height, the study aligns with the results within the expected range, yielding void-free columns without segregation. The key conclusions drawn are as follows:

(1) The cube's compressive and splitting strength decreases with the increase in height of the conduit. However, compared with ordinary concrete, the decrease in strength of SCC is generally smaller. With the rise in the free fall height of concrete, the compressive strength of the prismatic body also decreases, which is similar to the

compressive strength of the cube.

(2) The mechanical properties of SCC exhibit a nonlinear decrease as the free fall height increases. For total heights below 6.5m, there is an approximate 3% decrease in mechanical properties. However, as the total height increases further, the reduction range becomes more significant. Upon reaching a height of 8m, the reduction range for the mechanical properties indicates a substantial impact on the overall performance of the SCC.

(3) When considering a total height of 7m, the decline in cube compressive strength for SCC using manufactured sand is approximately equivalent to that observed in SCC prepared with natural sand. The reduction in cube splitting strength ranges from 7% to 11%, which is slightly higher than the corresponding decrease observed in SCC made with natural sand (7%).

(4) Through the verification test within 6m of free fall height, it is feasible that the maximum drop height of the core concrete of CFST should not be greater than twice the height.

The current research aims to comprehend the performance of SCC under significant height drops and its potential application in CFST columns. Despite previous studies, there is a critical need for further research to comprehensively explore various aspects of SCC, especially when incorporating manufactured (derived/artificial) sand in CFST columns. This includes investigating shrinkage performance, analysing the bonding properties between manufactured sand concrete and steel tubes, assessing flexural and creep behaviour, and evaluating the long-term behaviour associated with these columns.

Conflict of interest declaration:

The authors declare that they have no conflicts of interest concerning this article.

Credit Author Statement

Jean de Dieu Ninteretse: Conceptualization of the study, devising the methodology, developing the necessary software tools for data analysis, interpretation of the results, and writing of the original draft.
Marc Nshimiyimana: Conceptualizing the research, devising the methodology, overseeing the project's progress, and interpreting the results. and writing the original draft, overall supervision.
Jovial Niyogisubizo: visual representations, and interpretation of the results.
Jean Claude Sugira: Writing, technical skills
Alain Niyongabo: Supervision

References

1. Chen, S. J., & Zhang, X. N. (2012). Preparation and application of self-compacting concrete-filled steel tube using polymer admixtures. Advanced Materials Research, 415, 265-271.
2. Huang, Z., Uy, B., Li, D., & Wang, J. (2020). Behaviour and design of

ultra-high-strength CFST members subjected to compression and bending. Journal of Constructional Steel Research, 175, 106351.

3. Cullochje, J. (2023). Advantages and application of self-compacting concrete in bending frame structures. SSRN. Available at https://ssrn.com/abstract=4360186

4. Gunawardena, T., & Mendis, P. (2022). Prefabricated building systems—design and construction. Encyclopedia, 2(1), 70-95.

5. Cao, B., Xie, M., Huang, B., Hu, G., & Wang, J. (2023). Axial compression performance of precast circular semi-continuous concrete-filled steel tube columns: Finite element analysis and theoretical modeling. Buildings, 13(2), 284.

6. Joseph, J. R., & Henderson, J. H. (2023). Concrete–filled steel tube truss girders—a state-of-the-art review. Journal of Engineering and Applied Science, 70(1), 1-15.

7. Hou, X., Cao, S., Rong, Q., Zheng, W., & Li, G. (2018). Effects of steel fiber and strain rate on the dynamic compressive stress-strain relationship in reactive powder concrete. Construction and Building Materials, 170, 570-581.

8. Cao, B., Zhu, L., Jiang, X., & Wang, C. (2022). An investigation of compression bearing capacity of concrete-filled rectangular stainless steel tubular columns under axial load and eccentric axial load. Sustainability, 14(14), 8946.

9. Chen, D., Montano, V., Huo, L., & Song, G. (2020). Depth detection of subsurface voids in concrete-filled steel tubular (CFST) structure using percussion and decision tree. Measurement, 163, 107869.

10. Zheng, W.-T., Xu, B., Wang, J., & Liu, J.-L. (2023). A concrete core void imaging approach for concrete-filled steel tube members and parameter analysis with travel time tomography. [Details of publication missing]

11. Kumari, B. (2018). Concrete filled steel tubular (CFST) columns in composite structures. IOSR Journal of Electrical and Electronics Engineering (IOSR-JEEE), 13(1), 11-18.

12. Badry, F. (2015). Experimental and numerical studies in self-compacting concrete. Cardiff University.

13. Tan, V. M. A., Yambao, M. E. F., Bravo, R. R., & Familara, J. A. (2019). Influence of natural fibers on the fresh and hardened properties of self-compacting concrete (SCC). World Scientific News, 115, 229-241.

14. Xiamuxi, A., Aosimanjiang, A., & Yang, B. (2023). Loading performance of reinforced and recycled aggregate concrete-filled circular steel tube short column with different steel ratios. Construction and Building Materials, 399, 132486.

15. Chen, H., Liu, L., Cai, M., Sun, L., Wang, P., & Liu, M. (2023). Mechanical behaviour of TOBs bolted T-stubs with thick arc-shaped flange to steel tube under tension: A numerical and theoretical investigation. [Details of publication missing]

16. Fleming, K., Weltman, A., Randolph, M., & Elson, K. (2008). Piling engineering. CRC Press.

17. Shen, Z., Chen, D., Zhao, L., & Wei, Y. (2024). Toward the balance between computational cost and model performance for the void detection of concrete-filled steel tubular structure using one-dimensional Mel-frequency cepstral coefficients and ensemble machine learning. Construction and Building Materials, 411, 134366.

18. Szilágyi, K., Borosnyói, A., & Zsigovics, I. (2011). Rebound surface hardness of concrete: Introduction of an empirical constitutive model. Construction and Building Materials, 25(5), 2480-2487.

19. Lu, H., Han, L.-H., & Zhao, X.-L. (2010). Fire performance of self-consolidating concrete filled double skin steel tubular columns: Experiments. Fire Safety Journal, 45(2), 106-115.

20. Le, T.-T., Asteris, P. G., & Lemonis, M. E. (2022). Prediction of axial load capacity of rectangular concrete-filled steel tube columns using machine learning techniques. Engineering with Computers, 38(Suppl 4), 3283-3316.

21. Ros, S., & Shima, H. (2013). Relationship between splitting tensile strength and compressive strength of concrete at early age with different types of cements and curing temperature histories. Concrete Institute Proceedings, 35, 427-432.

22. Kankam, C. K., Meisuh, B. K., Sossou, G., & Buabin, T. K. (2017). Stress-strain characteristics of concrete containing quarry rock dust as partial replacement of sand. Case Studies in Construction Materials, 7, 66-72.